

Computational development of the Planar Miniaturized Fast Neutron
Detector

by

Luke Stegeman

B.S., Kansas State University, 2019

A THESIS

submitted in partial fulfillment of the
requirements for the degree

MASTER OF SCIENCE

Alan Levin Department of Mechanical and Nuclear Engineering
Carl R. Ice College of Engineering

KANSAS STATE UNIVERSITY
Manhattan, Kansas

2022

Approved by:

Major Professor
Amir A. Bahadori

Copyright

© Luke Stegeman 2022.

Abstract

A novel fast neutron spectrometer concept called the Miniaturized Fast Neutron Detector has been computationally developed and characterized via a series of radiation transport simulations. The planar version of the Miniaturized Fast Neutron Detector consists of a plastic converter layer situated in front of an arbitrary number of stacked, electrically isolated thin-silicon diode detectors. Ideally, incoming neutrons impinge upon the plastic, produce recoil ions, and those recoil ions deposit energy in one or more of the diode detectors placed behind the plastic. The spectrometer is capable of reconstructing incident neutron energy spectra without *a priori* information via at least two distinct unfolding algorithms. The ultimate purpose of the device is to act as an advanced personal dosimeter or area monitor with high position resolution to improve the accuracy of local radiation risk estimates due to secondary neutron radiation.

In this work, the device's ability to unfold three distinct incident neutron energy spectra, the spectroscopic effectiveness of the device as a function of incident integral neutron fluence, and a set of strategies for optimizing and mathematically generalizing the device geometry are all presented. Radiation transport simulations were conducted to generate absorbed dose response functions for each diode detector and to compute the absorbed dose in each diode detector due to incident ^{252}Cf , AmB, and AmBe neutron energy spectra as a function of integral neutron fluence. These data are used to test the unfolding capability of the device and characterize its spectroscopic effectiveness. Two unfolding algorithms are considered: the matrix inversion unfolding method, which employs a non-negative least-squares algorithm, and the SPUNIT method. Further radiation transport simulations and analyses were conducted to develop a strategy to optimize the dimensions of the plastic conversion layer and the diode detectors for any arbitrary neutron energy range so that individual device iterations can be tailored to various environments.

The results of this work demonstrate that the planar Miniaturized Fast Neutron Detector is capable of unfolding a diverse range of incident neutron energy spectra without *a priori* information. The effectiveness of the device is quantified as a function of integral neutron fluence and this quantity can be used to determine the minimum integral neutron fluence necessary to generate acceptable unfolded neutron energy spectra (and, by extension, dosimetric quantities and risk-related metrics). The results also demonstrate that the efficiency and energy discrimination capabilities of the current iteration of the device (one with 20 stacked diode detectors) can be improved by decreasing the thickness of the plastic conversion block and increasing the number of uniformly sized diode detectors (or gradually increasing the thickness of diode detectors as a function of device depth).

Table of Contents

List of Figures	viii
List of Tables	xiv
Acknowledgements	xv
Nomenclature	xvi
1 Introduction	1
1.1 Motivation	1
1.2 Radiation Weighting Factors for Neutrons	3
1.3 Measuring the Neutron Energy Spectrum	5
1.3.1 Neutron Spectroscopy Methods	6
1.3.2 Neutron Spectrometers and Portability	7
1.3.3 The Miniaturized Fast Neutron Detector	9
1.4 Operational Overview of the PMFND	11
1.5 Objective	17
2 Methodology	19
2.1 Tools	19
2.1.1 PHITS	19
2.1.2 SRIM	23
2.2 Unfolding the Incident Neutron Energy Spectrum	24
2.2.1 Absorbed Dose Response Function Generation	25
2.2.2 Computing the Absorbed Dose	26

2.2.2.1	Absorbed Dose via Measurement	26
2.2.2.2	Absorbed Dose due to Mono-energetic Neutrons for “Re- response” Simulations	27
2.2.2.3	Absorbed Dose due to Neutron Energy Spectrum for “Dose” Simulations	28
2.2.3	Unfolding Methods	29
2.2.3.1	Non-Negative Least Squares Unfolding Method	30
2.2.3.2	SPUNIT Unfolding Method	32
2.3	Characterizing Spectrometer Effectiveness	33
2.3.1	Radiometric Spectrometer Effectiveness	33
2.3.2	Dosimetric Spectrometer Effectiveness	34
2.3.3	Biometric Spectrometer Effectiveness	35
2.4	Optimizing the PMFND for Future Studies	36
2.4.1	HDPE Block Optimization	36
2.4.1.1	Possible Reactions	37
2.4.1.2	Probability of Neutron-Scattered Ion Reaching Detection Re- gion	38
2.4.2	Optimizing the Unit Cell Detector Stack	44
2.4.2.1	SRIM Runs for Unit Cell Detector Stack Optimization	44
2.4.2.2	Carbon Ion Recoil Considerations	47
3	Results and Discussion	48
3.1	Unfolding the Neutron Energy Spectrum	48
3.1.1	PMFND Response Functions	48
3.1.2	Unfolded Neutron Energy Spectra	49
3.1.2.1	Non-Negative Least Squares Method	50
3.1.2.2	SPUNIT Method	55
3.2	Characterizing Spectrometer Effectiveness	60

3.2.1	Radiometric Spectrometer Effectiveness	60
3.2.2	Dosimetric Spectrometer Effectiveness	64
3.2.3	Biohazard Spectrometer Effectiveness	64
3.2.4	Acceptable Effectiveness Metrics and Minimum Required Neutron Flu- ence	69
3.3	Optimizing the PMFND for Future Studies	71
3.3.1	HDPE Block Optimization Results	71
3.3.2	Optimizing Unit Cell Detector Stack	72
3.3.3	Non-Proton Recoil Ion Elimination	78
4	Conclusions	82
4.1	Future Work	85
	Bibliography	88
A	PHITS Response Simulation Input File	97
B	pysrim Script for PMFND Proton Stopping Power Simulations	115
C	Custom Monte Carlo Code for Determining Entry Probability	120

List of Figures

1.1	Neutron radiation weighting factors as a function of neutron kinetic energy from ICRP 60 and ICRP 103.	4
1.2	Overall PMFND structure; device is 1 cm thick.	9
1.3	Unit cell structure of PMFND.	10
1.4	To-scale size comparison of BBNDs, PRESCILA, and the PMFND (excluding wires, readout equipment, etc.); I is the number of unit cell detectors in the PMFND detector stack.	11
1.5	Depiction of possible elastic interactions that can occur in HDPE block; interactions occur at z_0	14
1.6	Depiction of a proton (or any recoil ion) traversing through HDPE, metallization layers, and the dead region of the Si detection layer, ionizing the media and depositing energy along its path.	15
1.7	Depiction of a proton (or any recoil ion) ionizing the active part of the Si detection region; the holes/electrons freed by ionization travel along/against electric field lines to ultimately be counted by charge collection devices; the unit cell detector is reverse biased with some voltage difference across the diode ΔV	15
1.8	Depiction of the possible paths a recoil proton (or any recoil ion) can take depending on the initial energy thereto imparted via scattering; low initial recoil energies will yield recoil ions that range out in shallow layers, high initial recoil energies will yield recoil ions that range out in deeper layers. . .	16
2.1	Default physics model map in PHITS 3.17.	20

2.2	Graphical representation of physics models used as a function of particle type and energy in PMFND PHITS simulations.	21
2.3	Representative TRIM input.	24
2.4	^{252}Cf , AmB, and AmBe ISO differential neutron energy spectra.	29
2.5	HDPE block with coordinate system and dimensions.	39
2.6	Balloon-like cloud of points representing locations at which recoil protons “range out” in HDPE as well as locations where protons intersect with the back face of the HDPE block.	45
3.1	Absorbed dose response functions for unit cell detectors $i = 1, \dots, 20$	49
3.2	Curve from which all absorbed dose response functions appear to emanate.	50
3.3	Unfolded ^{252}Cf neutron energy spectrum via NNLS method using first five unit cell detectors of PMFND and five linearly spaced energy bins.	51
3.4	Unfolded AmB neutron energy spectrum via NNLS method using first five unit cell detectors of PMFND and five linearly spaced energy bins.	51
3.5	Unfolded AmBe neutron energy spectrum via NNLS method using first five unit cell detectors of PMFND and five linearly spaced energy bins.	52
3.6	Unfolded ^{252}Cf neutron energy spectrum via NNLS method using 20 unit cell detectors of PMFND and 20 linearly spaced energy bins.	53
3.7	Unfolded AmB neutron energy spectrum via NNLS method using 20 unit cell detectors of PMFND and 20 linearly spaced energy bins.	54
3.8	Unfolded AmBe neutron energy spectrum via NNLS method using 20 unit cell detectors of PMFND and 20 linearly spaced energy bins.	54
3.9	Unfolded ^{252}Cf neutron energy spectrum via SPUNIT method using 20 unit cell detectors, the highest integral neutron fluence simulated ($\Phi_0 = 2.1 \times 10^{10} \text{ cm}^{-2}$) and $N_{\text{it}} = 2 \times 10^5$ SPUNIT iterations.	57

3.10	Unfolded AmB neutron energy spectrum via SPUNIT method using 20 unit cell detectors, the highest integral neutron fluence simulated ($\Phi_0 = 2.1 \times 10^{10} \text{ cm}^{-2}$) and $N_{\text{it}} = 2 \times 10^5$ SPUNIT iterations.	57
3.11	Unfolded AmBe neutron energy spectrum via SPUNIT method using 20 unit cell detectors, the highest integral neutron fluence simulated ($\Phi_0 = 2.1 \times 10^{10} \text{ cm}^{-2}$) and $N_{\text{it}} = 2 \times 10^5$ SPUNIT iterations.	58
3.12	Unfolded ^{252}Cf neutron energy spectrum via SPUNIT method using 5 unit cell detectors, the highest integral neutron fluence simulated ($\Phi_0 = 2.1 \times 10^{10} \text{ cm}^{-2}$) and $N_{\text{it}} = 2 \times 10^5$ SPUNIT iterations.	58
3.13	Unfolded AmB neutron energy spectrum via SPUNIT method using 5 unit cell detectors, the highest integral neutron fluence simulated ($\Phi_0 = 2.1 \times 10^{10} \text{ cm}^{-2}$) and $N_{\text{it}} = 2 \times 10^5$ SPUNIT iterations.	59
3.14	Unfolded AmBe neutron energy spectrum via SPUNIT method using 5 unit cell detectors, the highest integral neutron fluence simulated ($\Phi_0 = 2.1 \times 10^{10} \text{ cm}^{-2}$) and $N_{\text{it}} = 2 \times 10^5$ SPUNIT iterations.	59
3.15	Radiometric spectrometer effectiveness as a function of integral neutron fluence for each neutron energy spectrum; marked locations (a), (b), and (c) on the effectiveness curve for each spectrum correspond to the unfolded neutron energy spectra labeled (a), (b), and (c) in Figures 3.16-3.18.	60
3.16	Illustration of unfolded ^{252}Cf spectra converging toward the incident neutron energy spectrum as the integral neutron fluence increases; unfolded spectrum (a) is obtained at a fluence of $3.6 \times 10^4 \text{ cm}^{-2}$ with radiometric spectrometer effectiveness $\varepsilon_1 = 1.37 \times 10^{-4}$ (b) at $3.8 \times 10^8 \text{ cm}^{-2}$ with radiometric spectrometer effectiveness $\varepsilon_1 = 0.173$, and (c) at $2.1 \times 10^{10} \text{ cm}^{-2}$ with radiometric spectrometer effectiveness $\varepsilon_1 = 0.957$	61

3.17	Illustration of unfolded AmB spectra converging toward the incident neutron energy spectrum as the integral neutron fluence increases; unfolded spectrum (a) is obtained at a fluence of $3.6 \times 10^4 \text{ cm}^{-2}$ with radiometric spectrometer effectiveness $\varepsilon_1 = 4.17 \times 10^{-4}$ (b) at $3.8 \times 10^8 \text{ cm}^{-2}$ with radiometric spectrometer effectiveness $\varepsilon_1 = 2.59 \times 10^{-5}$, and (c) at $2.1 \times 10^{10} \text{ cm}^{-2}$ with radiometric spectrometer effectiveness $\varepsilon_1 = 0.941$	62
3.18	Illustration of unfolded AmBe spectra converging toward the incident neutron energy spectrum as the integral neutron fluence increases; unfolded spectrum (a) is obtained at a fluence of $3.6 \times 10^4 \text{ cm}^{-2}$ with radiometric spectrometer effectiveness $\varepsilon_1 = 5.24 \times 10^{-3}$ (b) at $3.8 \times 10^8 \text{ cm}^{-2}$ with radiometric spectrometer effectiveness $\varepsilon_1 = 0.478$, and (c) at $2.1 \times 10^{10} \text{ cm}^{-2}$ with radiometric spectrometer effectiveness $\varepsilon_1 = 0.795$	63
3.19	Dosimetric spectrometer effectiveness as a function of integral neutron fluence for all tested incident neutron energy spectra; marked locations (a), (b), and (c) on the effectiveness curve for each spectrum correspond to the refolded dose values labeled (a), (b), and (c) in Figures 3.20-3.22.	65
3.20	Illustration of refolded absorbed dose values (per source neutron) due to incident ^{252}Cf spectrum converging toward the expected absorbed dose values as the integral neutron fluence increases; refolded dose values (a) are obtained at a fluence of $3.6 \times 10^4 \text{ cm}^{-2}$ with dosimetric spectrometer effectiveness $\varepsilon_2 = -2.54$ (b) at $3.8 \times 10^8 \text{ cm}^{-2}$ with dosimetric spectrometer effectiveness $\varepsilon_2 = 0.989$, and (c) at $2.1 \times 10^{10} \text{ cm}^{-2}$ with dosimetric spectrometer effectiveness $\varepsilon_2 = 0.991$	66

3.21	Illustration of refolded absorbed dose values (per source neutron) due to incident AmB spectrum converging toward the expected absorbed dose values as the integral neutron fluence increases; refolded dose values (a) are obtained at a fluence of $3.6 \times 10^4 \text{ cm}^{-2}$ with dosimetric spectrometer effectiveness $\varepsilon_2 = 0.516$ (b) at $3.8 \times 10^8 \text{ cm}^{-2}$ with dosimetric spectrometer effectiveness $\varepsilon_2 = -0.317$, and (c) at $2.1 \times 10^{10} \text{ cm}^{-2}$ with dosimetric spectrometer effectiveness $\varepsilon_2 = 0.989$	67
3.22	Illustration of refolded absorbed dose values (per source neutron) due to incident AmBe spectrum converging toward the expected absorbed dose values as the integral neutron fluence increases; refolded dose values (a) are obtained at a fluence of $3.6 \times 10^4 \text{ cm}^{-2}$ with dosimetric spectrometer effectiveness $\varepsilon_2 = 0.895$ (b) at $3.8 \times 10^8 \text{ cm}^{-2}$ with dosimetric spectrometer effectiveness $\varepsilon_2 = 0.997$, and (c) at $2.1 \times 10^{10} \text{ cm}^{-2}$ with dosimetric spectrometer effectiveness $\varepsilon_2 = 0.974$	68
3.23	Biohazard spectrometer effectiveness as a function of integral neutron fluence for all tested incident neutron energy spectra.	69
3.24	Two-dimensional map of the mean probability that a local elastic neutron scattering interaction results in a recoil ion exiting the back wall of the HDPE block and has a nonzero chance of contributing to the signal charge in one or more unit cell detectors; in this case, $E_n = 20 \text{ MeV}$	71
3.25	Probability that a local interaction at $z = z_0$ results in the production of a recoil ion that exits the HDPE back face for $E_n \in (0, 20) \text{ MeV}$	72
3.26	Black points represent the depth at which the probability of a local neutron interaction resulting in a recoil ion exiting the back face of the HDPE block becomes non-zero as a function of incident neutron kinetic energy overlaid on proton ranges in HDPE.	73

3.27	Proton stopping power as a function of PMFND depth (excluding HDPE) overlaid on PMFND schematic; green background indicates silicon detection region, magenta line indicates metallization/insulation layers, darkened background indicates unit cell layers beyond unit cell $i = 20$	74
3.28	Proton stopping power as a function of PMFND depth (excluding HDPE) overlaid on PMFND schematic; green background indicates silicon detection region, magenta line indicates metallization/insulation layer, darkened background indicates unit cell layers beyond unit cell $i = 20$; spikes in stopping power at each metallization/insulation layer are suppressed to improve readability.	75
3.29	FWHM of each smoothed Bragg peak of Figure 3.28 and best fit line as a function of initial recoil proton kinetic energy.	77
3.30	Recoil proton range in PMFND unit cell detector stack as a function of initial recoil proton kinetic energy compared with proton range in silicon.	78
3.31	Probability of producing a ${}^1_1\text{H}$ recoil ion via interaction in HDPE as a function of incident neutron kinetic energy E_n ; cross section data from ENDF-VIII.0 via JANIS.	79
3.32	Probability of producing a ${}^2_1\text{H}$ recoil ion via interaction in HDPE as a function of incident neutron kinetic energy E_n ; cross section data from ENDF-VIII.0 via JANIS.	79
3.33	Probability of producing a ${}^{12}_6\text{C}$ recoil ion via interaction in HDPE as a function of incident neutron kinetic energy E_n ; cross section data from ENDF-VIII.0 via JANIS.	80
3.34	Series of ${}^{12}_6\text{C}$ recoil ion stopping power profiles with initial kinetic energies $T \in [0.284, 5.680]$ MeV overlaid on first unit cell detector of PMFND.	81
4.1	Spherical MFND concept.	86

List of Tables

1.1	Materials and atomic compositions of PMFND.	12
2.1	Decay modes, branching ratios, and average particle lifetimes for neutral sub-atomic particles (excluding neutrons due to the use of the event generator) according to PHITS 3.17 User Manual.	22
2.2	Isotopes present in HDPE alongside natural abundance fractions.	38
3.1	Acceptability thresholds for each spectrometer effectiveness type and integral neutron fluence values at which each spectrum achieves the stated threshold for $N = 2 \times 10^5$ SPUNIT iterations.	70
3.2	Fitting parameters for Equation 3.6 assuming silicon density $\rho = 2.33 \text{ g cm}^{-3}$	78

Acknowledgments

I would like to begin by thanking my family—including my dad, Ed, my mom, Laurie, my older brother, Ben, and my younger sister, Jordan—for their encouragement (and their unending curiosity about what exactly it is that I do at work). I thank my roommates—Kalea, Abbi, and Jordan—for their support, friendliness, and brilliant cooking skills. I also want to apologize to all of my other friends for my constant unavailability, and thank them for their understanding.

I thank those who worked on the fabrication side of the original Miniaturized Fast Neutron Detector team, including Prof. Zayd Leseman, Samuel Oxandale, Tyler Hieber, Dr. Dipta Sarkar, Dr. Steve Bellinger, and Tim Sobering. I thank Prof. William Dunn and Prof. Jeremy Roberts for serving on my committee and for the knowledge they have passed down over the course of several years. Finally, I thank Prof. Amir Bahadori for inviting me to work in his research group and for his helpful guidance in this work and beyond.

This work was funded in part by the Johnson Cancer Research Center at Kansas State University. Some of the computing for this project was performed on the Beocat Research Cluster at Kansas State University, which is funded in part by the National Science Foundation (NSF), USA under Grant Nos. CNS-1006860, EPS-1006860, EPS-0919443, ACI-1440548, CHE-1726332, and NIH P20GM113109.

Nomenclature

Abbreviations

$(C_2H_4)_n$ polyethylene

^{252}Cf californium-252

SiO_2 silicon dioxide

pysrim Python module used to conduct many SRIM simulations

Al aluminum

AmB americium-boron (spectrum)

AmBe americium-beryllium (spectrum)

ATIMA subprogram that computes stopping power and range for protons and heavy ions

Au gold

BBND **B**onner **B**all **N**eutron **D**etector

CGNSD **C**apture-**G**ated **N**eutron **S**cintillator **D**etector

EGS **E**lectron-**G**amma **S**hower code

ENDF **E**valuated **N**uclear **D**ata **F**iles

FWHM full-width at half-maximum

GEM **G**eneralized **E**vaporation **M**odel

HDPE high-density polyethylene

ICRP **I**nternational **C**ommission on **R**adiological **P**rotection

INCL **I**ntra-**N**uclear **C**ascade of **L**iége

JANIS **J**ava-based **N**uclear **I**nformation **S**oftware

JENDL **J**apanese **E**valuated **N**uclear **D**ata **L**ibrary

JQMD **J**apan Atomic Energy Research Institute **Q**uantum **M**olecular **D**ynamics

MFND **M**iniaturized **F**ast **N**eutron **D**etector

MSND **M**icrostructured **S**emiconductor **N**eutron **D**etector

NCRP **N**ational **C**ouncil on **R**adiation **P**rotection and **M**easurements

Ni nickel

NIST **N**ational **I**nstitute of **S**tandards and **T**echnology

NNLS **N**on-**N**egative **L**east **S**quares

PDF **p**robability **d**ensity **f**unction

PHITS **P**article and **H**eavy **I**on **T**ransport code **S**ystem

PMFND **P**lanar **M**iniaturized **F**ast **N**eutron **D**etector

PRESCILA **P**roton **R**ecoil **S**cintillator-**L**os **A**lamos

PSTAR **S**topping **P**ower and **R**ange **T**ables for **P**rotons

REIC risk of **e**xposure-**i**nduced **c**ancer

REID risk of **e**xposure-**i**nduced **d**eath

Si silicon

SMFND **S**pherical **M**iniaturized **F**ast **N**eutron **D**etector

SPUNIT **i**terative **s**pectral **u**nfolding algorithm

SRIM **S**topping **P**ower and **R**ange of **I**ons in **M**atter

Ti titanium

TRIM **T**ransport of **I**ons in **M**atter

UNSCEAR **U**nited **N**ations **S**cientific **C**ommittee on the **E**ffects of **A**tomistic **R**adiation

Variables

$(\tilde{a}, \tilde{b}, \tilde{c})$ unitless fitting parameters for Equation 3.6

(x', y', z') final ion recoil position

$(x(t_0), y(t_0), \Delta z)$ location at which recoil ion intersects with plane coincident with back face of HDPE block at $z = \Delta z$

(x_0, y_0, z_0) neutron interaction location in HDPE block

α defined by Equation 2.48

$\bar{\chi}$ average value of incident neutron energy spectrum integrated from E_0 to E_J

\bar{D} average absorbed dose over all unit cell detectors

\bar{F} average value of unfolded neutron energy spectrum integrated from E_0 to E_J

$\chi(E_n)$ incident neutron energy spectrum

ΔE_j difference between current and previous neutron energies, $\Delta E_j = E_j - E_{j-1}$

ΔE_m modified neutron energy bin width after averaging, $\Delta E_m = E_{\text{high},m} - E_{\text{low},m}$

ΔV reverse-bias voltage difference across unit cell detector

Δx transverse dimension of PMFND

Δy transverse dimension of PMFND (perpendicular to Δx)

- Δz thickness of HDPE block
- $\Delta z_{\text{dead},i}$ thickness of dead Si region i
- $\Delta z_{\text{ins},i}$ thickness of insulation layer in unit cell detector i
- $\Delta z_{\text{met},i}$ thickness of metallization layers in unit cell detector i
- Δz_i thickness of active Si region i
- Δ defined by Equation 2.49
- δ small distance in z
- $\delta(\cdot)$ delta function
- $\Delta_m D_i$ m -th partial absorbed dose associated with the i -th unit cell detector
- ℓ stopping power data index
- $\frac{dQ_i}{dt}$ total current collected by unit cell detector i
- γ defined by Equation 2.51
- \hat{z} HDPE depth at which the probability that a local neutron interaction results in a recoil ion exiting the back face of the HDPE block first becomes non-zero
- $\Lambda_{\text{HDPE}}(T)$ range of recoil ion of initial kinetic energy T in HDPE
- $\lambda_{\text{inc},\mathcal{T}}$ tissue-specific hazard function for radiation exposure based on cancer incidence
- $\lambda_{\text{mort},\mathcal{T}}$ tissue-specific hazard function for radiation exposure based on cancer mortality
- $\Lambda_{p,\text{HDPE}}(T)$ range of recoil proton of initial kinetic energy T in HDPE
- $\Lambda_{p,\text{PMFND}}$ proton range in PMFND detector stack
- $\langle w_R \rangle$ energy-averaged neutron radiation weighting factor
- \mathcal{R} $I \times J$ response function matrix

\mathcal{R}_{AV} modified, energy-averaged, $I \times M$ response matrix
 $\mathcal{A}_{\text{HDPE}}$ atomic weight of HDPE
 \mathcal{D} rectangular 2d spatial domain of PMFND cross section
 \mathcal{E}_i total energy deposited in unit cell detector i
 $\mathcal{E}_{\text{high},k}$ high energy bin edge
 $\mathcal{E}_{\text{low},k}$ low energy bin edge
 \mathcal{E}_{th} PMFND equivalent energy deposition threshold
 \mathcal{M} mission index
 $\mathcal{R}(\vec{Q}, \vec{P})$ generic response function of generic state-variable vector \vec{Q} and generic distributed-variable vector \vec{P}
 $\mathcal{R}_i(E_j)$ or $\mathcal{R}_i(E_j, \vec{\Omega}_0)$ absorbed dose response function associated with i -th unit cell detector evaluated at E_j
 $\mathcal{R}_i(E_n, \vec{\Omega})$ absorbed dose response function associated with i -th unit cell detector, dependent on both incident neutron kinetic energy and solid angle
 $\mathcal{R}_{\mathcal{T}}(E_n)$ absorbed dose response function of \mathcal{T}
 $\mathcal{R}_H(E_n)$ ambient dose equivalent response function evaluated at E_n
 \mathcal{T} tissue/medium identifying parameter
 $\mu(E_n)$ probability of neutron interaction in HDPE per unit path length as a function of E_n
 $\mu_q(E_n)$ probability per unit path length of an interaction of type q occurring in HDPE
 ν isotope identifying parameter
 ω_c direction cosine of the scattered neutron in the center-of-mass system

ω_r cosine of recoil ion scattering angle

$\Phi(\vec{P})$ generic fluence distribution function, distributed over variables contained in \vec{P}

$\Phi(\vec{r}, E_n)$ or $\Phi(E_n)$ energy-dependent neutron fluence distribution fluence

$\Phi(\vec{r}, E_n, \vec{\Omega})$ or $\frac{\partial^2 \Phi(\vec{r})}{\partial E_n \partial \Omega}$ or $\Phi(E_n, \vec{\Omega})$ energy- and angle-dependent neutron fluence distribution function

Φ_0 integral neutron fluence

Φ_j^n n -th iteration of j -th neutron fluence vector element

$\Phi_{AV}(E_m)$ m -th element of modified neutron fluence vector

ψ_r recoil ion azimuthal angle (about $+z$ -axis)

ρ_{HDPE} HDPE density

$\sigma_{q,C-12}$ neutron cross section for neutron interactions of type q that result in the production of a $^{12}_6\text{C}$ recoil ion

$\sigma_{q,H-1}$ neutron cross section for neutron interactions of type q that result in the production of a ^1_1H recoil ion

$\sigma_{q,H-2}$ neutron cross section for neutron interactions of type q that result in the production of a ^2_1H recoil ion

θ_s neutron scattering angle

\tilde{D}_i^n n -th iteration of i -th absorbed dose vector element

ε_1 radiometric spectrometer effectiveness

ε_2 dosimetric spectrometer effectiveness

ε_3 biohazard spectrometer effectiveness

$\vec{1}$ size J vector of 1's

$\vec{\Omega}$	solid angle direction
$\vec{\Omega}_0$	incident solid angle direction used for generating absorbed dose response functions via PHITS ($\vec{\Omega}_0 = \langle 1, 0, 0 \rangle$ in this work)
$\vec{\Phi}$	energy-dependent neutron fluence vector
$\vec{\Phi}^0$	initial neutron fluence vector guess used in SPUNIT method
$\vec{\Phi}_{AV}$	energy-averaged $M \times 1$ neutron fluence vector
\vec{D}	absorbed dose vector
\vec{D}^0	initial absorbed dose vector used in SPUNIT method
\vec{r}	position vector
$V_{\mathcal{T}}$	volume of \mathcal{T}
A	mass number
a	attained age
$a_{\mathcal{M}}$	age of exposure for mission \mathcal{M}
A_{PMFND}	cross-sectional area ($\Delta x \times \Delta y$) of the PMFND
$D_i(E_j)$	absorbed dose obtained in unit cell detector i due to incident neutrons of kinetic energy E_j
D_i^r	refolded absorbed dose in unit cell detector i
$D_{\mathcal{T},R}$	absorbed dose in \mathcal{T} due to radiation of type R (neutrons)
e	elementary charge (or Euler's constant)
E_i	target energy for a particular unit cell detector under the PMFND optimization model in which deeper unit cell detectors are thickened to capture a particular energy group

- E_j j -th neutron kinetic energy used for generating absorbed dose response functions via PHITS
- E_n neutron kinetic energy
- E'_n scattered neutron kinetic energy
- $E_{\text{high},m}$ high energy bin edge for modified energy bin structure
- $E_{\text{low},m}$ low energy bin edge for modified energy bin structure
- $E_{n,\text{max}}$ maximum neutron energy of interest
- $E_{n,\text{min}}$ minimum neutron energy of interest
- $F(E_m)$ m -th element of unfolded neutron energy spectrum vector
- $f(x)$ generic unknown spectrum that is a function of generic variable x
- f^{C-12} natural abundance of $^{12}_6\text{C}$
- f^{H-1} natural abundance of ^1_1H
- f^{H-2} natural abundance of ^2_1H
- $g(y)$ generic known quantity that is a function of generic variable y
- $H^*(10\text{ mm})$ ambient dose equivalent
- $H_r^*(10\text{ mm})$ refolded ambient dose equivalent
- $H_{\mathcal{T},\mathcal{M}}$ tissue-dose equivalent for mission \mathcal{M}
- $H_{\mathcal{T}}$ equivalent dose incurred in \mathcal{T}
- I number of unit cell detectors in the PMFND
- i index associated with i -th unit cell detector in PMFND detector stack
- J number associated with maximum neutron energy index

j	neutron energy index
k	deposition energy bin index
$K(x, y)$	generic Green's function of generic variables x and y
M	number associated with maximum neutron energy index after averaging data to improve matrix inversion unfolding method
m	neutron energy index after averaging data to improve matrix inversion unfolding method
m_i	mass of active silicon detection region in unit cell detector i
n	SPUNIT iteration index
N_a	Avogadro's number
$N_i(\mathcal{E})$	number deposition in unit cell detector i as a function of deposition energy \mathcal{E}
N_p	number of histories used for PHITS simulations
N_{it}	total number of SPUNIT iterations
$N_{i,k}$	number deposition value in unit cell detector i and energy deposition bin k
Q	Q -value associated with nuclear reaction
Q_i	signal charge deposited in unit cell detector i
Q_{th}	PMFND charge threshold
r	statistical correlation coefficient
R^2	coefficient of determination
r^2	square Pearson correlation coefficient
$S_{\text{adj}}(a \vee a_{\mathcal{M}})$	overall survival function adjusted for deaths caused by radiation exposure

- T kinetic energy of recoil ion (most often, protons)
- t time
- t_0 instant at which recoil ion intersects with $z = \Delta z$ plane
- $w_R(E_n)$ neutron radiation weighting factor as a function of neutron kinetic energy
- w_{Si} average energy required to produce an electron-hole pair in silicon
- z distance along the primary axis of the PMFND; $+z$ -axis points from front face of HDPE ($z = 0$) to back face of PMFND ($z = \Delta z + \sum_{i=1}^I \left[\Delta z_i + 2\Delta z_{\text{dead},i} + 2\Delta z_{\text{met},i} + \Delta z_{\text{ins},i} \right]$)
- $R(\vec{Q})$ generic response as a function of generic state-variable vector \vec{Q}

Chapter 1

Introduction

1.1 Motivation

Human exposure to neutron radiation has the potential to cause cancer. There are several scenarios where the neutron environment is intense enough to warrant concern for the health of those exposed. Nuclear reactors¹, particle accelerators², radiation therapy centers³, and human spaceflight^{4;5} are all neutron-rich environments. Nuclear reactors and particle accelerators are the most obvious examples of places where neutron exposure is a concern. Regulatory agencies across the globe, including the United Nations Scientific Committee on the Effects of Atomic Radiation (UNSCEAR), the International Commission on Radiological Protection (ICRP), and the National Council on Radiation Protection and Measurements (NCRP), issue recommendations to governments on how nuclear technicians and operations personnel should be monitored for exposure to neutron radiation. Recommendations are often determined in a scientifically conservative manner and could be influenced, either to enhance safety measures or to optimize economic efficiency, by improving the accuracy with which cancer risk due to neutron exposure (and other radiation exposure) is estimated. Nuclear reactors and particle accelerator facilities are commonly supplied with standard issue dosimeters worn by personnel that measure some form of “dose” incurred in the worker over a period of a few weeks to months. The neutron energy spectrum is generally well-known

in radiation-intense regions of these facilities due to exhaustive modeling and adjacency to tools that allow designers to conduct rigorous safety evaluations.

During normal operation, nuclear reactors and particle accelerators are generally operated remotely from a relatively safe location—humans are never intentionally exposed to neutron radiation. In contrast, radiation therapy centers which are designed to treat *people*, requiring the presence of humans alongside neutron radiation. Likewise, spacecraft can house a crew of *people* as they orbit the Earth or traverse the cosmos. This fundamental difference in purpose increases the importance of monitoring the risk of cancer and death due to neutron exposure. Another difference between neutron environments that are explicitly designed to safely carry out nuclear processes and those in which nuclear processes are necessary to achieve a desired result, is that in the latter case, the neutrons that are produced are generally *secondary neutrons*. Secondary neutron spectra are less predictable than primary neutron spectra because they are highly dependent on the surrounding shielding distribution. Primary particle spectra interact with the environment in a way that could only be predicted via time-consuming, computationally expensive Monte Carlo simulations that include environment-specific geometry. Secondary neutron spectra are thus generally unknown or are highly uncertain prior to some form of measurement.^{6;7}

The risk of developing cancer due to incident neutron irradiation is most generally dependent on the fluence distribution function $\Phi(\vec{r}, E_n, \vec{\Omega})$. $\Phi(\vec{r}, E_n, \vec{\Omega})$, or $\frac{\partial^2 \Phi(\vec{r})}{\partial E_n \partial \Omega}$, depends on neutron kinetic energy E_n , solid angle direction $\vec{\Omega}$, and position \vec{r} . In simpler terms, the risk of developing cancer due to neutron exposure depends on

1. The incident neutron energy spectrum $\chi(E_n)$,
2. The distribution of directions from which neutrons arrive at the position \vec{r} ,
3. The intensity of the incident neutron fluence, and
4. The location of interest \vec{r} , which encompasses the shielding (including body self-shielding) overcome to reach \vec{r} , as well as the organ in which \vec{r} is located.

1.2 Radiation Weighting Factors for Neutrons

In terms of predicting risk, the two most important aspects of the neutron radiation environment are the neutron fluence intensity and the neutron energy spectrum. The equivalent dose in some tissue-medium \mathcal{T} due to neutron irradiation is given by

$$H_{\mathcal{T}} = \langle w_R \rangle D_{\mathcal{T},R}, \quad (1.1)$$

where $\langle w_R \rangle$ is the neutron-energy-averaged radiation weighting factor for neutrons and $D_{\mathcal{T},R}$ is the absorbed dose in tissue-medium \mathcal{T} due to neutron irradiation. The neutron radiation weighting factor has historically been a *function of neutron kinetic energy* and its definition has been refined over time. ICRP Report 60 from 1990 defined radiation weighting factors for neutrons using a step function⁸,

$$w_R(E_n) = \begin{cases} 5, & \text{for } E_n < 10 \text{ keV} \\ 10, & \text{for } 10 \text{ keV} \leq E_n \leq 100 \text{ keV} \\ 20, & \text{for } 100 \text{ keV} \leq E_n \leq 2 \text{ MeV} \\ 10, & \text{for } 2 \text{ MeV} \leq E_n \leq 20 \text{ MeV} \\ 5, & \text{for } E_n > 20 \text{ MeV} \end{cases} . \quad (1.2)$$

In 2007, ICRP Report 103 updated the neutron radiation weighting factor definition to a continuous function⁹,

$$w_R(E_n) = \begin{cases} 2.5 + 18.2e^{-[\ln(E_n)]^2/6}, & \text{for } E_n < 1 \text{ MeV} \\ 5.0 + 17.0e^{-[\ln(2E_n)]^2/6}, & \text{for } 1 \text{ MeV} \leq E_n \leq 50 \text{ MeV} \\ 2.5 + 3.25e^{-[\ln(0.04E_n)]^2/6}, & \text{for } E_n > 50 \text{ MeV} \end{cases} . \quad (1.3)$$

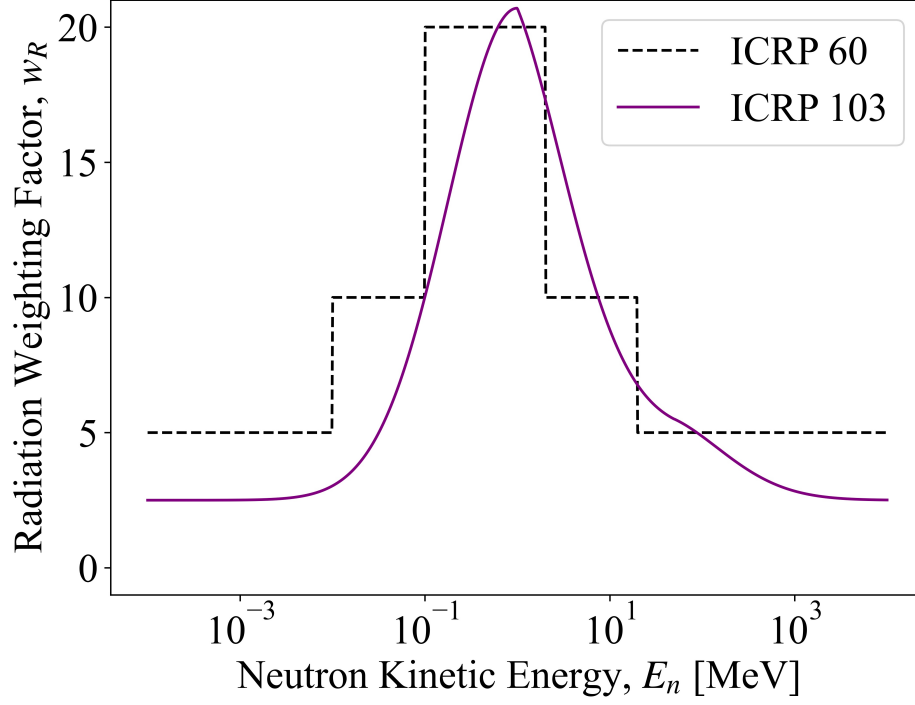


Figure 1.1: Neutron radiation weighting factors as a function of neutron kinetic energy from ICRP 60 and ICRP 103.

The ICRP 60 and 103 definitions are shown in Figure 1.1. Due to the functional dependence of w_R on E_n , the neutron-energy-averaged radiation weighting factor is given by

$$\langle w_R \rangle = \int_0^{\infty} w_R(E_n) \chi(E_n) dE_n, \quad (1.4)$$

where $\chi(E_n)$ is the probability density function that describes the distribution of incident neutron kinetic energies. The dose in tissue-medium \mathcal{T} due to neutrons $D_{\mathcal{T},R}$ can be computed in several ways. One method is to use a response function method,

$$D_{\mathcal{T},R} = \frac{1}{V_{\mathcal{T}}} \int_{V_{\mathcal{T}}} \int_0^{\infty} \mathcal{R}_{\mathcal{T}}(E_n) \Phi(\vec{r}, E_n) dE_n d\vec{r}, \quad (1.5)$$

where $\mathcal{R}_{\mathcal{T}}(E_n)$ is the absorbed dose response function of homogeneous tissue-medium \mathcal{T} at energy E_n , $\Phi(\vec{r}, E_n)$ is the solid-angle integrated fluence distribution function,

$$\Phi(\vec{r}, E_n) = \int_{4\pi} \Phi(\vec{r}, E_n, \vec{\Omega}) d\Omega, \quad (1.6)$$

and $V_{\mathcal{T}}$ is the volume of the tissue-medium. The tissue-specific absorbed dose is important for computing several radiation risk quantities, including risk of exposure-induced cancer (REIC) and risk of exposure-induced death (REID). NASA estimates REIC and REID via

$$\text{REIC} = \sum_{\mathcal{M}} \sum_{\mathcal{T}} \sum_{a=a_{\mathcal{M}}}^{101} \lambda_{\text{inc},\mathcal{T}}(a_{\mathcal{M}}, a, H_{\mathcal{T},\mathcal{M}}) S_{\text{adj}}(a \vee a_{\mathcal{M}}), \quad (1.7)$$

and

$$\text{REID} = \sum_{\mathcal{M}} \sum_{\mathcal{T}} \sum_{a=a_{\mathcal{M}}}^{101} \lambda_{\text{mort},\mathcal{T}}(a_{\mathcal{M}}, a, H_{\mathcal{T},\mathcal{M}}) S_{\text{adj}}(a \vee a_{\mathcal{M}}), \quad (1.8)$$

where \mathcal{M} is a space-mission index, $a_{\mathcal{M}}$ is the age of exposure for mission \mathcal{M} , a is the attained age, $H_{\mathcal{T},\mathcal{M}}$ is the tissue-dose equivalent for mission \mathcal{M} , $\lambda_{\text{inc},\mathcal{T}}(a_{\mathcal{M}}, a, H_{\mathcal{T},\mathcal{M}})$ and $\lambda_{\text{mort},\mathcal{T}}(a_{\mathcal{M}}, a, H_{\mathcal{T},\mathcal{M}})$ are the tissue-specific hazard functions for radiation exposure based on cancer incidence and mortality respectively, and $S_{\text{adj}}(a \vee a_{\mathcal{M}})$ is the overall survival function adjusted for deaths caused by radiation exposure.¹⁰ Both $\langle w_R \rangle$ and $\Phi(\vec{r}, E_n)$ are dependent on $\chi(E_n)$, implying that detailed knowledge of the incident neutron energy spectrum is necessary to accurately estimate resultant cancer risk due to neutron irradiation.

1.3 Measuring the Neutron Energy Spectrum

Neutron spectrometers are used to measure the incident neutron energy spectrum. However, a universally “ideal” neutron spectrometer does not exist. Neutron spectrometers are optimized according to the context in which they are utilized. The context relevant to this discussion is one in which fast neutrons—neutrons within the range $E_n \in [1, 20]$ MeV—dominate the radiation environment and the unknown incident neutron energy spectrum

$\chi(E_n)$ is sought so that personal dosimetry and cancer risk can be assessed for an individual or to conduct area monitoring in a small volume.

An ideal neutron spectrometer for this scenario is one that

1. Is light, so the device can be worn on a person's clothing,
2. Does not require much power to operate, so the device can be worn over an extended period of time and maintain practical portability,
3. Is compact, so the device can measure the neutron energy spectrum with fine position resolution, and
4. Responds identically to neutron irradiation from all directions (isotropy).

1.3.1 Neutron Spectroscopy Methods

Neutrons are considered *indirectly ionizing radiation* because neutrons ionize matter via interactions where energetic secondary charged particles result, and those charged particles ionize the local medium by direct interaction with atomic electrons. This fact makes neutron detection, and by extension neutron spectroscopy, more complicated than the detection of heavy charged particles, electrons, photons, etc. There are several well-established neutron spectroscopy methods. Brooks and Klein categorized seven generic categories of neutron spectroscopy as follows¹¹:

1. Measuring the energy of a recoil nucleus after being scattered by an incident neutron,
2. Measuring the energy of a charged particle emitted from a neutron-induced nuclear reaction,
3. Measuring the velocity of a neutron based on time-of-flight between two fixed points,
4. Deducing minimum neutron energies based on radioactive decay event detection, photon spectroscopy, and/or neutron thermalization,

5. Neutron spectrum unfolding using multiple detectors with unique neutron response characteristics,
6. Measuring the angular spread of neutrons to determine their energy (neutron diffraction), and
7. Measuring the time-distribution of the slowing down process of a pulse of neutrons.

Most advanced neutron spectrometers make use of one or more of the above techniques to determine incident neutron energy spectra. In general, neutron spectrometers are highly specialized for specific applications and the neutron energy range of interest. These factors in turn contribute to the form—the volume, mass, and portability—of the neutron spectrometer.

1.3.2 Neutron Spectrometers and Portability

Existing spectrometers generally possess undesirable characteristics that prevent them from being used for personal dosimetry and/or high-position-resolution area monitoring. Bonner Ball Neutron Detectors (BBNDs) are the most commonly used neutron spectrometer system for neutron dosimetry and radiation protection.¹² BBNDs consist of several spherical proportional counters encased with polyethylene spherical shells of varying thicknesses. Neutrons thermalized through the moderation process are counted by the proportional counters. Unfolding (also referred to as deconvolution or reconstruction) methods are used to reconstruct the incident neutron energy spectrum based on the unique neutron response functions associated with each Bonner sphere and the measurements made by each proportional counter. BBND systems are greatly extensible by adding more spheres with increased polyethylene thickness or replacing the polyethylene with denser materials to detect higher energy neutrons. Extreme BBND sets can measure isotropically distributed neutrons of energies ranging from 0.0253 eV to 1 GeV.¹³ BBNDs are not suitable for all applications, however. BBND sets are generally quite bulky, ranging from 5 cm to 46 cm diameter spheres, and hence unsuitable for personal dosimetry applications or fine-position resolution area monitoring.¹²

Portable, wide-energy-range, semiconductor-based neutron spectrometer designs heavily influenced by BBNDs were conceived and developed by Hoshor *et al.*¹⁴ This family of spectrometers still relies on neutron thermalization in polyethylene for detection but prioritizes portability. The spectrometer consists of a stack of Microstructured Semiconductor Neutron Detectors (MSNDs)¹⁵ separated by slabs of polyethylene to moderate neutrons. The detection relevant portion of the smallest cylindrical spectrometer design was fabricated at approximately 4 kg, a radius of 5.08 cm, and a length of 18 cm.¹⁴ Ultimately, this design is unsuitable for personal dosimetry due to its weight, handheld nature, and anisotropy.

Neutron spectrometers that rely mainly on neutron thermalization for neutron detection appear to exhibit improved performance for larger detector volumes because thermalizing high-energy neutrons is more likely to require multiple scattering interactions. Another neutron spectroscopy method is scintillation, in which the main detection mechanism is to facilitate the production of secondaries via nuclear interactions in the scintillator and then relate the measured light output to the incident neutron energy.¹⁶ Due to the difference in the detection mechanism, scintillator detectors are generally less dependent on volume than devices that rely on neutron thermalization. A portable, handheld Capture-Gated Neutron Scintillator Detector (CGNSD) is an example of a scintillator detector that separates gamma-ray and proton recoil contributions (which are more likely to deposit energies proportional to incident neutron energy) by “gating”, or pulse shape discrimination.¹⁷ This handheld spectrometer comprises an encased cylindrical volume of approximately 12 cm in diameter and 30 cm in length. Again, the handheld nature and size of this CGNSD is still not suitable for personal dosimetry or high position-resolution area monitoring. Another handheld device that relies on scintillation is the Proton Recoil Scintillator-Los Alamos (PRESCILA). PRESCILA is *not* a neutron spectrometer, but a handheld neutron “rem meter” that is capable of directly measuring the NCRP-38 dose equivalent rate¹⁸, a quantity that could feasibly be used for risk estimation, in real-time. With minor modifications to data post-processing, PRESCILA could measure the equivalent dose in real-time, which comes close to fulfill the stated purpose of the “ideal” neutron spectrometer described in Section 1.3. However, PRESCILA is approximately 2 kg in mass and 1125 cm³ in volume, which is still too

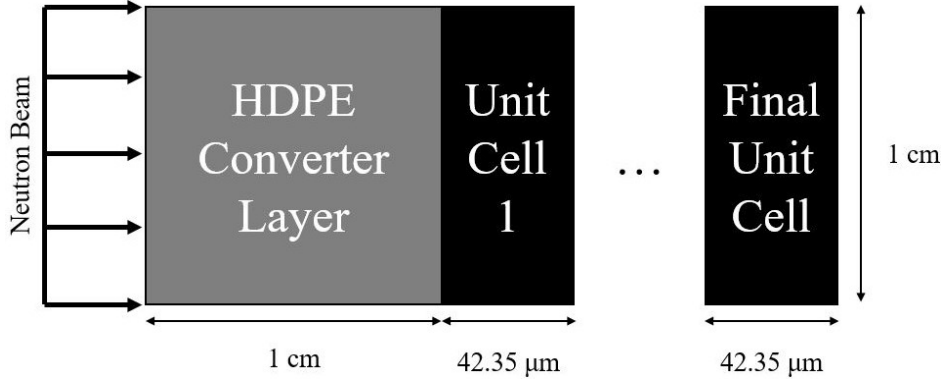


Figure 1.2: Overall PMFND structure; device is 1 cm thick.²¹

heavy to be attached to clothing, and too large for long-term dosimetry due to its handheld design.¹⁹

1.3.3 The Miniaturized Fast Neutron Detector

In response to the lack of a small neutron spectrometer designed for personal dosimetry and fine position-resolution area monitoring, a novel neutron spectrometer concept—the Miniaturized Fast Neutron Detector (MFND)—was conceived.²⁰ The acronym “MFND” will be used to generally refer to any miniature neutron spectrometer that relies on neutron-proton scattering interactions in a hydrogen-rich material to generate recoil protons that deposit energy in stacked layers of semiconductor detectors, independent of orientation or shape, and those stacked semiconductor detectors use the measured deposited energy to ultimately unfold the incident neutron energy spectrum, similar to Bonner sphere neutron spectroscopy. In the US patent application on the MFND concept by Bahadori and Leseman²⁰, a spherical MFND design is presented, producing an isotropic response. However, for computational, analytical, and conceptual simplicity, a planar prototype has been the subject of all MFND investigations up to this point and is the focus of this work. The planar prototype of the MFND (PMFND) was conceived to be a small, compact neutron spectrometer that relies on the detection of recoil protons by a stack of semiconductor diode detectors situated behind a high-density polyethylene (HDPE) neutron-to-proton conversion layer to estimate the incident neutron energy spectrum.²⁰ Figures 1.2 and 1.3 show the PMFND from the side. For

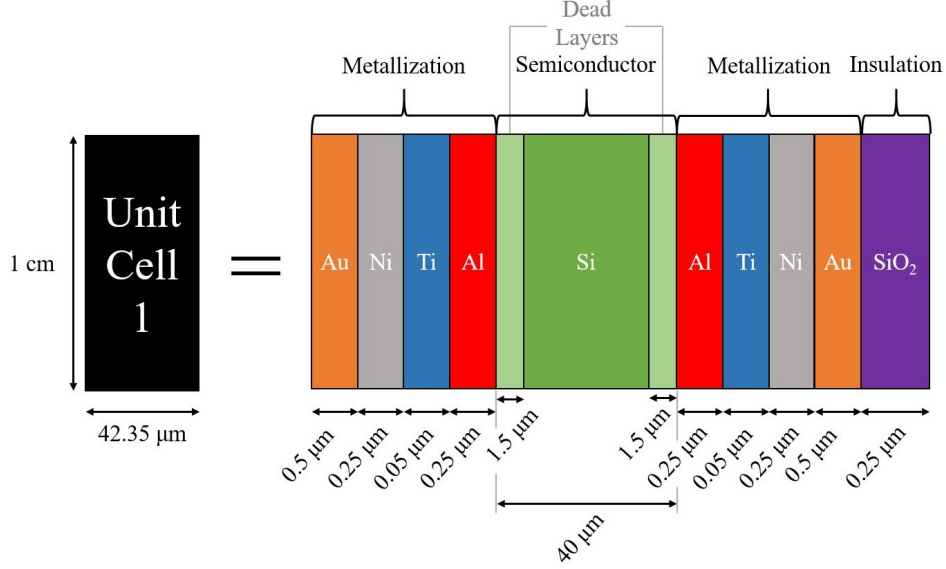


Figure 1.3: *Unit cell structure of PMFND.*²¹

a sense of scale, Figure 1.4 emphasizes the drastic size differences between the PMFND and previously mentioned neutron detectors. The PMFND is significantly smaller and lighter than existing neutron spectrometers. Despite the precise thicknesses shown in Figures 1.2 and 1.3, these values were determined based on the availability of materials and processes, not necessarily optimized to support the purpose of the PMFND. However, the PMFND remains modular in that unit cell detectors may vary in thickness. Equations and methods formulated in this work are meant to apply to a very general PMFND (with variable thicknesses for unit cell detectors, HDPE, etc.) and make the following assumptions about the characteristics of the general PMFND:

1. There are I unit cell detectors,
2. The metallization layers (thickness $\Delta z_{\text{met},i}$) and insulation layers (thickness $\Delta z_{\text{ins},i}$) for each unit cell detector all have identical dimensions throughout the PMFND,
3. The depth (into/out of page) Δx and height Δy of the PMFND is constant throughout the device,
4. The HDPE converter layer has depth Δz , and

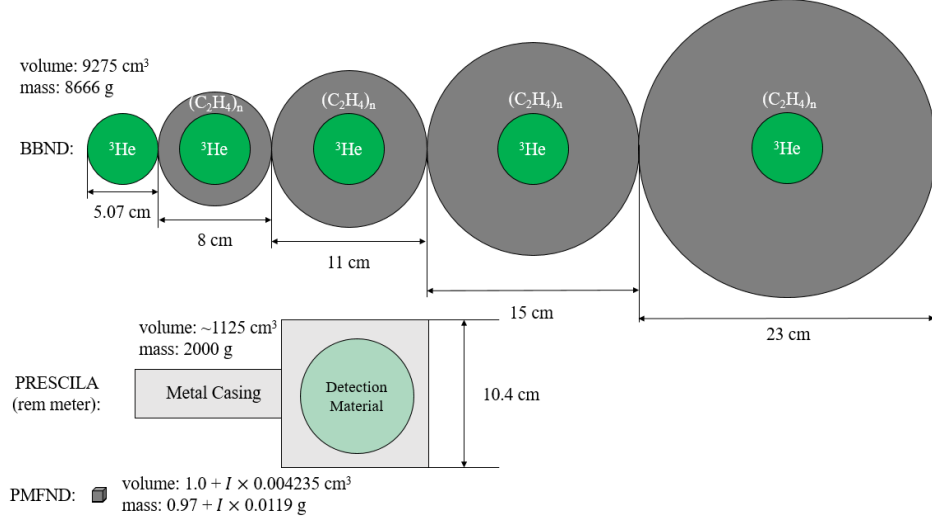


Figure 1.4: To-scale size comparison of BBNDs²², PRESCILA¹⁹, and the PMFND (excluding wires, readout equipment, etc.); I is the number of unit cell detectors in the PMFND detector stack.

5. The i -th Si detection region has two equally spaced “dead” regions (where energy deposition does not contribute to the signal produced) of depth $\Delta z_{\text{dead},i}$ and an active region of depth Δz_i .

Simulation results presented in this work are all based on a PMFND with dimensions as defined in Figures 1.2 and 1.3 and $I = 5$, $I = 20$, or $I = 55$ unit cell detectors (selected based on presumed fabrication practicality, optimizing spectroscopic information capture, or both); this will be clearly noted when necessary. All materials used to model the PMFND are given in Table 1.1 and remain consistent throughout this work.

1.4 Operational Overview of the PMFND

The spectroscopic information obtained from the PMFND ultimately facilitates the act of unfolding, or reconstructing, the incident neutron energy spectrum without *a priori* information in a range of diverse neutron environments. The process by which the PMFND measures the incident neutron energy spectrum is detailed here. Several mathematical details are omitted here, but will be included in subsequent sections. For now, consider a single neutron of initial kinetic energy E_n impinging upon the HDPE layer of the PMFND normal

Material	Density [g cm ⁻³]	Isotope	Atomic Fraction (%)
Si	2.330	²⁸ Si	92.2300
		²⁹ Si	4.6800
		³⁰ Si	3.0900
SiO ₂	2.200	²⁸ Si	30.7433
		²⁹ Si	1.5600
		³⁰ Si	1.0300
		¹⁶ O	66.6667
(C ₂ H ₄) _n (HDPE)	0.970	¹ H	66.6534
		² H	0.0133
		¹² C	33.3333
Au	19.320	¹⁹⁷ Au	100.0000
Ni	8.912	⁵⁸ Ni	68.0769
		⁶⁰ Ni	26.2231
		⁶¹ Ni	1.1399
		⁶² Ni	3.6345
		⁶⁴ Ni	0.9256
Ti	4.506	⁴⁶ Ti	8.2500
		⁴⁷ Ti	7.4400
		⁴⁸ Ti	73.7200
		⁴⁹ Ti	5.4100
		⁵⁰ Ti	5.1800
Al	2.700	²⁷ Al	100.0000

Table 1.1: *Materials and atomic compositions of PMFND.*²¹

to the left-facing surface shown in Figure 1.2. This neutron traverses some distance z_0 in the HDPE without interacting. The neutron interacts in the HDPE with some interaction coefficient $\mu(E_n)$. At the point of interaction, several types of neutron-induced interactions that may occur (displayed in Equations 2.36-2.38). The most common outcome is one where the neutron elastically scatters with a hydrogen atom, creating a recoil proton of energy

$$T = E_n \omega_r^2, \quad (1.9)$$

where E_n is the neutron kinetic energy, and ω_r is the cosine of the recoil scattering angle. This recoil proton continues through the PMFND and deposits energy in matter via direct ionization until the proton is stopped by Coulombic interactions and/or scattering. In the i -th active Si regions of the PMFND, the electron-hole pairs generated by ionization are separated and collected by electrodes on either side of the unit cell detector to compute the signal charge Q_i . The total signal charge is linearly proportional to the total energy deposited in region i , \mathcal{E}_i . It is the nature of charged particles to slow down non-linearly—that is, to deposit a majority of their energy over a short distance after depositing energy at a lower, nearly constant rate per unit distance for a relatively long distance (the shape of a Bragg curve).²³ This means that if a proton “stops” within active Si region i (highly likely considering the relative thickness of Si to the metallization layers and the insulation layer), then detector i accumulates a significant fraction of T . If recoil protons are mostly forward directed, $\theta_s \approx 0$, $E_n \approx T$ and the deposited energy in the i -th active Si region, \mathcal{E}_i scales with the incident neutron energy E_n . More energy is required for a recoil proton to reach deeper PMFND unit cell detectors. The total collected charge in a deeper unit cell detector is a measure of the number of sufficiently high-energy neutrons impinging upon the detector. In simple terms, this information is exploited by the PMFND to unfold a previously unknown neutron energy spectrum. Figures 1.5-1.8 illustrate the simplified process described in the preceding paragraph.

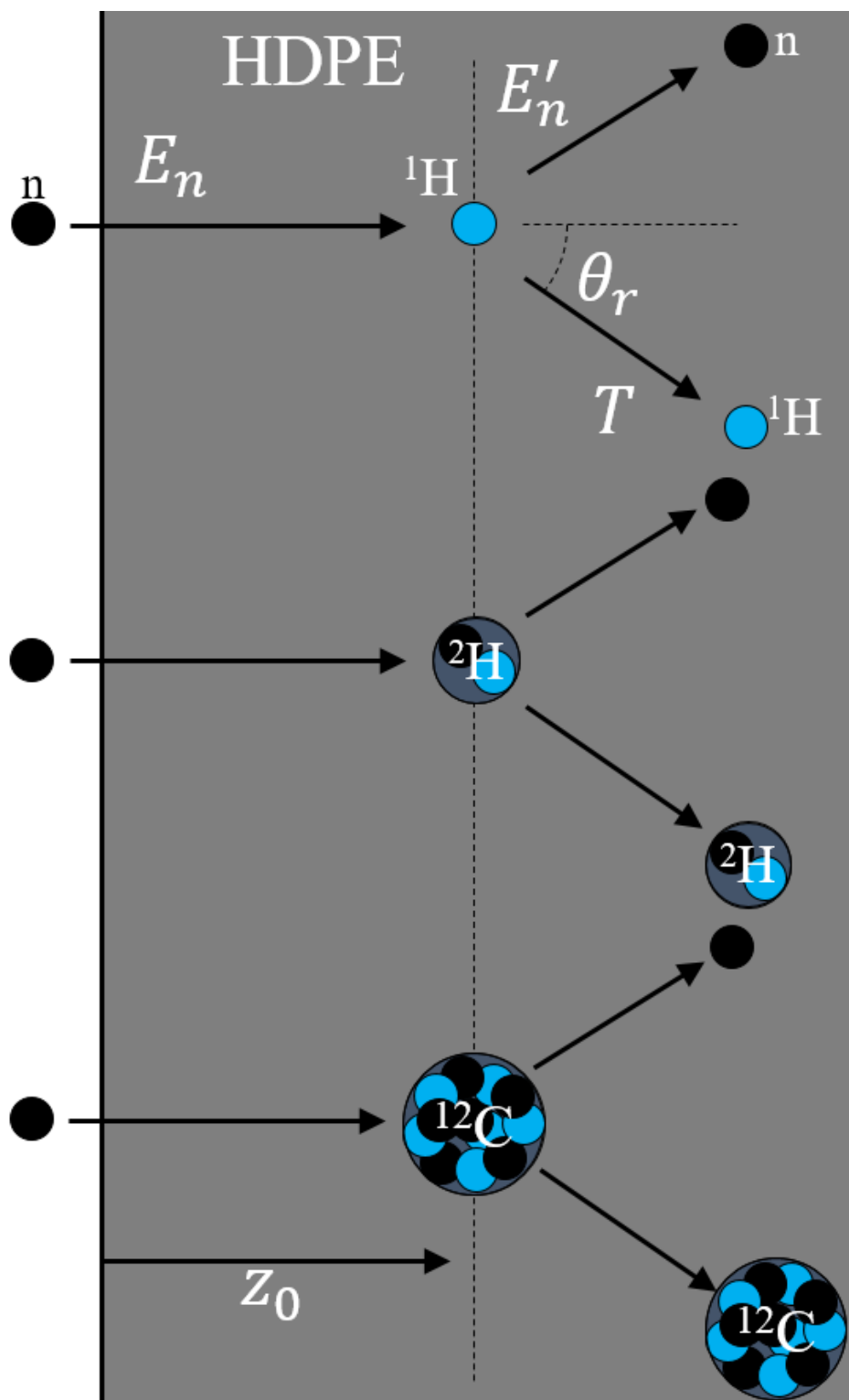


Figure 1.5: Depiction of possible elastic interactions that can occur in HDPE block; interactions occur at z_0 .

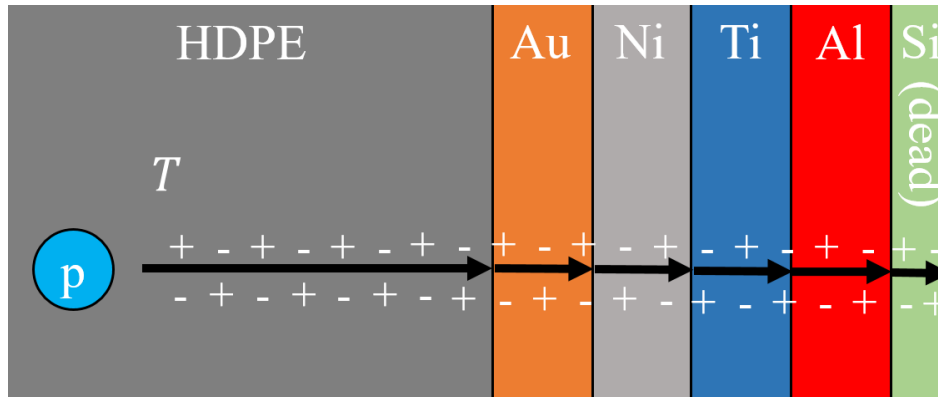


Figure 1.6: *Depiction of a proton (or any recoil ion) traversing through HDPE, metallization layers, and the dead region of the Si detection layer, ionizing the media and depositing energy along its path.*

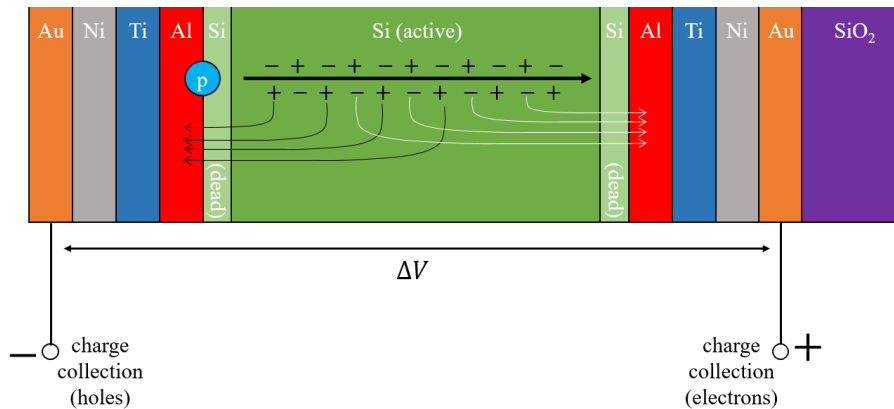


Figure 1.7: *Depiction of a proton (or any recoil ion) ionizing the active part of the Si detection region; the holes/electrons freed by ionization travel along/against electric field lines to ultimately be counted by charge collection devices; the unit cell detector is reverse biased with some voltage difference across the diode ΔV .*

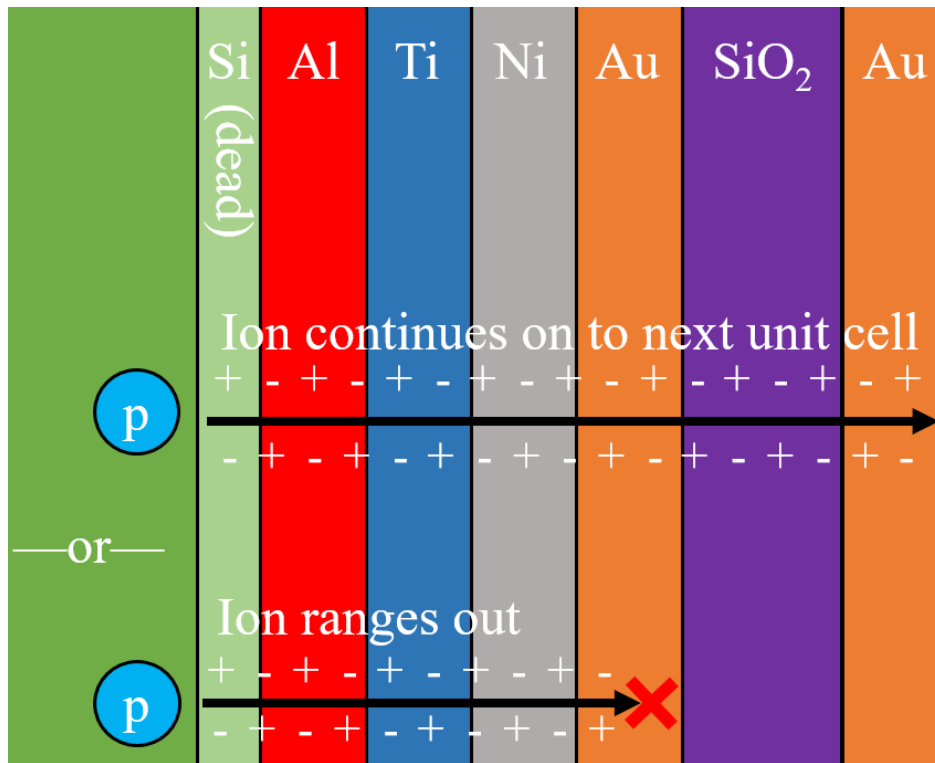


Figure 1.8: *Depiction of the possible paths a recoil proton (or any recoil ion) can take depending on the initial energy thereto imparted via scattering; low initial recoil energies will yield recoil ions that range out in shallow layers, high initial recoil energies will yield recoil ions that range out in deeper layers.*

1.5 Objective

The objective of this thesis is to computationally establish the suitability of the Planar Miniaturized Fast Neutron Detector (PMFND) for high spatial resolution neutron radiation risk estimation. Three substantial studies were carried out to develop an understanding and demonstrate the utility of the PMFND concept.

The main questions of the first study are

- Can the PMFND unfold an incident neutron energy spectrum without *a priori* information?
- How does changing the number of unit cell detectors change the PMFND's unfolding capability?
- Does one unfolding method provide better reconstructions of the incident neutron energy spectrum than the other?

The first study encompasses initial attempts to show that the PMFND is capable of unfolding an incident neutron energy spectrum. Particle and Heavy Ion Transport code System (PHITS)²⁴⁻²⁶ is used to generate statistically precise, well-resolved absorbed dose response functions for each unit cell detector as a function of neutron kinetic energy. Then, known neutron energy spectra are simulated in PHITS to generate simulated absorbed dose values for each unit cell detector. Attempts are made to reconstruct the incident neutron energy spectrum without considering the known incident spectrum. Two unfolding methods are compared for their ability to unfold the incident neutron energy spectrum: the non-negative least-squares method and the SPUNIT method. This study reflects the work presented in *Neutron Spectrum Unfolding with a Planar Miniaturized Fast Neutron Detector*.²⁷

The main questions of the second study are

- How can we quantitatively evaluate the effectiveness of the PMFND as a neutron spectrometer?
- How much neutron fluence is necessary to achieve acceptable unfolding results?

The second study seeks to define several quantitative measures of “effectiveness” of the PMFND. Effectiveness is essentially a metric that describes how closely the unfolded neutron energy spectrum matches up with the incident neutron energy spectrum, or how closely a quantity dependent on the unfolded neutron energy spectrum matches up with the same quantity dependent on the incident neutron energy spectrum. Three effectiveness measures are defined—radiometric, dosimetric, and biometric—and computed as a function of integral neutron fluence. Acceptable unfolding results are then defined by setting threshold values for each effectiveness measure, and the integral neutron fluence necessary to achieve acceptable unfolding results is determined by finding combinations of incident spectra and integral neutron fluence that produce effectiveness measures surpassing the requisite effectiveness thresholds. This study reflects the work shown in *Planar Miniaturized Fast Neutron Detector Spectroscopy Evaluation*.²¹

The main questions of the third study are

- How can the HDPE block be optimized to improve PMFND performance?
- How can the PMFND unit cells be optimized to improve performance?
- Can the concept of the PMFND be generalized for use in a wider range of neutron environments?

The third study expounds upon the physics that allow the PMFND to function, and suggests methods to optimize the device to improve its efficiency and effectiveness per unit fluence, and to generalize the device such that it can easily be modified for fundamentally different neutron environments.

Chapter 2

Methodology

This chapter discusses the methodology used to conduct all PMFND-related studies.

2.1 Tools

Several existing and newly built computational tools were used to carry out this work. The Particle and Heavy Ion Transport code System (PHITS)^{24–26} was used to conduct major radiation transport simulations involving the PMFND to test its ability to unfold incident neutron energy spectra and evaluate its effectiveness as a spectrometer. Stopping Power and Range of Ions in Matter (SRIM)²⁸ was used to conduct smaller scale, less precise, but fast radiation transport simulations meant to optimize various parts of the PMFND. The details of each code are discussed in this section.

2.1.1 PHITS

PHITS is a general purpose Monte Carlo particle transport code capable of simulating particle transport of all particle types over wide energy ranges. In this work, PHITS version 3.17 was used exclusively. PHITS offers an array of physics models that the user can enable or disable. The user specifies energy thresholds at which each particle type is no longer tracked through space. Other energy values determine when certain particle types adhere

	Neutron	Proton, Pion (other hadrons)	Nucleus	Muon	e^- / e^+	Photon	
	1 TeV		1 TeV/u			1 TeV	
High	Intra-nuclear cascade (JAM) + Evaporation (GEM) 3.0 GeV		JAMQMD + GEM	Virtual Photo-Nuclear JAM/ JQMD + GEM 200 MeV	EGS5	EPDL97 or EGS5	
↑ Energy	Intra-nuclear cascade (INCL4.6) + Evaporation (GEM) 20 MeV	d t ³ He α	Quantum Molecular Dynamics (JQMD) + GEM 10 MeV/u				Photo-Nuclear JAM/ JQMD + GEM + JENDL + NRF
↓ Low	Nuclear Data Library (JENDL-4.0) + EGM 0.1 meV	1 MeV	Ionization ATIMA	ATIMA + Original			
		1 keV		Muonic atom + Capture	**Track structure 1 meV	*Only in water	

Figure 2.1: *Default physics model map in PHITS 3.17.*²⁹

to particular physics models. Figure 2.1 from the PHITS 3.17 introductory presentation²⁹ displays the default settings for all physics models and all associated cutoff energies for each particle. Figure 2.2 shows the physics parameters set for all PHITS simulations in this work.

Appendix A shows a template for the “response function generation” PHITS simulations in this work. The [Parameters] card lists the physics parameters and energy cutoffs to be used in the associated particle transport simulation. The relevant physics models shown in Figure 2.2 are summarized here. The Japanese Evaluated Nuclear Data Library (JENDL-4.0) provides cross-section data for many nuclear interactions and typically covers a wider energy range than ENDF-VIII.0 for most interactions.³⁰ JENDL-4.0 is useful for space radiation transport simulations due to the high energies involved relative to terrestrial radiation. Neutron transport is primarily governed by PHITS’s event generator mode (version 2). The event generator ensures that energy and momentum are conserved for each neutron-induced reaction or event and allows for event-by-event energy deposition tallying.^{31;32} Semiconductor detection analysis requires this type of event-by-event energy deposition to simulate the way discrete charges are freed via ionization and swept to electrodes for counting. Two physics models govern proton transport. ATIMA calculates the stopping power and other quantities related to proton energy deposition for protons between 1 keV

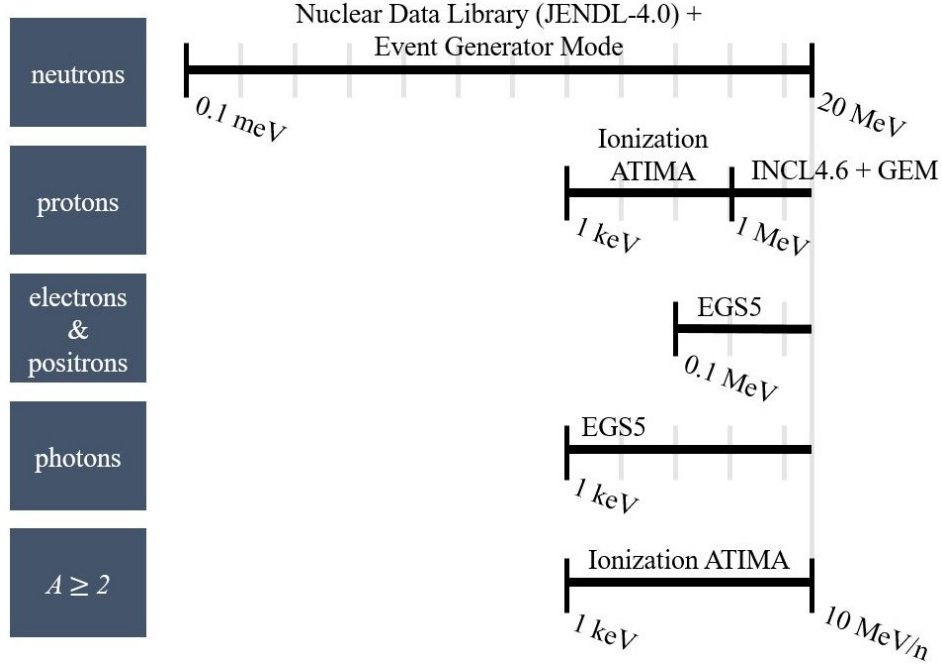


Figure 2.2: Graphical representation of physics models used as a function of particle type and energy in PMFND PHITS simulations.²¹

and 1 MeV.³³ ATIMA also governs all heavy ion transport, where the mass number $A \geq 2$. Intra-Nuclear Cascade of Liège (INCL) 4.6 + Generalized Evaporation Model (GEM) simulate proton-induced nuclear reactions and cascades.^{34;35} Electron-Gamma Shower (EGS5) code governs coupled electron, positron, and photon transport.³⁶ The Japan Atomic Energy Research Institute Quantum Molecular Dynamics (JQMD)-2.0 model accounts for relativistic effects.³⁷ All nucleon-nucleus collisions are computed using Sato’s formula.³⁸ Lynch’s formula from Moliere theory accounts for Coulomb diffusion.³⁹ Energy straggling is included via the Landau-Vavilov method.⁴⁰ Neutrons are only explicitly captured, meaning reduced-weight neutrons are *not* emitted after absorption. Transport ceases when particle kinetic energies fall below the minimum energies shown in Figure 2.2. Neutral particles that are not neutrons decay according to the decay mode specified in Table 4.5 of the PHITS 3.17 User Manual (displayed in Table 2.1).³¹

Decay Mode	Branching Ratio [%]	Lifetime [s]
$n \rightarrow p + e^- + \bar{\nu}_e$	100	8.867×10^2
$\pi^0 \rightarrow \gamma + \gamma$	100	0
$\pi^+ \rightarrow \mu^+ + \nu_\mu$	100	2.6029×10^{-8}
$\pi^- \rightarrow \mu^- + \bar{\nu}_\mu$	100	2.6029×10^{-8}
$\mu^+ \rightarrow e^+ + \nu_e + \bar{\nu}_\mu$	100	2.19703×10^{-6}
$\mu^- \rightarrow e^- + \bar{\nu}_e + \nu_\mu$	100	2.19703×10^{-6}
$K^0 \rightarrow \pi^+ + \pi^-$	68.31	8.922×10^{-11}
$K^0 \rightarrow \pi^0 + \pi^0$	31.39	8.922×10^{-11}
$K^0 \rightarrow \gamma + \gamma$	trace	8.922×10^{-11}
$K^+ \rightarrow \mu^+ + \nu_\mu$	63.51	1.2371×10^{-8}
$K^+ \rightarrow \pi^+ + \pi^0$	36.49	1.2371×10^{-8}
$K^- \rightarrow \mu^- + \bar{\nu}_\mu$	63.51	1.2371×10^{-8}
$K^- \rightarrow \pi^- + \pi^0$	36.49	1.2371×10^{-8}
$\eta \rightarrow \gamma + \gamma$	38.9	0
$\eta \rightarrow \pi^0 + \pi^0 + \pi^0$	31.9	0
$\eta \rightarrow \pi^+ + \pi^- + \pi^0$	23.7	0
$\eta \rightarrow \pi^+ + \pi^- + \gamma$	5.5	0
$\eta' \rightarrow \pi^+ + \pi^- + \eta$	44.1	0
$\eta' \rightarrow \pi^0 + \pi^0 + \eta$	20.5	0
$\eta' \rightarrow \pi^+ + \pi^- + \gamma$	30.1	0
$\eta' \rightarrow \gamma + \gamma$	5.3	0
$\Lambda \rightarrow p + \pi^-$	64.1	2.631×10^{-10}
$\Lambda \rightarrow n + \pi^0$	35.9	2.631×10^{-10}
$\Sigma^+ \rightarrow p + \pi^0$	51.57	7.99×10^{-11}
$\Sigma^+ \rightarrow n + \pi^+$	48.43	7.99×10^{-11}
$\Sigma^0 \rightarrow \Lambda + \gamma$	100	0
$\Sigma^- \rightarrow n + \pi^-$	100	1.479×10^{-10}
$\Xi^0 \rightarrow \Lambda + \pi^0$	100	2.90×10^{-10}
$\Xi^- \rightarrow \Lambda + \pi^-$	100	1.639×10^{-10}
$\Omega^- \rightarrow \Lambda + K^-$	67.8	8.22×10^{-11}
$\Omega^- \rightarrow \Xi^0 + \pi^-$	23.6	8.22×10^{-11}
$\Omega^- \rightarrow \Xi^- + \pi^0$	8.6	8.22×10^{-11}

Table 2.1: Decay modes, branching ratios, and average particle lifetimes for neutral subatomic particles (excluding neutrons due to the use of the event generator) according to PHITS 3.17 User Manual.³¹

2.1.2 SRIM

SRIM is a software package that computes quantities related to the stopping power and range of ions in matter using quantum mechanical methods.²⁸ SRIM is a fast, efficient way to estimate the stopping power of any heavy ion as a function of depth in a series of infinite slab layers of various materials defined by the user. When running TRIM, or Transport of Ions in Matter, which is the most robust transport mode included in the SRIM package, the user defines the incident ion, the initial kinetic energy of the ion, the angle of incidence of the ion, the width, density, and material composition of each infinite slab layer, and the type of TRIM calculation that the user desires. TRIM is a stochastic, Monte Carlo-esque calculation mode. For this work, the default “Ion Distribution and Quick Calculation of Damage” option was used for all TRIM calculations. This option utilizes the Kinchen-Pease damage model assumptions to determine the stopping power as a function of z , where the $+z$ -axis travels normal to the infinite slab surfaces. The major assumptions of the Kinchen-Pease model are that

1. All ion collisions are between two bodies and elastic,
2. Electronic stopping is ignored above a threshold energy, and
3. The orientation of the atomic lattice is ignored.⁴¹

SRIM is used in this work to develop stopping power profiles as a function of depth in the PMFND and ion range data in relevant compounds. SRIM was selected for PMFND optimization purposes over PHITS due to rapid calculation times, a diminished need for ultra-precise results, and ease of use. Figure 2.3 shows a representative example of a TRIM input used in this work. Inputting data into SRIM can be cumbersome—the program has no features to copy repetitive structures (such as the unit cell layers of the PMFND). Fortunately, *pysrim*, a Python package, was developed to bypass the pain of manually constructing geometry and materials layer by layer.⁴² Appendix B provides the Python code used to execute SRIM via *pysrim* for this work.

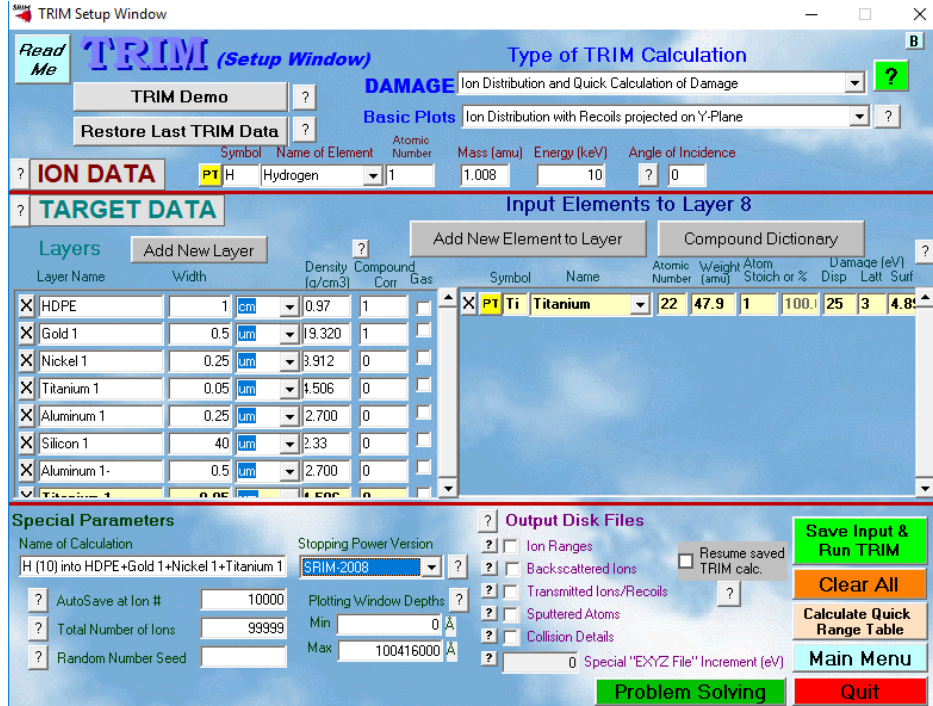


Figure 2.3: Representative TRIM input.²⁸

2.2 Unfolding the Incident Neutron Energy Spectrum

To “unfold” a spectrum is to solve, either analytically or by numerical approximation, the Fredholm integral equation of the first kind, or

$$g(y) = \int_a^b K(x, y)f(x)dx \quad (2.1)$$

for the spectrum $f(x)$. In general, $g(y)$ is some known quantity that is either measurable or computable for all y . The kernel function $K(x, y)$ is a Green’s function or an impulse response function. This section explains how the incident neutron energy spectrum is determined by using absorbed dose response functions and absorbed dose “measurements”. In short, this section shows how we solve for $\Phi(E_n)$ in

$$D_i = \int_0^\infty \mathcal{R}_i(E_n)\Phi(E_n)dE_n. \quad (2.2)$$

2.2.1 Absorbed Dose Response Function Generation

Fluence and dosimetric quantities are analytically related via *response functions*. In the most general sense, a response function $\mathcal{R}(\vec{Q}, \vec{P})$ is defined via

$$R(\vec{Q}) = \int_{\forall \vec{P}} \mathcal{R}(\vec{Q}, \vec{P}) \Phi(\vec{P}) d\vec{P}, \quad (2.3)$$

where $R(\vec{Q})$ is some response—a radiometric, dosimetric, or risk-related quantity—as a function of the variables contained within \vec{Q} . $\Phi(\vec{P})$ is the fluence distribution function (a distribution in \vec{P}). Response functions are specific to the physical situation at hand and can be used to *characterize* a physical situation. For example, in the case of the PMFND, absorbed dose response functions characterize the absorbed dose imparted to each active Si region per unit incident neutron fluence.

For the PMFND, the state variable vector is the position of interest, $\vec{Q} = \vec{r}$. Because there are a finite number of active Si regions where the imparted absorbed dose is measured, the position vector \vec{r} may be replaced with the index i to indicate the index of the relevant detection region, as numbered in Figure 1.2. The response is the absorbed dose D_i and the integration variable vector is $\vec{P} = \langle E_n, \vec{\Omega} \rangle$. E_n represents neutron kinetic energy and $\vec{\Omega}$ represents the solid angle vector. Once simplified, Equation 2.3 becomes

$$D_i = \int_{4\pi} \int_0^\infty \mathcal{R}_i(E_n, \vec{\Omega}) \Phi(E_n, \vec{\Omega}) dE_n d\Omega. \quad (2.4)$$

As Equation 2.4 shows, there is a unique absorbed dose response function for each detection region. Each response function can be determined by probing the response of the PMFND via Monte Carlo simulation with a known incident fluence spectrum for a range of neutron energies (and directions, if an isotropic response is desired). Let the incident fluence distribution be a mono-directional ($\vec{\Omega}_0$), mono-energetic (E_j) neutron beam,

$$\Phi(E_n, \vec{\Omega}) = \Phi_0 \delta(E_n - E_j) \delta(\vec{\Omega} - \vec{\Omega}_0), \quad (2.5)$$

where Φ_0 is the integral neutron fluence magnitude, which is simply

$$\Phi_0 = \frac{N_p}{A_{\text{PMFND}}}, \quad (2.6)$$

where N_p is the number of histories per PHITS simulation, and A_{PMFND} is the cross-sectional area ($\Delta x \times \Delta y$) of the PMFND. Substitution into Equation 2.4 yields

$$D_i(E_j) = \Phi_0 \mathcal{R}_i(E_j, \vec{\Omega}_0), \quad (2.7)$$

which can be rearranged to become

$$\mathcal{R}_i(E_j, \vec{\Omega}_0) = \frac{D_i(E_j)}{\Phi_0}. \quad (2.8)$$

Absorbed dose response functions are built using Equation 2.8. $\vec{\Omega}_0$ is set to be a direction normal to the HDPE surface, since the PMFND is not meant to be an isotropic detector. The absorbed dose in each detection region D_i as a function of E_j can be determined in reality via direct measurement or computationally estimated via Monte Carlo simulation.

2.2.2 Computing the Absorbed Dose

The absorbed dose D_i for the i -th unit cell detector is defined as the average energy imparted \mathcal{E}_i per unit mass m_i of the active Si detection region,

$$D_i = \frac{\mathcal{E}_i}{m_i}. \quad (2.9)$$

2.2.2.1 Absorbed Dose via Measurement

When D_i is determined via measurement, the average energy deposited is found by integrating the total collected current dQ_i/dt in the active Si detection region,

$$Q_i = \int_0^\infty \frac{dQ_i}{dt} dt, \quad (2.10)$$

and converting the total collected charge Q_i to deposited energy via

$$\mathcal{E}_i = \frac{w_{\text{Si}}}{e} Q_i, \quad (2.11)$$

where $w_{\text{Si}} \approx 3.6 \text{ eV}$ is the average energy required to produce an electron-hole pair in silicon and e is the elementary charge. Equation 2.9 is then used to compute the absorbed dose D_i .

2.2.2.2 Absorbed Dose due to Mono-energetic Neutrons for “Response” Simulations

To compute the absorbed dose D_i as a function of all E_j and ultimately use Equation 2.8 to build the absorbed dose response functions, a series of 201 ($J + 1 = 201$) radiation transport simulations were conducted using PHITS. Details on specific transport models, approximations, and parameters are discussed in Section 2.1.1. These simulations are referred to as “response” simulations for ease of distinction. The simulation geometry is comprised of a $I = 20$ -layered PMFND with cross-sectional area $A_{\text{PMFND}} = 1 \text{ cm}^2$ as described in Figures 1.2-1.3. The source is a square, mono-directional, mono-energetic beam of neutrons with initial kinetic energy E_j for $j = 0, 1, \dots, J$. The source and front face of the HDPE block are centered at the point $(0, 0, -0.01) \text{ cm}$. The source is directed along the $+z$ -axis as shown in Figure 2.5. The energy $E_0 = 2.53 \times 10^{-8} \text{ MeV}$, or the energy of a thermal neutron. Energies E_1 through E_J adhere to the formula

$$E_j = (0.1 \text{ MeV})j, \quad (2.12)$$

such that E_1 through E_J are distributed evenly over the interval $[0.1, 20.0] \text{ MeV}$. $N_p = 775 \times 10^6$ neutrons make up the source for each “response” simulation.

Each active Si detection region is designated as a tally region using the [T - Deposit] tally function. Within each active Si detection region, the number deposition $N_i(\mathcal{E})$ is tallied as a function of deposition energy \mathcal{E} . $N_i(\mathcal{E})$ represents the fraction of source neutrons that deposit some amount of energy $\mathcal{E} \in (\mathcal{E}_{\text{low},k}, \mathcal{E}_{\text{high},k}]$ in detection region i . 2000 linearly-spaced

deposition energy bins, with the smallest bin edge being $\mathcal{E}_{\text{low},1} = 0$ and the greatest being $\mathcal{E}_{\text{high},2000} = 20$ MeV, are used for the tally. To be precise, the exact data that PHITS provides post-simulation is the number deposition distribution, where the k -th deposition energy bin stores the number deposition value $N_{i,k}$. PHITS output data were structured in this way to take into account a *charge threshold* introduced by the eventual PMFND manufacturer, Q_{th} . This charge threshold value would be used for device tuning, reducing system noise, and at minimum would serve as a minimum detectable charge, below which no signal would register in the detector. The charge threshold translates to an energy threshold via

$$\mathcal{E}_{\text{th}} = \frac{w_{\text{Si}}}{e} Q_{\text{th}}. \quad (2.13)$$

Ultimately, in this work, the charge thresholding feature was never fully explored, so $Q_{\text{th}} = 0$. The total energy deposited in the active Si detection region of unit cell detector i is given by

$$\mathcal{E}_i = \frac{1}{2} \sum_{k \ni \mathcal{E}_{\text{low},k} \geq \mathcal{E}_{\text{th}}} (\mathcal{E}_{\text{low},k} + \mathcal{E}_{\text{high},k}) N_{i,k}. \quad (2.14)$$

Once \mathcal{E}_i is computed, Equations 2.6 and 2.8 are used to compute the response function $\mathcal{R}_i(E_j, \vec{\Omega}_0)$. The input file template for the “response” PHITS simulation is given in Appendix A.

2.2.2.3 Absorbed Dose due to Neutron Energy Spectrum for “Dose” Simulations

Similar methods as those described in the previous section were used to compute the absorbed dose in each unit cell detector when the source consists of a distribution of neutron energies. For purposes of testing the ability of the PMFND to successfully unfold incident neutron energy spectra, and to determine the integral neutron fluence required to obtain acceptable unfolding results, 720 PHITS “dose” simulations were performed. Three different incident neutron energy spectra, Watt ^{252}Cf , AmB, and AmBe, were selected for testing. Figure 2.4 shows these incident neutron energy spectra. The International Organization for

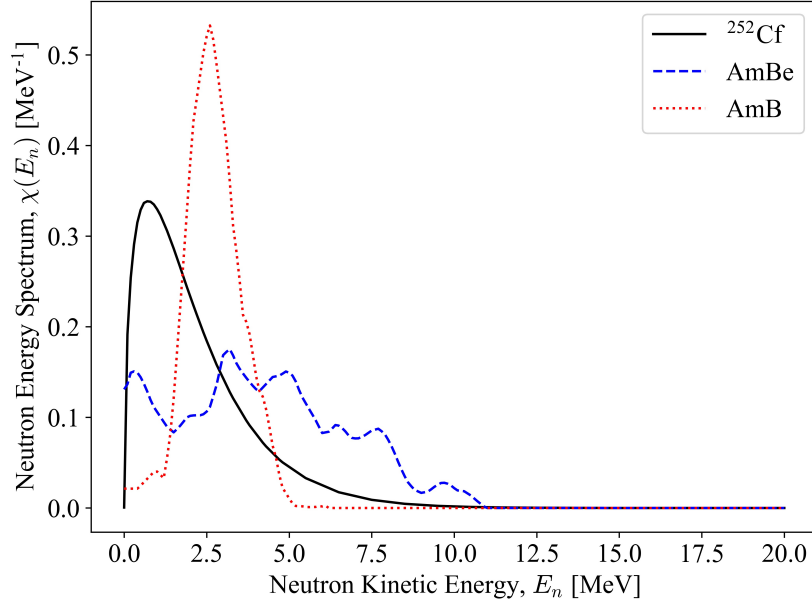


Figure 2.4: ^{252}Cf , AmB , and AmBe ISO differential neutron energy spectra.⁴³

Standardization (ISO) neutron spectra data were used.⁴³ The number of source neutrons was varied in otherwise identical “dose” simulations to observe how spectrometer effectiveness metrics and unfolded neutron spectra results change as integral neutron fluence Φ increases.

2.2.3 Unfolding Methods

Unfolding methods are used to solve Equation 2.2 for $\Phi(E_n)$. All practical unfolding methods are numerical procedures and require some discretization of Equation 2.2. Equation 2.2 is discretized via

$$D_i = \sum_{j=1}^J \mathcal{R}_i(E_j) \Phi(E_j) \Delta E_j, \quad (2.15)$$

where $\Delta E_j = E_j - E_{j-1}$. Equation 2.15 can be made into a vector equation, which is computationally preferable, by letting \vec{D} be an I -element vector with elements D_i (I referring to the number of Si detectors), $\vec{\Phi}$ be a J -element vector with elements $\Phi(E_j) \Delta E_j$, and \mathcal{R} be

an $I \times J$ matrix with elements $\mathcal{R}_i(E_j)$. The resulting matrix equation is

$$\vec{D} = \mathcal{R}\vec{\Phi}. \quad (2.16)$$

2.2.3.1 Non-Negative Least Squares Unfolding Method

The non-negative least squares (NNLS) unfolding method approximates the solution of $\Phi(E_n)$ in Equation 2.2 by finding a suitable solution to Equation 2.16. Formally, the energy-dependent neutron fluence vector is computed using

$$\vec{\Phi} = \arg \min_{\vec{\Phi}} \|\mathcal{R}\vec{\Phi} - \vec{D}\|_2 \text{ subject to } \vec{\Phi} \geq \vec{0}. \quad (2.17)$$

Equation 2.17 is mathematical shorthand for “find $\vec{\Phi}$ that minimizes the L_2 -norm of $\mathcal{R}\vec{\Phi} - \vec{D}$ where element Φ_j is positive for all j ”. The physical constraint $\vec{\Phi} \geq \vec{0}$ is necessary because the concept of negative fluence is nonphysical. `scipy.optimize.nnls`, found within Python’s SciPy package, is the NNLS algorithm used to carry out Equation 2.17.^{44;45}

Typically, the number of neutron energies used to generate response functions is much larger than the number of unit cell detectors in the PMFND, $J \gg I$. There are infinitely many solutions for the elements of $\vec{\Phi}$ in Equation 2.16 when $J > I + 1$ because there are fewer equations than there are unknowns, e.g.,

$$\begin{aligned} D_1 &= \mathcal{R}_1(E_1)\Phi(E_1)\Delta E_1 + \cdots + \mathcal{R}_1(E_j)\Phi(E_j)\Delta E_j + \cdots + \mathcal{R}_1(E_J)\Phi(E_J)\Delta E_J \\ &\vdots \\ D_i &= \mathcal{R}_i(E_1)\Phi(E_1)\Delta E_1 + \cdots + \mathcal{R}_i(E_j)\Phi(E_j)\Delta E_j + \cdots + \mathcal{R}_i(E_J)\Phi(E_J)\Delta E_J \\ &\vdots \\ D_I &= \mathcal{R}_I(E_1)\Phi(E_1)\Delta E_1 + \cdots + \mathcal{R}_I(E_j)\Phi(E_j)\Delta E_j + \cdots + \mathcal{R}_I(E_J)\Phi(E_J)\Delta E_J. \end{aligned}$$

This means that, while the NNLS algorithm of Equation 2.17 will eventually populate a feasible $\vec{\Phi}$ that satisfies Equation 2.16 to within some pre-specified tolerance, the resulting

$\vec{\Phi}$ is likely to yield a *local* minimum value of $\|\mathcal{R}\vec{\Phi} - \vec{D}\|_2$ instead of the *global* minimum. In terms of the unfolded neutron energy spectrum, this usually means that the unfolded spectrum does not closely follow the incident neutron energy spectrum without significant, spectral shape-altering noise. However, modifying the response function matrix can help to reduce this noise.

Carrying out Equation 2.17 without first modifying the response function matrix \mathcal{R} or the structure of the integral fluence vector $\vec{\Phi}$ yields the highest possible energy resolution of the unfolded neutron energy spectrum, but the unfolded spectrum often does not resemble the incident spectrum without significant noise. To remedy this, the response function matrix \mathcal{R} is manually modified from an $I \times J$ matrix to an $I \times M$ matrix, where $M < J$ and $M \sim I$. This modification is carried out by averaging collections of energy-adjacent values of each response function, say $\mathcal{R}_i(E_{j-1})$, $\mathcal{R}_i(E_j)$, and $\mathcal{R}_i(E_{j+1})$, assigning a new energy index m , and using this average to populate a modified, $I \times M$ response function matrix \mathcal{R}_{AV} .

Formally, the transformation of $\mathcal{R} \mapsto \mathcal{R}_{AV}$ is accomplished via

$$\mathcal{R}_{AV,i}(E_m) = \frac{1}{\Delta E_m} \sum_{j \ni \{E_{\text{low},m} \leq E_j < E_{\text{high},m}\}} \mathcal{R}_i(E_j) \Delta E_j, \quad (2.18)$$

where $\Delta E_m = E_{\text{high},m} - E_{\text{low},m}$. Only the values of $E_{\text{low},m}$ and $E_{\text{high},m}$ are user-selected and tend to improve the unfolding performance when updated energy bin edges are concentrated near locations where the incident neutron energy spectrum changes quickly. The energy-grouping process reduces the number of columns from J to M . The transformation $\mathcal{R} \mapsto \mathcal{R}_{AV}$ causes a decrease in the resolution of the unfolded neutron energy spectrum. The integral fluence vector is directly affected, as it too must transform from $\vec{\Phi} \mapsto \vec{\Phi}_{AV}$ changing from a length J vector to a length M vector with elements of the form $\Phi_{AV}(E_m) \Delta E_m$. The NNLS algorithm is completed when the unfolded fluence vector is converted to a true neutron spectrum vector with units MeV^{-1} ,

$$F(E_m) = A_{\text{PMFND}} \frac{\Phi_{AV}(E_m)}{\Delta E_m}. \quad (2.19)$$

2.2.3.2 SPUNIT Unfolding Method

The SPUNIT algorithm is an iterative method designed to unfold neutron energy spectra.⁴⁶ The algorithm requires an initial absorbed dose vector \vec{D}^0 obtained via simulation or measurement, a response matrix \mathcal{R} , an initial guess neutron fluence spectrum vector $\vec{\Phi}^0$, and some termination parameter that can be specified by the user. For generality, the SPUNIT method is presented here considering a maximum number of iterations N_{it} , but the method is easily modified for any reasonable convergence criterion, such as a rate of change threshold.

The initial guess fluence spectrum $\vec{\Phi}^0$ is set to a flat differential neutron energy spectrum that spans the energy range from 2.53×10^{-8} MeV to 20 MeV to maintain the prospect that unknown incident neutron energy spectra can be unfolded without *a priori* knowledge. The flat guess spectrum vector is defined as

$$\vec{\Phi}^0 = \frac{\vec{1}}{JA_{\text{PMFND}}}. \quad (2.20)$$

The SPUNIT algorithm generates a prediction of the incident neutron energy spectrum iteratively. The n -th iteration of the i -th absorbed dose vector element \tilde{D}_i^n is given by

$$\tilde{D}_i^n = \sum_{j=0}^J \mathcal{R}_i(E_j) \Phi_j^n, \quad (2.21)$$

and the $(n+1)$ -th iteration of the neutron fluence spectrum vector for energy E_j is given as

$$\Phi_j^{n+1} = \Phi_j^n \frac{\sum_i \mathcal{R}_i(E_j) / \tilde{D}_i^n}{\sum_i \mathcal{R}_i(E_j) / D_i^0}. \quad (2.22)$$

After N_{it} iterations, the unfolded fluence vector is normalized by multiplying by the cross-sectional area of the PMFND A_{PMFND} and dividing by the j -th energy bin width ΔE_j to produce the unfolded neutron energy spectrum vector \vec{F} ,

$$F(E_j) = A_{\text{PMFND}} \frac{\Phi_j^{N_{\text{it}}}}{\Delta E_j}. \quad (2.23)$$

2.3 Characterizing Spectrometer Effectiveness

Three PMFND spectrometer effectiveness metrics were developed. Each is discussed in this section.

2.3.1 Radiometric Spectrometer Effectiveness

The radiometric spectrometer effectiveness refers to the degree to which the PMFND is able to reconstruct the incident neutron energy spectrum—or the overall correlation between $F(E_n)$ and $\chi(E_n)$. The radiometric spectrometer effectiveness ε_1 is defined as the squared correlation coefficient associated with the incident neutron energy spectrum $\chi(E_j)$ and the unfolded neutron energy spectrum $F(E_j)$ for $j = 0, \dots, J$,

$$\varepsilon_1 = \left[\frac{\sum_{j=0}^J [\chi(E_j) - \bar{\chi}] [F(E_j) - \bar{F}]}{\sqrt{\sum_{j=0}^J [\chi(E_j) - \bar{\chi}]^2} \sqrt{\sum_{j=0}^J [F(E_j) - \bar{F}]^2}} \right]^2. \quad (2.24)$$

$\bar{\chi}$ and \bar{F} are the average values of the incident neutron energy spectrum and the average value of the unfolded neutron energy spectrum respectively, integrated over the range $E_n \in [E_0, E_J]$,

$$\bar{\chi} = \frac{1}{E_J - E_0} \int_{E_0}^{E_J} \chi(E_n) dE_n \approx \frac{1}{E_J - E_0} \sum_{j=0}^J \chi(E_j) \Delta E_j, \quad (2.25)$$

and

$$\bar{F} = \frac{1}{E_J - E_0} \int_{E_0}^{E_J} F(E_n) dE_n \approx \frac{1}{E_J - E_0} \sum_{j=0}^J F(E_j) \Delta E_j. \quad (2.26)$$

ε_1 is conveniently scale invariant and has a domain of $\varepsilon_1 \in [0, 1]$. As the radiometric spectrometer effectiveness increases, the unfolded neutron energy spectrum approaches the incident neutron energy spectrum, i.e., $\varepsilon_1 \rightarrow 1$, $F(E_n) \rightarrow \chi(E_n)$. On the other hand, as $\varepsilon_1 \rightarrow 0$, the reconstructed neutron energy spectrum approaches a function of a constant value and $F(E_n)$ is devoid of any useful spectroscopic information. From a statistical perspective, the squared correlation coefficient measures the relative movement between two sets of random

variables. $\chi(E_n)$ and $F(E_n)$ are non-zero and are normalized such that

$$\sum_{j=1}^J \chi(E_j) \Delta E_j = 1, \quad (2.27)$$

and

$$\sum_{j=1}^J F(E_j) \Delta E_j = 1. \quad (2.28)$$

Due to these restrictions on $\chi(E_n)$ and $F(E_n)$, the associated correlation coefficient is a measure of both the correlation and *mathematical similarity*—or the visual agreement—between $\chi(E_n)$ and $F(E_n)$.

2.3.2 Dosimetric Spectrometer Effectiveness

The dosimetric spectrometer effectiveness is the degree to which the absorbed dose in each unit cell detector computed directly from the incident neutron energy spectrum $\chi(E_n)$ agree with the absorbed dose in each unit cell detector computed directly from the unfolded neutron energy spectrum $F(E_n)$. The coefficient of determination is used to define the dosimetric spectrometer effectiveness ε_2 ,

$$\varepsilon_2 = 1 - \frac{\sum_{i=1}^I (D_i - D_i^r)^2}{\sum_{i=1}^I (D_i - \bar{D})^2}, \quad (2.29)$$

where D_i is the absorbed dose expected from folding the true incident neutron energy spectrum $\chi(E_n)$ with response function $\mathcal{R}_i(E_n)$,

$$D_i = \frac{1}{A_{\text{PMFND}}} \int_0^\infty \mathcal{R}_i(E_n) \chi(E_n) dE_n, \quad (2.30)$$

\bar{D} is the average absorbed dose in each unit cell detector,

$$\bar{D} = \frac{1}{I} \sum_{i=1}^I D_i, \quad (2.31)$$

and D_i^r is the refolded absorbed dose, or the absorbed dose computed using the unfolded neutron energy spectrum $F(E_n)$, i.e.,

$$D_i^r = \frac{1}{A_{\text{PMFND}}} \int_0^\infty \mathcal{R}_i(E_n) F(E_n) dE_n \approx \frac{1}{A_{\text{PMFND}}} \sum_{j=0}^J \mathcal{R}_i(E_j) F(E_j) \Delta E_j. \quad (2.32)$$

The dosimetric spectrometer effectiveness can take on values $\varepsilon_2 \in (-\infty, 1]$. Similar to the radiometric spectrometer effectiveness, $\varepsilon_2 = 1$ signals perfect agreement between D_i and D_i^r values—100% of the variability in the expected absorbed dose values is explained by the refolded absorbed dose values. $\varepsilon_2 = 0$ means that the average expected absorbed dose value \bar{D} explains exactly as much variability in D_i as D_i^r . Negative values of ε_2 indicate that the refolded absorbed dose is highly inaccurate with respect to the expected absorbed dose.

2.3.3 Biometric Spectrometer Effectiveness

The biometric spectrometer effectiveness, ε_3 , is the degree to which the ambient dose equivalent⁹ $H^*(10 \text{ mm})$ computed from the incident neutron energy spectrum $\chi(E_n)$ agrees with the refolded ambient dose equivalent $H_r^*(10 \text{ mm})$ computed from the unfolded neutron energy spectrum $F(E_n)$. The ambient dose equivalent $H^*(10 \text{ mm})$ is defined as the dose equivalent at a point in a radiation field that would be produced by the corresponding expanded and aligned field in the International Commission on Radiation Limits and Measurements sphere at a depth of 10 mm on the radius vector opposing the direction of the aligned field.⁹ ε_3 is defined as unity minus the relative error between some measure of biological hazard, or more broadly “risk”, computed from the incident neutron energy spectrum and the same measure of risk computed from the unfolded neutron energy spectrum. In this case, the ambient dose equivalent $H^*(10 \text{ mm})$ is selected as the radiobiological metric. That is,

$$\varepsilon_3 = 1 - \left| \frac{H_r^*(10 \text{ mm}) - H^*(10 \text{ mm})}{H^*(10 \text{ mm})} \right|, \quad (2.33)$$

where $H_r^*(10\text{ mm})$ is the refolded ambient dose equivalent given by

$$H_r^*(10\text{ mm}) = \int_0^\infty \mathcal{R}_H(E_n)F(E_n)dE_n \approx \sum_{j=0}^J \mathcal{R}_H(E_j)F(E_j)\Delta E_j, \quad (2.34)$$

where $\mathcal{R}_H(E_n)$ is the 1996 ambient dose equivalent response function, linearly interpolated from Table A. 42 of ICRP 74.⁴⁷ Similarly, $H^*(10\text{ mm})$ is the ambient dose equivalent due to the incident neutron energy spectrum, given by

$$H^*(10\text{ mm}) = \int_0^\infty \mathcal{R}_H(E_n)\chi(E_n)dE_n \approx \sum_{j=0}^J \mathcal{R}_H(E_j)\chi(E_j)\Delta E_j. \quad (2.35)$$

The biometric spectrometer effectiveness takes on values $\varepsilon_3 \in (-\infty, 1]$. The biometric spectrometer effectiveness is simple to interpret. As $\varepsilon_3 \rightarrow 1$, the refolded ambient dose equivalent value approaches the ambient dose equivalent due to the incident neutron energy spectrum, $H_r^*(10\text{ mm}) \rightarrow H^*(10\text{ mm})$. For $\varepsilon_3 \leq 0$, the relative error between $H^*(10\text{ mm})$ and $H_r^*(10\text{ mm})$ is at least 100%.

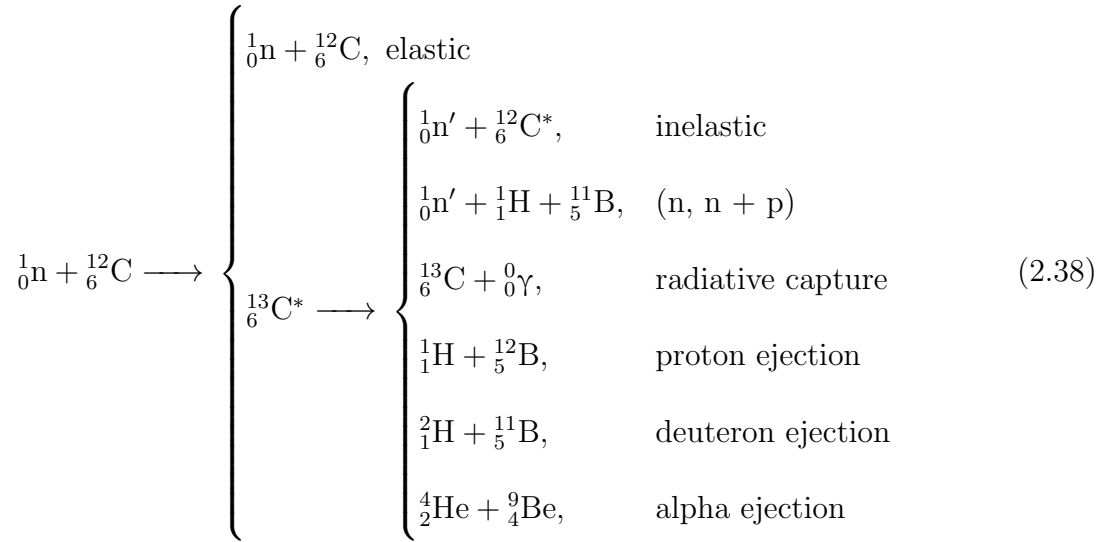
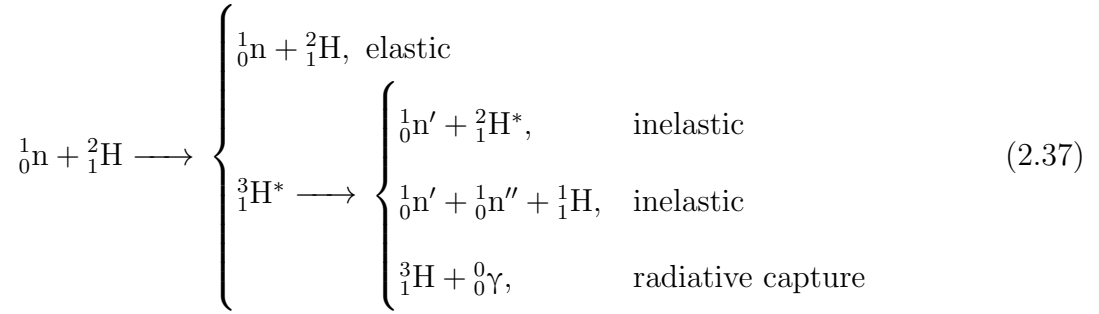
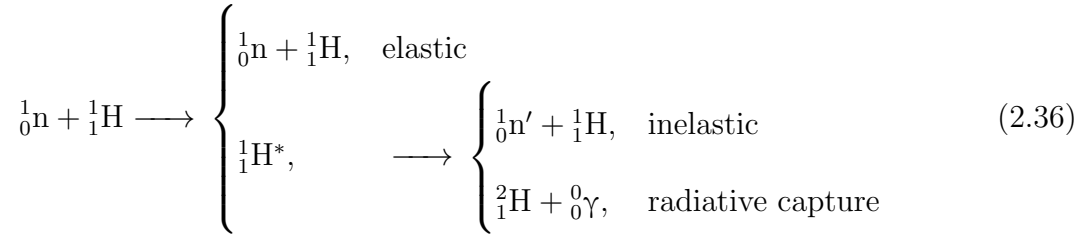
2.4 Optimizing the PMFND for Future Studies

2.4.1 HDPE Block Optimization

The material composition and physical dimensions of the neutron-proton conversion layer significantly affects both the effectiveness and efficiency of the PMFND as neutron spectrometer. During the initial design of the PMFND, a 1 cm^3 cube of HDPE was chosen to virtually test the PMFND's capabilities via Monte Carlo simulations. This choice was made based on experience, not optimization. Since then, methods were devised to characterize the probability that the neutron-proton conversion layer emits an ion that eventually reaches the first metallization layer of the PMFND (and thus has a chance of contributing to the signal of one or more unit cell detectors).

2.4.1.1 Possible Reactions

Nuclear reactions 2.36-2.38 summarize most of the interactions that can take place when an energetic neutron enters a medium comprised of HDPE, or $(C_2H_4)_n$. Hydrogen and carbon have only two appreciable, naturally occurring isotopes each: 1_1H , 2_1H , $^{12}_6C$, and $^{13}_6C$.



The presumed natural abundances of each isotope are shown in Table 2.2.

Isotope	Natural Abundance
^1_1H	0.99985
^2_1H	0.00015
$^{12}_6\text{C}$	1.0

Table 2.2: *Isotopes present in HDPE alongside natural abundance fractions.*

2.4.1.2 Probability of Neutron-Scattered Ion Reaching Detection Region

The probability, $P(x_0, y_0, z_0|E_n, \Delta x, \Delta y, \Delta z)$, that a normally incident neutron with kinetic energy E_n initially interacts at location (x_0, y_0, z_0) in the HDPE block and scatters an ion that exits the back face of the HDPE block (at $z = \Delta z$) is sought for HDPE block optimization purposes. Figure 2.5 clarifies HDPE dimensions and variable assignment. Δx , Δy , and Δz refer to the width, length, and depth of the HDPE block respectively. Note that multiple neutron scattering is not considered in this formulation.

The probability $P(x_0, y_0, z_0|E_n, \Delta x, \Delta y, \Delta z)$ can be broken down into a number of independent constituent probability functions that, when multiplied, develop the joint probability function $P(x_0, y_0, z_0|E_n, \Delta x, \Delta y, \Delta z)$. These functions are uncovered by examining the sequence of events necessary for a scattered ion to reach the back face of the HDPE block. First, the incident neutron, which starts from $(x_0, y_0, 0)$ must travel through the HDPE block along the z -direction and reach (x_0, y_0, z_0) without interacting in HDPE. Second, the interaction that occurs at (x_0, y_0, z_0) must be an interaction that produces a recoil ion—typically, a scattering interaction. Finally, the scattered recoil ion must travel from (x_0, y_0, z_0) to the plane $z = \Delta z$ and remain restricted to the domain $\mathcal{D} = \{(x, y) \in [-\Delta x/2, \Delta x/2] \times [-\Delta y/2, \Delta y/2]\}$ at the point of intersection without depositing all energy in the HDPE before surpassing the interface between the HDPE block and the first unit cell detector, $z = \Delta z$.

The probability that a normally incident neutron of kinetic energy E_n interacts with HDPE within dz about z is

$$f_1(z|E_n)dz = \mu(E_n)e^{-\mu(E_n)z} dz, \quad (2.39)$$

where $\mu(E_n)$ is the macroscopic cross section of HDPE for neutrons of energy E_n . $f_1(z|E_n)$ is

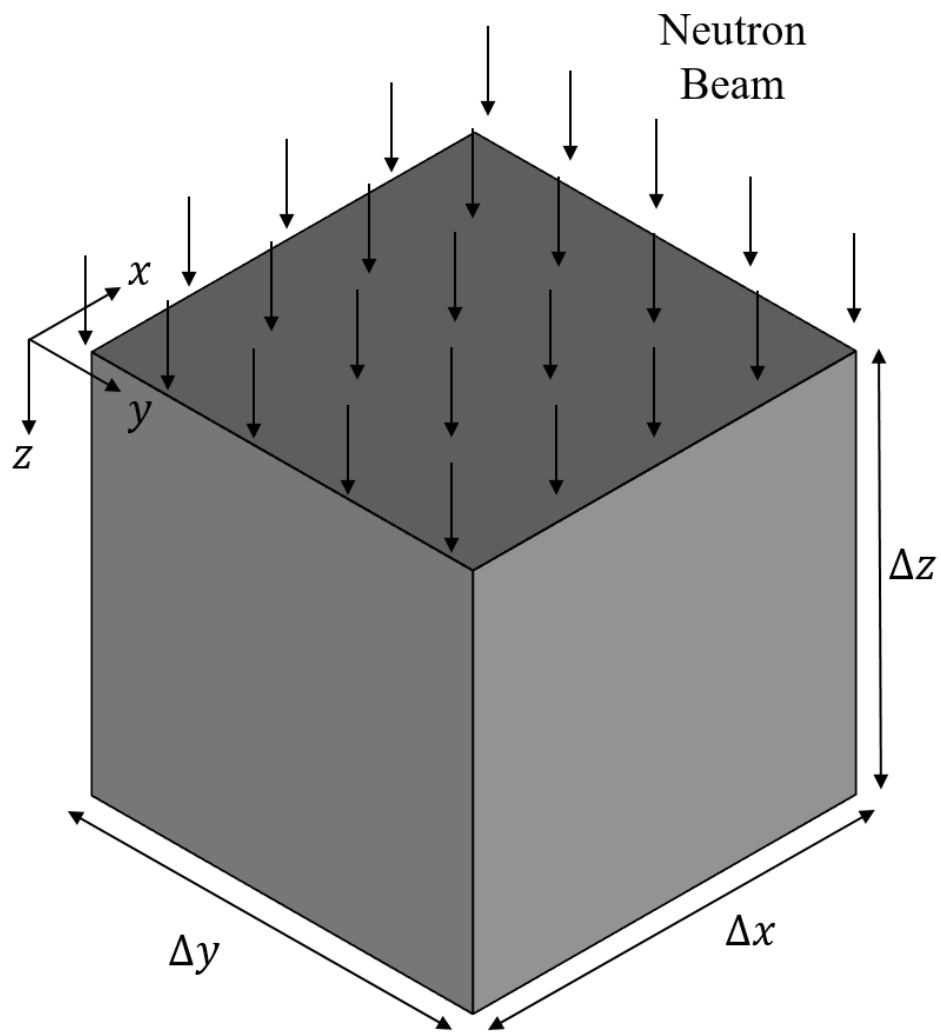


Figure 2.5: HDPE block with coordinate system and dimensions.

a probability density function (PDF). Integrating $f_1(z|E_n)$ over the interval $z \in (z_0 - \delta, z_0 + \delta)$, where $z_0 - \delta < z_0 + \delta \leq \Delta z$ and δ is some arbitrarily small distance, gives the probability of interaction within the interval,

$$P_1(z_0 - \delta \leq z \leq z_0 + \delta | E_n) = \int_{z_0 - \delta}^{z_0 + \delta} \mu(E_n) e^{-\mu(E_n)z} dz = 2e^{-\mu(E_n)z_0} \sinh(\mu(E_n)\delta). \quad (2.40)$$

Note that the total probability of a neutron interacting in the HDPE block of depth Δz can be determined by setting $z_0 - \delta = 0$ and $z_0 + \delta = \Delta z$,

$$P_1(0 \leq z \leq \Delta z | E_n) = 1 - e^{-\mu(E_n)\Delta z}, \quad (2.41)$$

which confirms that as Δz increases, so too does the probability of a neutron interaction occurring in the HDPE block.

The probability that a particular type of interaction q occurs in an HDPE medium due to an incident neutron of energy E_n is given by

$$P_2(q | E_n) = \frac{\mu_q(E_n)}{\mu(E_n)}, \quad (2.42)$$

where μ_q is the probability per unit path length of an interaction of type q occurring in HDPE. μ_q (and similarly, μ) is calculated via

$$\mu_q = \frac{\rho_{\text{HDPE}} N_a}{\mathcal{A}_{\text{HDPE}}} \left(f^{\text{C-12}} \sigma_{q,\text{C-12}} + 2f^{\text{H-1}} \sigma_{q,\text{H-1}} + 2f^{\text{H-2}} \sigma_{q,\text{H-2}} \right), \quad (2.43)$$

where ρ_{HDPE} is the density of HDPE (0.97 g cm^{-3}), N_a is Avogadro's number, $\mathcal{A}_{\text{PMFND}}$ is the atomic weight of HDPE, f^ν is the abundance of isotope ν (as shown in Table 2.2), and $\sigma_{q,\nu}$ is the microscopic neutron cross section of isotope ν for an interaction of type q .

Finally, the probability that an interaction of type q occurring at location (x, y, z) will yield a recoil ion that exits the back face of the HDPE is described by $P_3(\cdot) = P_3(z' \geq \Delta z \cap (x(t_0), y(t_0)) \Big|_{z(t_0)=\Delta z} \in \mathcal{D} | E_n, q)$. Let t_0 be the instant at which the recoil ion intersects

with the $z = \Delta z$ plane. The locus of final ion recoil positions (x', y', z') is given by

$$x' = \Lambda_{\text{HDPE}}(T) \sqrt{1 - \omega_r^2} \cos \psi_r + x_0, \quad (2.44)$$

$$y' = \Lambda_{\text{HDPE}}(T) \sqrt{1 - \omega_r^2} \sin \psi_r + y_0, \quad (2.45)$$

and

$$z' = \Lambda_{\text{HDPE}}(T) \omega_r + z_0. \quad (2.46)$$

In Equations 2.44-2.46, Λ_{HDPE} and T are the range in HDPE and kinetic energy of the recoil ion, respectively, and ω_r is the direction cosine of the recoil ion with respect to the positive z -axis. The recoil ion energy T is a function of ω_c (the direction cosine in the center-of-mass system, E_n , the reaction Q -value, and q ,

$$T = \frac{1}{2} E_n (1 - \alpha) (1 - \omega_c \sqrt{1 + \Delta}) + \frac{Q}{A + 1}, \quad (2.47)$$

where A is the ratio of the recoil ion to the incident neutron (essentially, the mass number of the recoil ion),

$$\alpha = \left[\frac{A - 1}{A + 1} \right]^2, \quad (2.48)$$

and

$$\Delta = \frac{Q(1 + A)}{A E_n}. \quad (2.49)$$

A value of $Q = 0$ indicates that an elastic scattering interaction occurred,⁴⁸ which is by far the most common interaction that occurs in the case under consideration; recoil ion energies are also at their greatest when produced via elastic scattering. The recoil ion direction cosine is given by

$$\omega_r = \sqrt{1 - \frac{1}{A} \frac{E_n - T + Q}{T} \frac{1 - \omega_c^2}{(\gamma + \omega_c)^2 + (1 - \omega_c^2)}}, \quad (2.50)$$

where

$$\gamma = \left[A^2 + \frac{A(A + 1)Q}{E_n} \right]^{-1/2}. \quad (2.51)$$

The expression for $P_3(\cdot)$ exists in closed form, but is cumbersome and unnecessary to express since it is computed easily via Monte Carlo simulation. A simple Monte Carlo simulation was built to estimate this quantity and the overall probability function $P(x, y, z|E_n, \Delta x, \Delta y, \Delta z)$. The overall probability function, which describes the probability of a neutron of kinetic energy E_n that is normally incident on the front face of the HDPE block of dimensions $\Delta x, \Delta y, \Delta z$ interacting in the HDPE at (x_0, y_0, z_0) , producing a recoil ion, and that recoil ion exiting the HDPE block through its back face, is given by

$$P(x_0, y_0, z_0|E_n, \Delta x, \Delta y, \Delta z) = \sum_q P_1(z_1 \leq z_0 \leq z_2|E_n)P_2(q|E_n)P_3(\cdot). \quad (2.52)$$

For a recoil ion to exit the back face of the HDPE block, the range of the recoil ion Λ must be great enough to reach $z = \Delta z$ and its direction of travel, defined by ω_r and ψ_r , must intersect with the plane $z = \Delta z$ within the domain \mathcal{D} . Parametric equations are generated from Equations 2.44-2.46 to determine the parameter t_0 for which $z(t_0) = \Delta z$,

$$x(t_0) = (x' - x_0)t_0 + x_0, \quad (2.53)$$

$$y(t_0) = (y' - y_0)t_0 + y_0, \quad (2.54)$$

$$z(t_0) = (z' - z_0)t_0 + z_0. \quad (2.55)$$

Solving Equation 2.55 for t_0 , and letting $z(t_0) = \Delta z$ gives

$$t_0 = \frac{\Delta z - z_0}{z' - z_0}. \quad (2.56)$$

If $0 \leq t_0 \leq 1$, then the recoil ion has enough kinetic energy to reach the $z = \Delta z$ plane. If $(x(t_0), y(t_0)) \in \mathcal{D}$, then the recoil ion exits the back face of the HDPE block and has the potential to deposit energy in one or more unit cell detectors. A simple Monte Carlo simulation code, `scattering.py` (given in Appendix C), was built to compute $P(x, y, z|E_n, \Delta x, \Delta y, \Delta z)$. This process is carried out in a series of steps.

1. The user selects the incident neutron kinetic energy E_n and the dimensions of the HDPE block, Δx , Δy , Δz .
2. The user specifies how the HDPE block should be spatially discretized and develops a list of (x, y, z) locations such that $x \in (-\Delta x/2, \Delta x/2)$, $y \in (-\Delta y/2, \Delta y/2)$, and $z \in (0, \Delta z)$.
3. The user selects the number of histories N to run for each (x, y, z) position.
4. The code is executed.
5. The list of interaction locations (x, y, z) are generated.
6. For each interaction location:
 - (a) $P_1(z_1 \leq z \leq z_2|E_n)$ is computed via Equation 2.40.
 - (b) For each interaction type q that produces a recoil ion:
 - i. The number of times a recoil ion exits through the back face of the HDPE block is initialized to $N_q = 0$.
 - ii. The recoil ion produced by the interaction of type q is determined. Let the ratio of the recoil ion rest mass to the incident neutron rest mass be A .
 - iii. $P_2(q|E_n)$ is computed via Equation 2.42.
 - iv. For each simulated recoil ion history (N_p total):
 - A. Randomly sample ω_c and ψ_r over the domains $[-1, 1]$ and $[0, 2\pi]$, respectively. This is valid because scattering is generally considered isotropic in the center-of-mass system for low-to-intermediate E_n , e.g., hydrogen scattering is considered isotropic in the center-of-mass system up to $E_n \sim 30$ MeV.⁴⁸
 - B. Use Equations 2.47-2.51 to compute T and ω_r .
 - C. Extract the range $\Lambda(T)$ from an HDPE range table for the relevant recoil ion and kinetic energy.

- D. Use Equations 2.44-2.46 to compute final positions (x', y', z') .
 - E. Compute t_0 via Equation 2.56. If $0 \leq t_0 \leq 1$ and $(x(t_0), y(t_0)) \in \mathcal{D}$, then the recoil ion exits the HDPE block through the back face and N_q should be incremented by one.
 - F. Compute $P_3(z' \geq \Delta z \cap (x(t_0), y(t_0)) \Big|_{z(t_0)=\Delta z} \in \mathcal{D} | E_n, q)$ as N_q/N .
- (c) Compute the total probability $P(x_0, y_0, z_0 | E_n, \Delta x, \Delta y, \Delta z)$ for this location using Equation 2.52.
7. Save the total probability $P(x_0, y_0, z_0 | E_n, \Delta x, \Delta y, \Delta z)$ for this interaction location (x_0, y_0, z_0) .

Figure 2.6 shows the cloud of sample points used to calculate $P(x, y, z | E_n, \Delta x, \Delta y, \Delta z)$ for a single interaction point (x_0, y_0, z_0) and the locations at which some of those points intersect with the back face of the HDPE block for a visual reference.

2.4.2 Optimizing the Unit Cell Detector Stack

Depending on the neutron radiation context in which the PMFND is used, its efficiency and effectiveness as a spectrometer may be improved by modifying the dimensions of either the HDPE conversion material or modifying the depth of the unit cell detectors (either individually or uniformly). This section discusses parameters pertaining to the unit cell detector stack that could be modified to optimize PMFND performance.

2.4.2.1 SRIM Runs for Unit Cell Detector Stack Optimization

A series of SRIM simulations were carried out to ensure that the current iteration of the PMFND is large enough to stop the highest energy recoil ions for the desired neutron energy range. The current iteration of the PMFND is ostensibly designed for incident neutron energies $E_n \in [0, 20]$ MeV with a 1 cm^3 HDPE conversion block, $I = 20$ unit cell detectors, and $40 \mu\text{m}$ thick Si detection regions. Consider the extreme case where a neutron of energy

- Recoil Proton Stopping Location
- HDPE Back Face Intersection Locations
- Interaction Location (x_0, y_0, z_0)

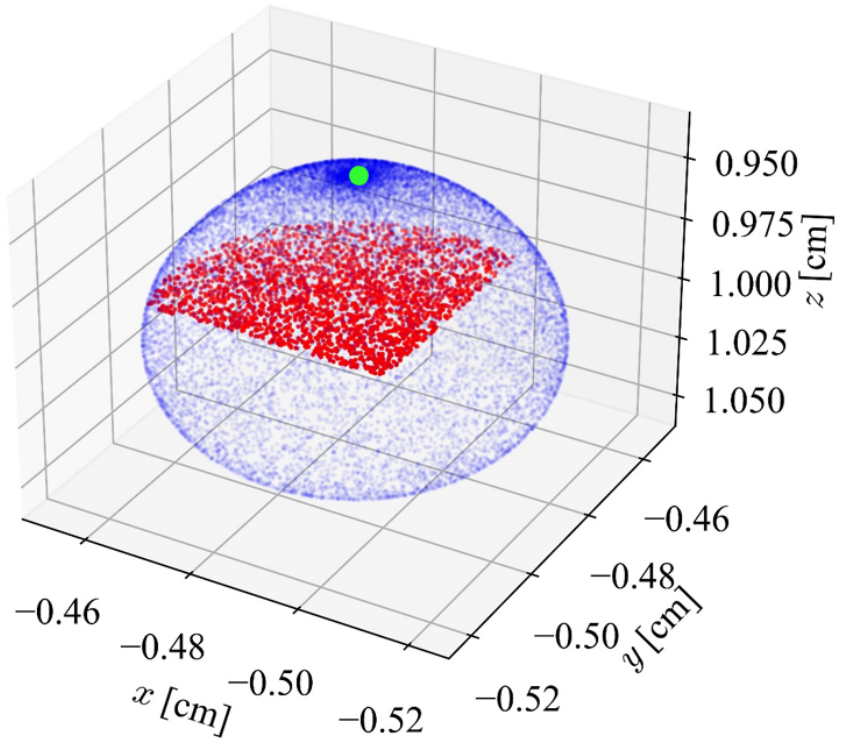


Figure 2.6: Balloon-like cloud of points representing locations at which recoil protons “range out” in HDPE as well as locations where protons intersect with the back face of the HDPE block.

E_n enters the HDPE layer, interacts at or very near $z = \Delta z$, and a recoil proton is forward-scattered with the same amount of energy as the incident neutron, $T = E_n$. The distance that this proton travels in the PMFND detector stack before stopping determines the number of unit cell detectors necessary to maximize spectroscopic information capture for neutron kinetic energies on the interval $(0, E_n)$.

Using *pysrim*, SRIM simulations were conducted to obtain stopping power curves as a function of PMFND depth for 20 recoil proton energies: the integer values between 1 MeV to 20 MeV. A 55 unit cell detector PMFND was assembled in *pysrim*. 100 recoil protons with initial energy T are emitted from the interface between the HDPE block and the first unit cell detector at $z = \Delta z$ along the $+z$ -axis. The average stopping power as a function of $z - \Delta z$ is recorded. The Kinchen-Pease calculation mode discussed in Section 2.1.2 is used. The *pysrim* script that executes this set of simulations is shown in Appendix B. The resulting stopping power curves are used to determine the stack depth necessary to capture the highest energy recoil ions.

The production of carbon recoil ions is an additional concern. The PMFND’s design is predicated on the idea that recoil protons are the main mode by which energy is deposited in the unit cell detector stack, and thus the main mode by which information about the incident neutron energy spectrum is accumulated. The energy of a recoil ion produced via elastic scattering is

$$T = E_n(1 - \alpha)\omega_r^2. \quad (2.57)$$

For protons, $\alpha = 0$, so the recoil proton energy is related to the incident neutron energy by the recoil scattering cosine alone. For $^{12}_6\text{C}$ ions, $\alpha = (11/13)^2 \approx 0.72$. The recoil ion energy is reduced by 72% without accounting for the angle of scatter. This “scrambling” of spectroscopic information could hinder the PMFND’s ability to unfold the incident neutron energy spectrum. Knowledge of the likelihood that carbon recoil ions deposit energy in one or more of the unit cell detectors would be useful for correcting oddities at the low end of the unfolded neutron energy spectrum. Carbon recoil ions are produced in the HDPE with a non-negligible probability, especially as incident neutron energy increases.

2.4.2.2 Carbon Ion Recoil Considerations

A second series of SRIM simulations were conducted to obtain recoil carbon ion stopping power curves as a function of PMFND depth for 20 recoil carbon energies from 0.2840 MeV to 5.680 MeV. 100 recoil carbon ions with initial energy T are emitted from the interface between the HDPE block and the first unit cell detector at $z = \Delta z$ along the $+z$ -axis. Only one unit cell detector was necessary for this set of simulations due to the protracted range of $^{12}_6\text{C}$ ions. The resulting stopping power curves are used to show where carbon ions range out in the PMFND.

Chapter 3

Results and Discussion

3.1 Unfolding the Neutron Energy Spectrum

3.1.1 PMFND Response Functions

Figure 3.1 shows the absorbed dose response functions $\mathcal{R}_i(E_n)$ for PMFND unit cell detectors $i = 1, \dots, 20$ generated from the procedure discussed in Section 2.2.1. The response functions are considered well-developed. Errors computed by PHITS for the point estimates that comprise the response functions are negligibly small and omitted from Figure 3.1.

Observing the interrelationships between response functions, a few phenomena are apparent. Note that the response functions are all *almost* monotonically non-decreasing functions (there is one common energy range within which the response functions do decrease slightly, and this will be addressed momentarily). Assuming this monotonic behavior continues for $E_n \geq 20$ MeV, increasing the incident neutron kinetic energy will yield a greater energy deposition. It appears that the detector response functions will eventually stop increasing for some $E_n > 20$ MeV that is different for each response function. A thresholding effect is also observed, as all response functions appear to follow a common curve, highlighted in Figure 3.2 before branching off into distinct response functions. This common response function curve is likely due to a combination of *direct* neutron interactions in silicon and interactions in metallization layers that result in fragmentation ions. The common oscillatory behavior

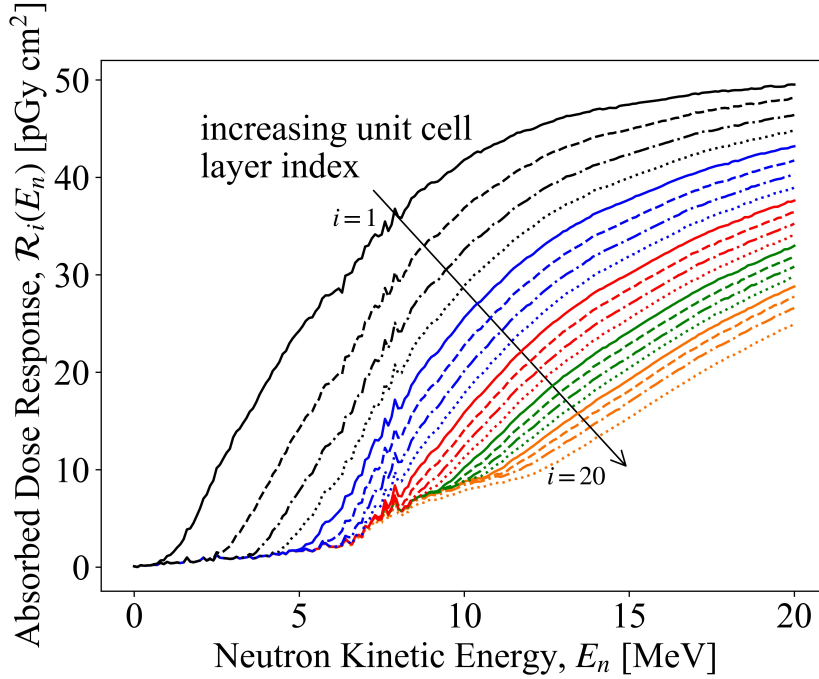


Figure 3.1: Absorbed dose response functions for unit cell detectors $i = 1, \dots, 20$.²¹

that appears around 7.5 MeV in all response functions is likely the result of a common ion fragmentation interaction. Response functions deviate from this common curve once the range of a recoil proton with energy $T = E_n$ in the PMFND surpasses the depth at which the front end of the active region of the associated silicon detection region is located.

Finally, note that the spacing between consecutive response functions decreases for deeper unit cell detectors. This phenomenon is directly related to the fact that the spread of the Bragg peak increases as initial recoil ion energy increases, as shown later on in Figures 3.27 and 3.28. As is discussed in Section 3.3.2, increasing the silicon thickness of unit cell detectors at greater depths may improve energy discrimination capabilities of the PMFND.

3.1.2 Unfolded Neutron Energy Spectra

This section presents and discusses the results of applying the NNLS and SPUNIT unfolding algorithms to each incident neutron spectrum unfolding algorithm.

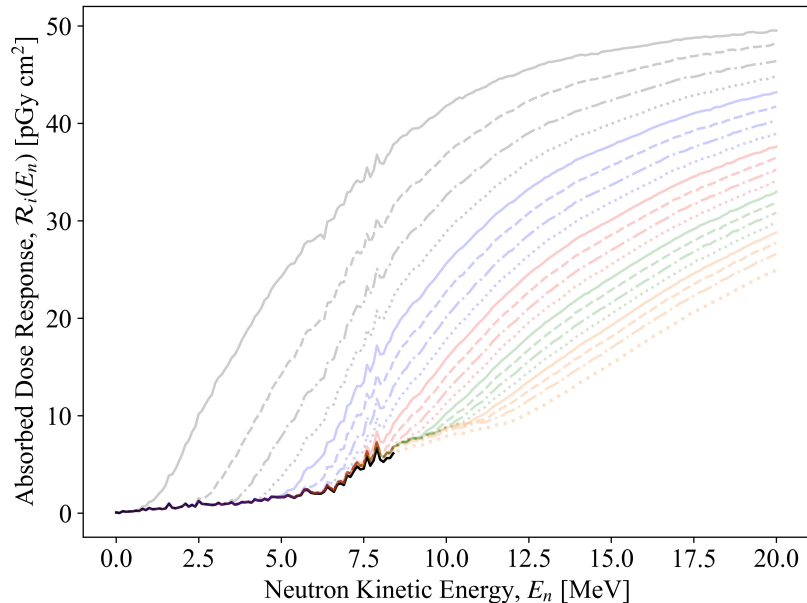


Figure 3.2: Curve from which all absorbed dose response functions appear to emanate.

3.1.2.1 Non-Negative Least Squares Method

Figures 3.3-3.5 show the unfolded ^{252}Cf , AmB, and AmBe neutron spectra obtained when applying the NNLS unfolding method to the first five layers of the PMFND. Let $I = 5$; only unit cell detectors $i = 1, \dots, 5$ are considered. Equations 2.17-2.19 are used to obtain $F(E_n)$. Let $M = 5$ to form the energy-averaged response matrix \mathcal{R}_{AV} . The absorbed dose values obtained, D_i , from the greatest incident integral neutron fluence value, $\Phi_0 = 2.1 \times 10^{10} \text{ cm}^{-2}$, were used for unfolding. \mathcal{R}_{AV} is obtained by letting $\Delta E_m = 4 \text{ MeV}$ for $m = 1, \dots, 5$. Surprisingly, unfolded spectra using only the first five layers of the PMFND show decent agreement with analogously energy-averaged incident neutron energy spectra $\chi_{AV}(E_n)$.

Figure 3.3 shows the unfolded ^{252}Cf neutron energy spectrum obtained from applying NNLS to the first five layers of the PMFND. The unfolded neutron energy spectrum agrees nearly perfectly with the energy-averaged (binned) incident neutron energy spectrum, $\chi_{AV}(E_n)$. The binned spectrum is quite coarse and lacks detail, but it is promising that the unfolded spectrum reconstructs the binned spectrum so accurately without *a priori* information.

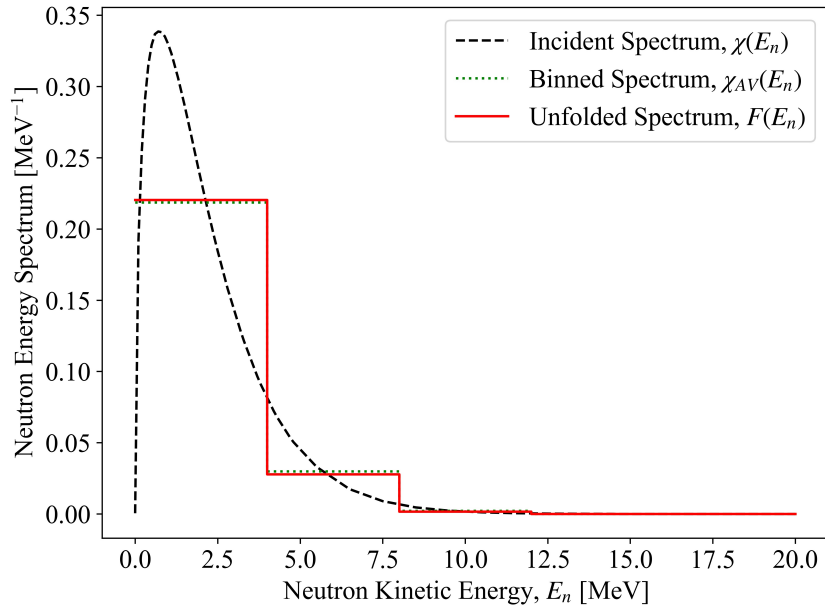


Figure 3.3: Unfolded ^{252}Cf neutron energy spectrum via NNLS method using first five unit cell detectors of PMFND and five linearly spaced energy bins.

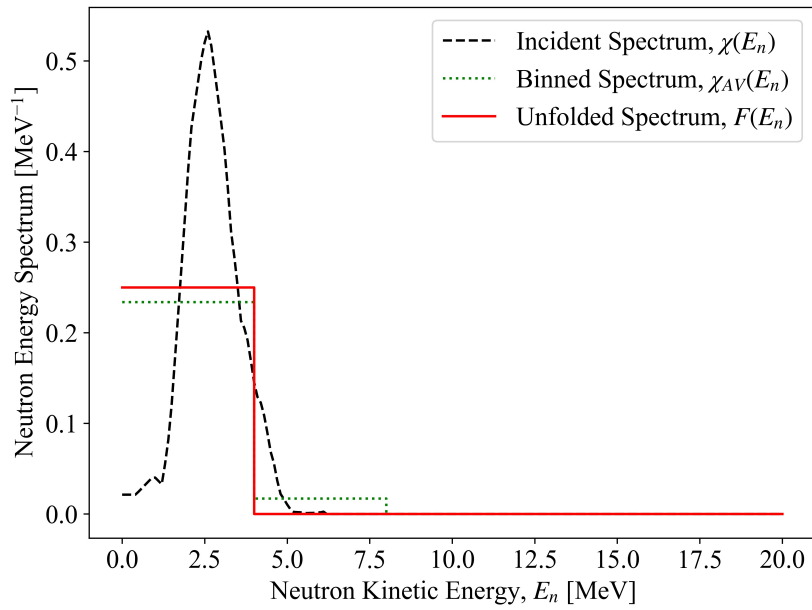


Figure 3.4: Unfolded AmB neutron energy spectrum via NNLS method using first five unit cell detectors of PMFND and five linearly spaced energy bins.

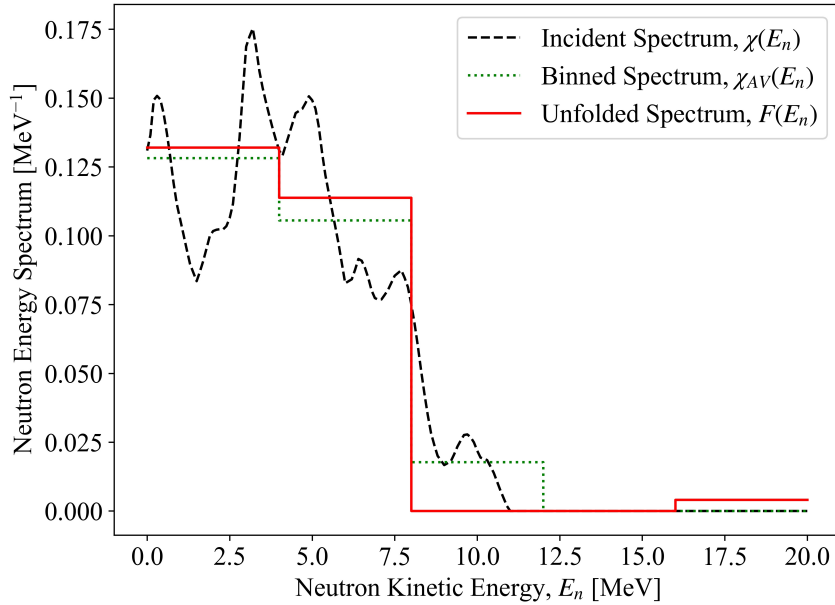


Figure 3.5: *Unfolded AmBe neutron energy spectrum via NNLS method using first five unit cell detectors of PMFND and five linearly spaced energy bins.*

Figure 3.4 shows the unfolded AmB neutron energy spectrum obtained from applying NNLS to the first five layers of the PMFND. Again, the unfolded neutron energy spectrum show good agreement with $\chi_{AV}(E_n)$, at least behaviorally.

Figure 3.5 shows the unfolded AmBe neutron energy spectrum obtained from applying NNLS to the first five layers of the PMFND. The unfolded energy spectrum follows the general shape of the AmBe spectrum, but generally does not agree well with the binned spectrum. The AmBe spectrum is too complex to replicate using such a coarse binning structure.

Figures 3.6-3.8 show the unfolded ^{252}Cf , AmB, and AmBe neutron spectra obtained when applying the NNLS unfolding method to all 20 layers of the PMFND. This time, let $I = 20$ and $M = 20$. Spectra unfolded with $I = 20$ and $M = 20$ show decent agreement with binned incident spectra. In each case, the general incident spectral trends are replicated by the unfolded neutron energy spectrum, but accuracy can vary wildly in individual energy bins.

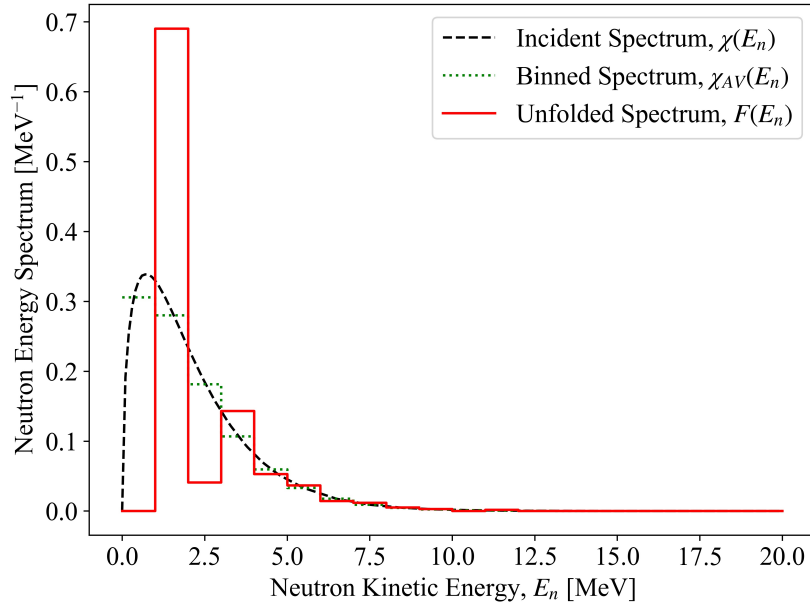


Figure 3.6: Unfolded ^{252}Cf neutron energy spectrum via NNLS method using 20 unit cell detectors of PMFND and 20 linearly spaced energy bins.

Figure 3.6 shows the unfolded ^{252}Cf neutron energy spectrum obtained from applying NNLS to a 20-layer PMFND. The unfolded energy spectrum follows the shape of the incident spectrum for energies $E_n \geq 3$ MeV. For $E_n < 3$ MeV, the unfolded spectrum overestimates and underestimates the incident spectrum significantly.

Figure 3.7 shows the unfolded AmB neutron energy spectrum obtained from applying NNLS to a 20-layer PMFND. The unfolded energy spectrum reproduces the shape of the incident spectrum in general, with small differences between the binned and unfolded spectra.

Figure 3.8 shows the unfolded AmBe neutron energy spectrum obtained from applying NNLS to a 20-layer PMFND. The unfolded energy spectrum follows the shape of the incident spectrum well for $E_n \geq 4$ MeV but again suffers inaccuracies at the low-energy end.

Overall, the five- and 20-layer PMFND NNLS unfolding methods are able to effectively reconstruct a variety of incident neutron energy spectra with coarse energy resolution. The NNLS unfolding algorithm has some difficulty reconstructing the low-energy end of some

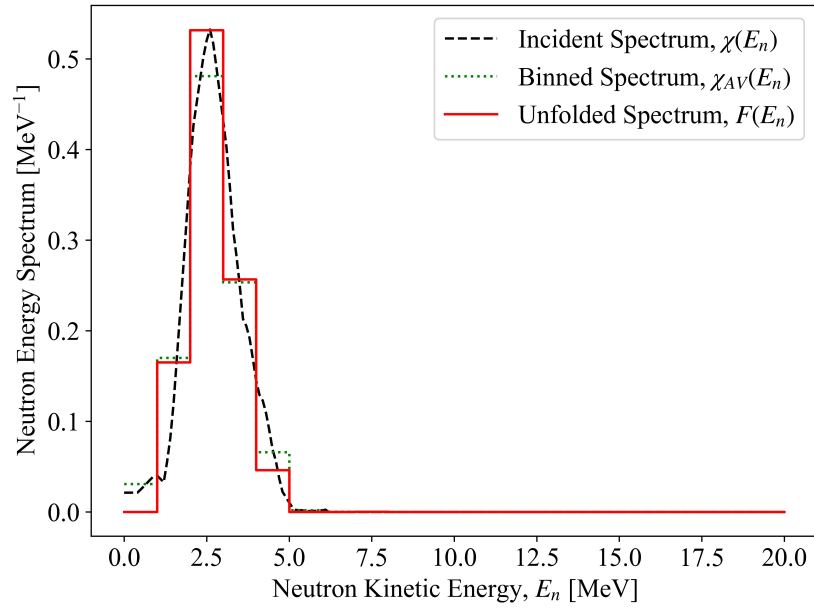


Figure 3.7: Unfolded AmB neutron energy spectrum via NNLS method using 20 unit cell detectors of PMFND and 20 linearly spaced energy bins.

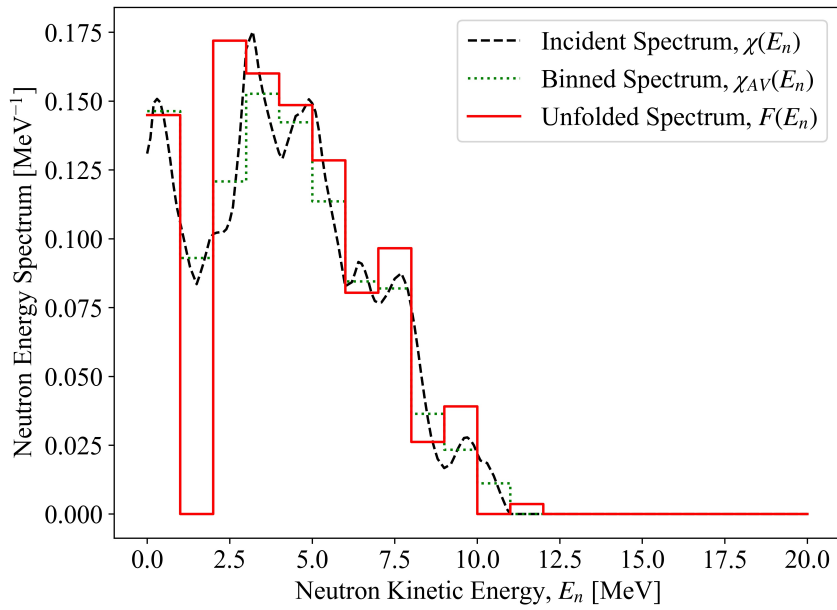


Figure 3.8: Unfolded AmBe neutron energy spectrum via NNLS method using 20 unit cell detectors of PMFND and 20 linearly spaced energy bins.

incident neutron energy spectra. This difficulty may stem from a fundamental issue with the construction of the energy-averaged response matrix, \mathcal{R}_{AV} . Equation 2.18 shows how each row of \mathcal{R}_{AV} is computed. Consider the m -th partial absorbed dose of the i -th unit cell detector—or the component of the absorbed dose associated with unit cell i due to incident neutrons with energies $E_n \in [E_m, E_{m+1})$ —computed via

$$\Delta_m D_i = \int_{E_m}^{E_{m+1}} \mathcal{R}_i(E_n) \Phi(E_n) dE_n. \quad (3.1)$$

Also, note that

$$D_i = \sum_{m=0}^M \mathcal{R}_{AV,i}(E_m) \Phi(E_m) \Delta E_m = \sum_{m=0}^M \Delta_m D_i \implies \mathcal{R}_{AV,i}(E_m) \Phi(E_m) \Delta E_m = \Delta_m D_i. \quad (3.2)$$

Replace $\Delta_m D_i$ with $\mathcal{R}_{AV,i}(E_m) \Phi(E_m) \Delta E_m$ in Equation 3.1 and solve for $\mathcal{R}_{AV,i}(E_m)$ to obtain

$$\mathcal{R}_{AV,i}(E_m) = \frac{1}{\Phi(E_m) \Delta E_m} \int_{E_m}^{E_{m+1}} \mathcal{R}_i(E_n) \Phi(E_n) dE_n \approx \sum_{j \ni E_m \leq E_j < E_{m+1}}^M \frac{\mathcal{R}_i(E_j) \Phi(E_j) \Delta E_j}{\Phi(E_m) \Delta E_m}. \quad (3.3)$$

Equation 3.3 shows that the elements of the energy-averaged response matrix depend on the incident energy-dependent fluence, which is the unknown of interest in the NNLS algorithm. Equation 2.18 constructs \mathcal{R}_{AV} under the assumption that the fluence spectrum is flat in each energy bin, or $\Phi(E_m) = \Phi(E_n)$ over the energy range $E_n \in [E_m, E_{m+1})$, which is unlikely for realistic neutron energy spectra. This assumption contributes to significant differences between the spectrum unfolded via NNLS and the incident neutron energy spectrum. This is especially important for rapidly varying incident spectra, like the low-energy regions of the ^{252}Cf and AmBe spectra.

3.1.2.2 SPUNIT Method

Figures 3.9-3.11 show the unfolded neutron energy spectra obtained from applying the SPUNIT algorithm using $N_{\text{it}} = 2 \times 10^5$ iterations to the $I = 20$ -unit cell detector PMFND. 2×10^5 SPUNIT iterations were conducted to balance computational time and unfolded

spectrum smoothness, as the smoothness of the unfolded neutron energy spectrum generally improves with diminishing returns as the number of iterations increases. The greatest integral neutron fluence $\Phi_0 = 2.1 \times 10^{10} \text{ cm}^{-2}$ was used to obtain the absorbed dose values D_i . Equations 2.20-2.23 are used to obtain $F(E_n)$. All SPUNIT unfolded spectra exhibit some noise. The unfolded ^{252}Cf and AmB spectra of Figures 3.9 and 3.10 qualitatively agree with their respective incident neutron energy spectra. The unfolded AmBe spectrum of Figure 3.11 is marginally acceptable. The general shape of the AmBe spectrum is preserved in the reconstruction, though some important details are absent or mislocated. The low-energy AmBe peak is missing in the unfolded spectrum. The highest-energy peak is shifted down by approximately 1 MeV. Some intermediate peaks, while properly located, are poorly resolved. One might expect that unfolding the AmBe neutron energy spectrum would be more difficult than ^{252}Cf and AmB due to its comparative complexity, as ^{252}Cf and AmB each only have one strong peak while AmBe has several. Still, spectrum reconstruction is expected to improve by increasing integral neutron fluence because the slope of the radiometric spectrometer effectiveness curve in Figure 3.15 is positive for the greatest integral neutron fluence tested. From the analysis of proton stopping power profiles in the PMFND discussed in Section 3.3.2, it is also clear that increasing the number of unit cell detectors would likely shift the high-energy AmBe to its correct location because forward-directed recoil protons of energies higher than 11 MeV are unable to deposit all energy within a 20 unit cell detector PMFND. The AmBe spectrum is non-zero for some $E_n > 11 \text{ MeV}$, so some spectroscopic information is lost when simulating the current PMFND iteration.

Figures 3.12-3.14 show the unfolded neutron energy spectra obtained from applying the same SPUNIT unfolding algorithm to the $I = 5$ -unit cell detector PMFND. It is immediately clear that the unfolded spectra obtained from the 5-unit cell PMFND do not agree nearly as well with their respective incident neutron energy spectra. It is notable that the unfolded ^{252}Cf spectrum is close to zero for energies $E_n \in (0, 1) \text{ MeV}$. The general shape of the unfolded AmB spectrum is reconstructed with significant noise. The unfolded AmBe spectrum fails to reproduce several peaks and flatlines above 7.5 MeV.

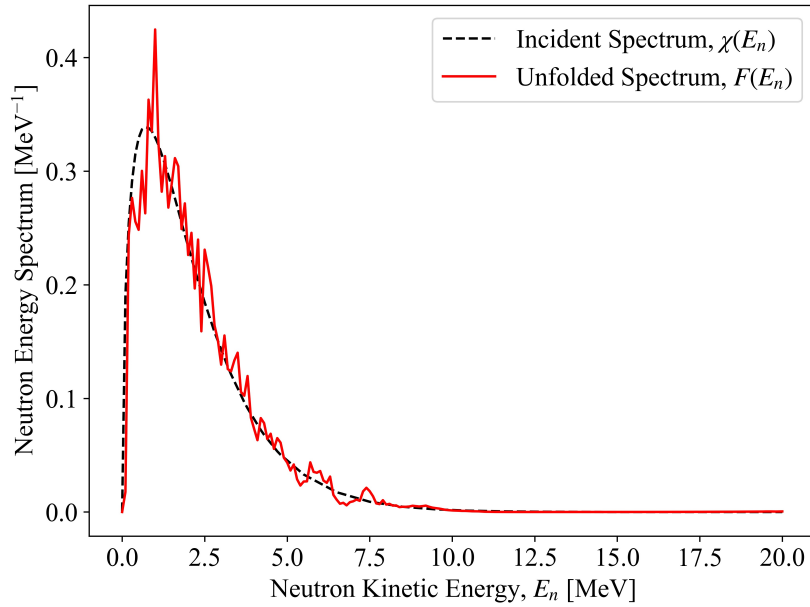


Figure 3.9: Unfolded ^{252}Cf neutron energy spectrum via SPUNIT method using 20 unit cell detectors, the highest integral neutron fluence simulated ($\Phi_0 = 2.1 \times 10^{10} \text{ cm}^{-2}$) and $N_{it} = 2 \times 10^5$ SPUNIT iterations.²¹

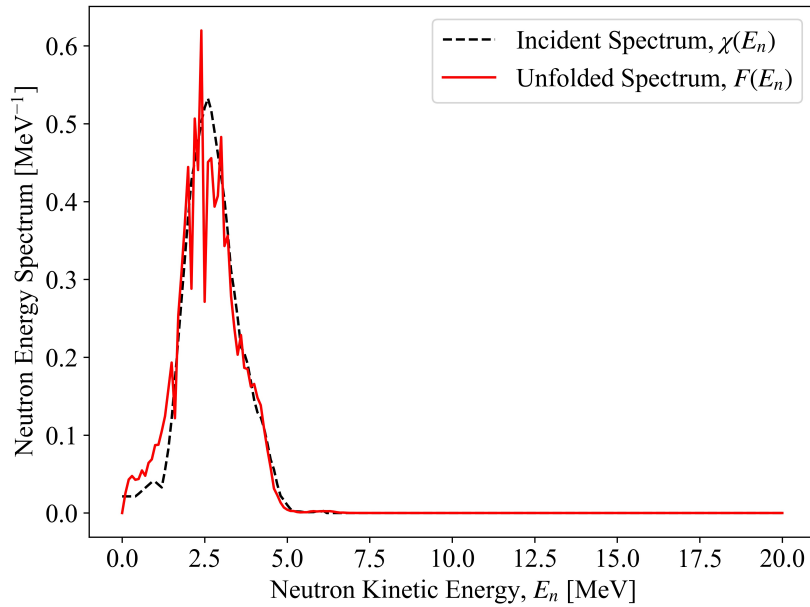


Figure 3.10: Unfolded AmB neutron energy spectrum via SPUNIT method using 20 unit cell detectors, the highest integral neutron fluence simulated ($\Phi_0 = 2.1 \times 10^{10} \text{ cm}^{-2}$) and $N_{it} = 2 \times 10^5$ SPUNIT iterations.²¹

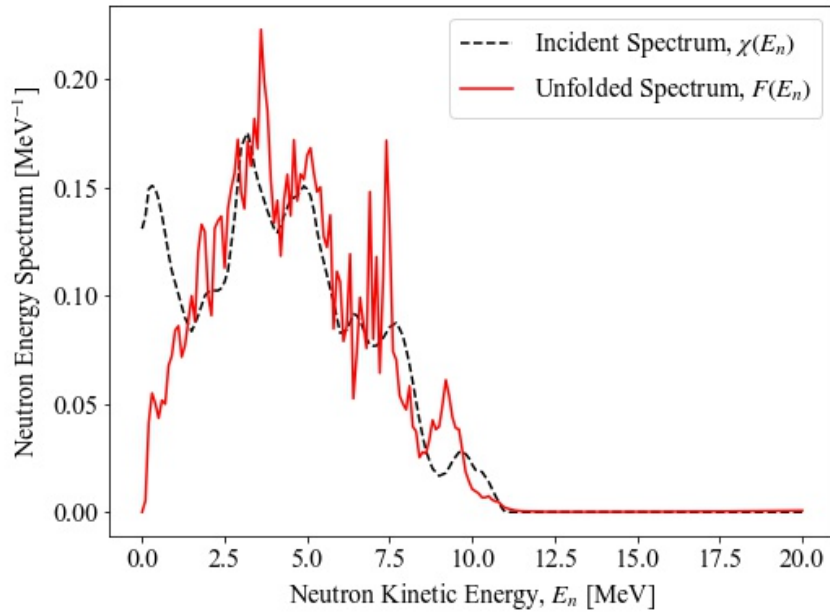


Figure 3.11: Unfolded AmBe neutron energy spectrum via SPUNIT method using 20 unit cell detectors, the highest integral neutron fluence simulated ($\Phi_0 = 2.1 \times 10^{10} \text{ cm}^{-2}$) and $N_{it} = 2 \times 10^5$ SPUNIT iterations.²¹

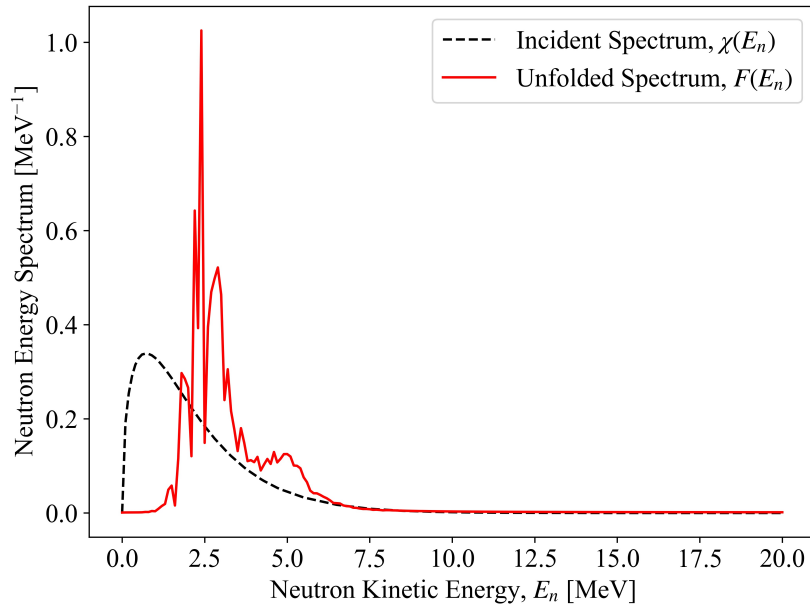


Figure 3.12: Unfolded ^{252}Cf neutron energy spectrum via SPUNIT method using 5 unit cell detectors, the highest integral neutron fluence simulated ($\Phi_0 = 2.1 \times 10^{10} \text{ cm}^{-2}$) and $N_{it} = 2 \times 10^5$ SPUNIT iterations.

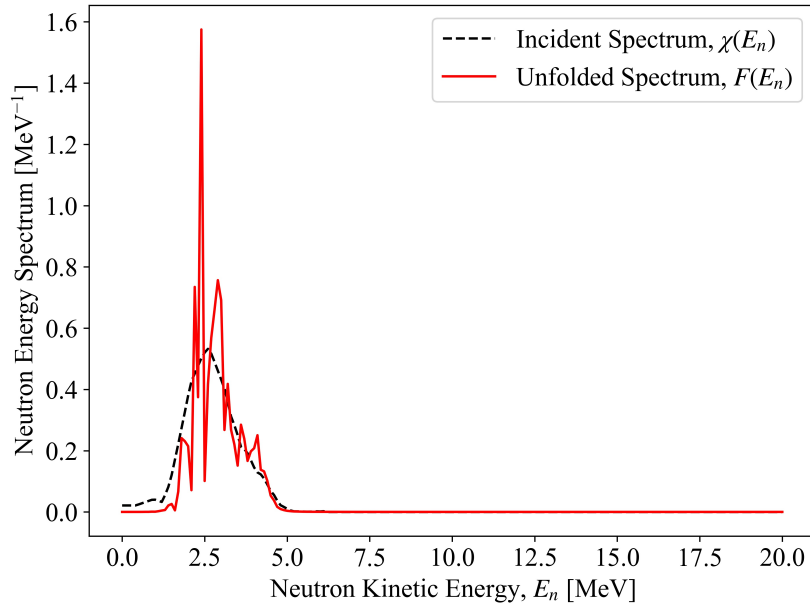


Figure 3.13: Unfolded AmB neutron energy spectrum via SPUNIT method using 5 unit cell detectors, the highest integral neutron fluence simulated ($\Phi_0 = 2.1 \times 10^{10} \text{ cm}^{-2}$) and $N_{it} = 2 \times 10^5$ SPUNIT iterations.

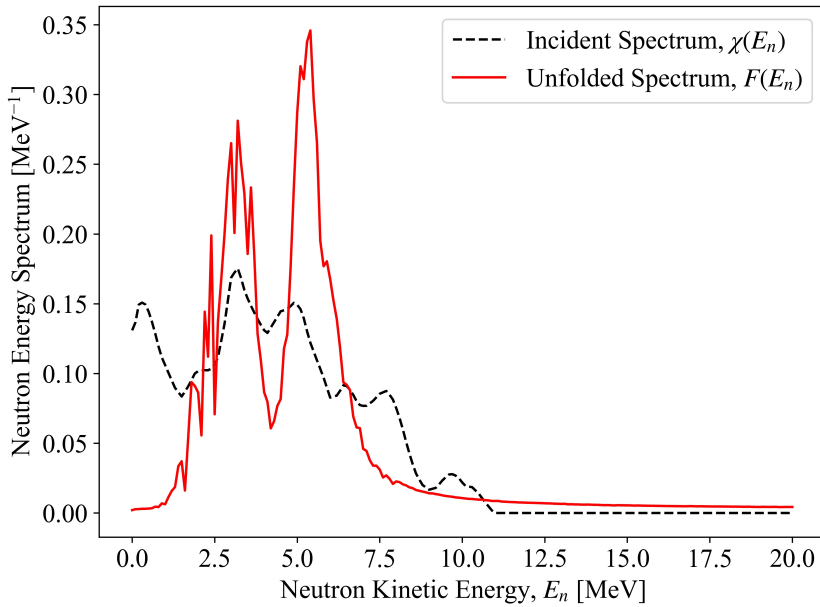


Figure 3.14: Unfolded AmBe neutron energy spectrum via SPUNIT method using 5 unit cell detectors, the highest integral neutron fluence simulated ($\Phi_0 = 2.1 \times 10^{10} \text{ cm}^{-2}$) and $N_{it} = 2 \times 10^5$ SPUNIT iterations.

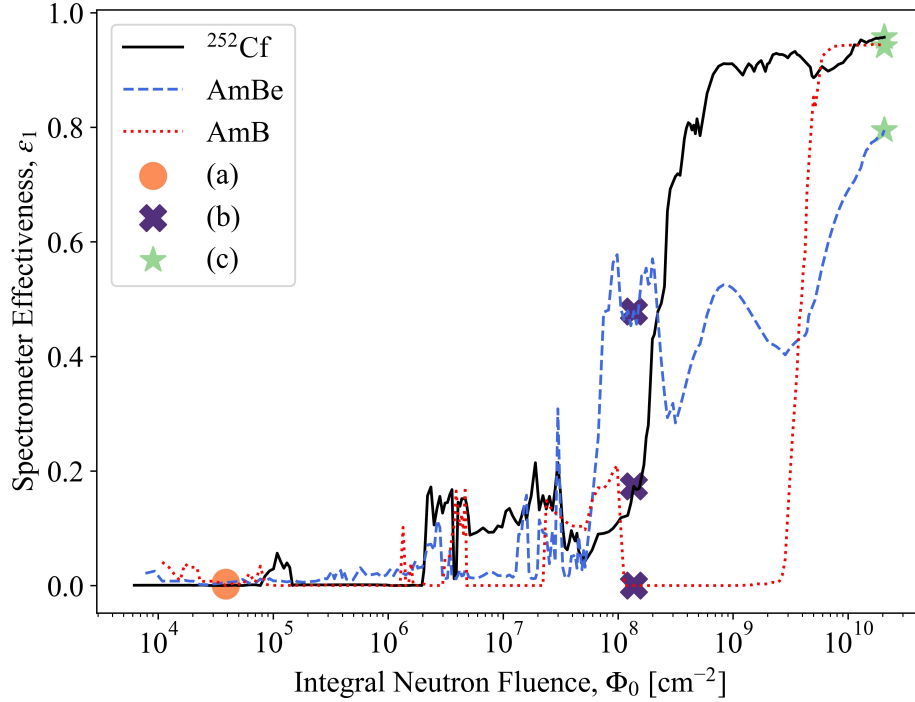


Figure 3.15: Radiometric spectrometer effectiveness as a function of integral neutron fluence for each neutron energy spectrum; marked locations (a), (b), and (c) on the effectiveness curve for each spectrum correspond to the unfolded neutron energy spectra labeled (a), (b), and (c) in Figures 3.16-3.18.²¹

3.2 Characterizing Spectrometer Effectiveness

This section discusses how the three spectrometer effectiveness measures (radiometric, dosimetric, and biometric) change as a function of integral neutron fluence for a 20-layer PMFND.

3.2.1 Radiometric Spectrometer Effectiveness

The radiometric spectrometer effectiveness for each tested spectrum as a function of integral neutron fluence is shown in Figure 3.15. As the integral neutron fluence increases, the radiometric spectrometer effectiveness generally tends toward unity for each tested spectrum. For low integral neutron fluence values, there is an abundance of noise due to the statistical variations associated with the Monte Carlo simulation results (energy deposition) and this noise is compounded during SPUNIT unfolding.

The radiometric spectrometer effectiveness tends to approach unity as integral neutron

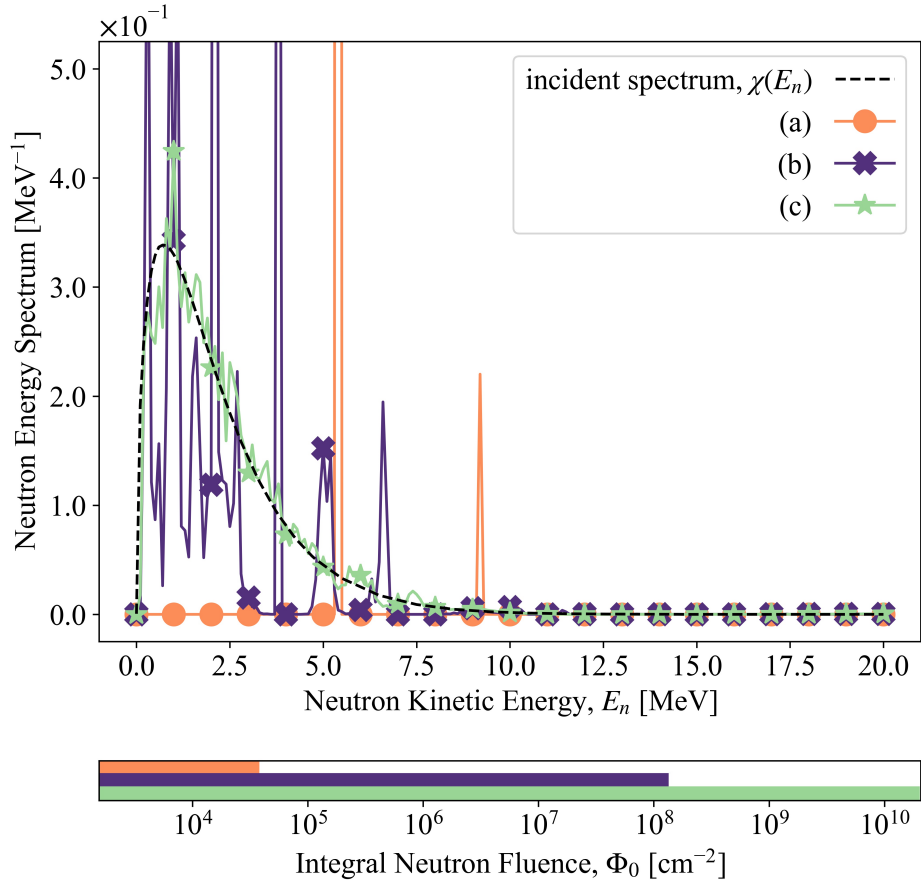


Figure 3.16: Illustration of unfolded ^{252}Cf spectra converging toward the incident neutron energy spectrum as the integral neutron fluence increases; unfolded spectrum (a) is obtained at a fluence of $3.6 \times 10^4 \text{ cm}^{-2}$ with radiometric spectrometer effectiveness $\varepsilon_1 = 1.37 \times 10^{-4}$ (b) at $3.8 \times 10^8 \text{ cm}^{-2}$ with radiometric spectrometer effectiveness $\varepsilon_1 = 0.173$, and (c) at $2.1 \times 10^{10} \text{ cm}^{-2}$ with radiometric spectrometer effectiveness $\varepsilon_1 = 0.957$.²¹

fluence increases for each tested spectrum. This implies that the unfolded neutron energy spectra tend to approach the incident neutron energy spectra as the integral neutron fluence increases. Figures 3.16-3.18 each display three unfolded spectra obtained from different integral neutron fluence values. In each case, the unfolded spectra more closely resemble the incident spectra as Φ_0 increases. Interested readers are encouraged to refer to the online version of *Planar Miniaturized Fast Neutron Spectroscopy Evaluation* by Stegeman *et al.* to view animated evolutions of the unfolded neutron energy spectra gradually converging to their associated incident neutron energy spectra as integral neutron fluence increases.²¹

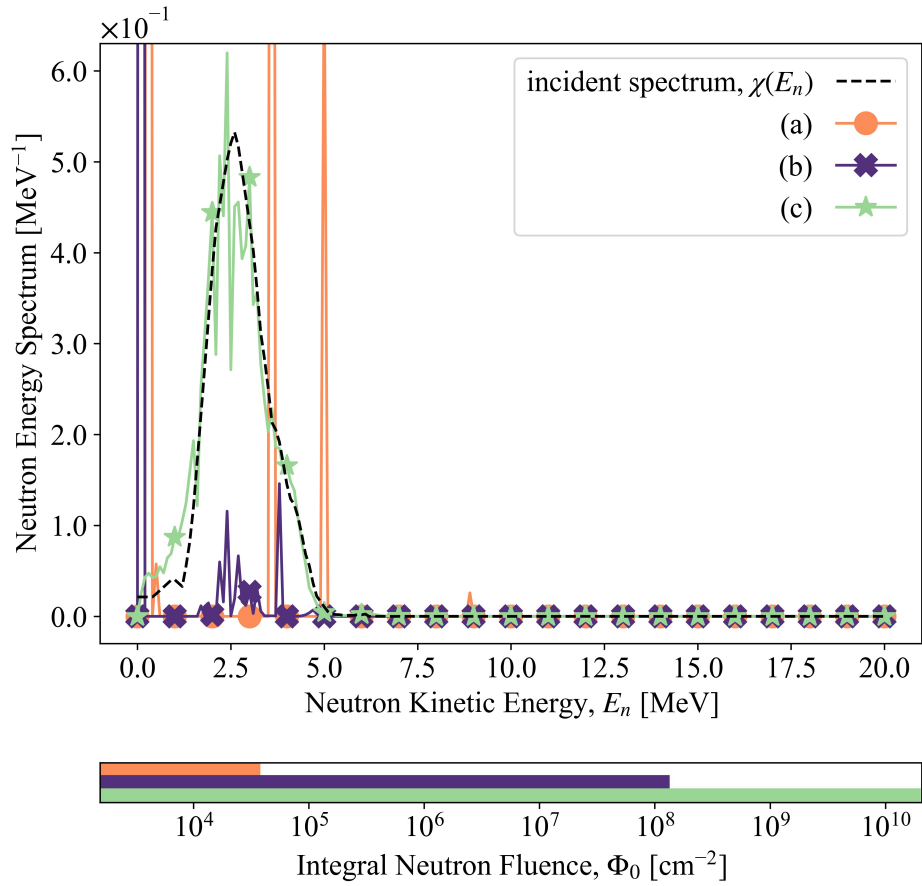


Figure 3.17: Illustration of unfolded AmB spectra converging toward the incident neutron energy spectrum as the integral neutron fluence increases; unfolded spectrum (a) is obtained at a fluence of $3.6 \times 10^4 \text{ cm}^{-2}$ with radiometric spectrometer effectiveness $\varepsilon_1 = 4.17 \times 10^{-4}$ (b) at $3.8 \times 10^8 \text{ cm}^{-2}$ with radiometric spectrometer effectiveness $\varepsilon_1 = 2.59 \times 10^{-5}$, and (c) at $2.1 \times 10^{10} \text{ cm}^{-2}$ with radiometric spectrometer effectiveness $\varepsilon_1 = 0.941$.²¹

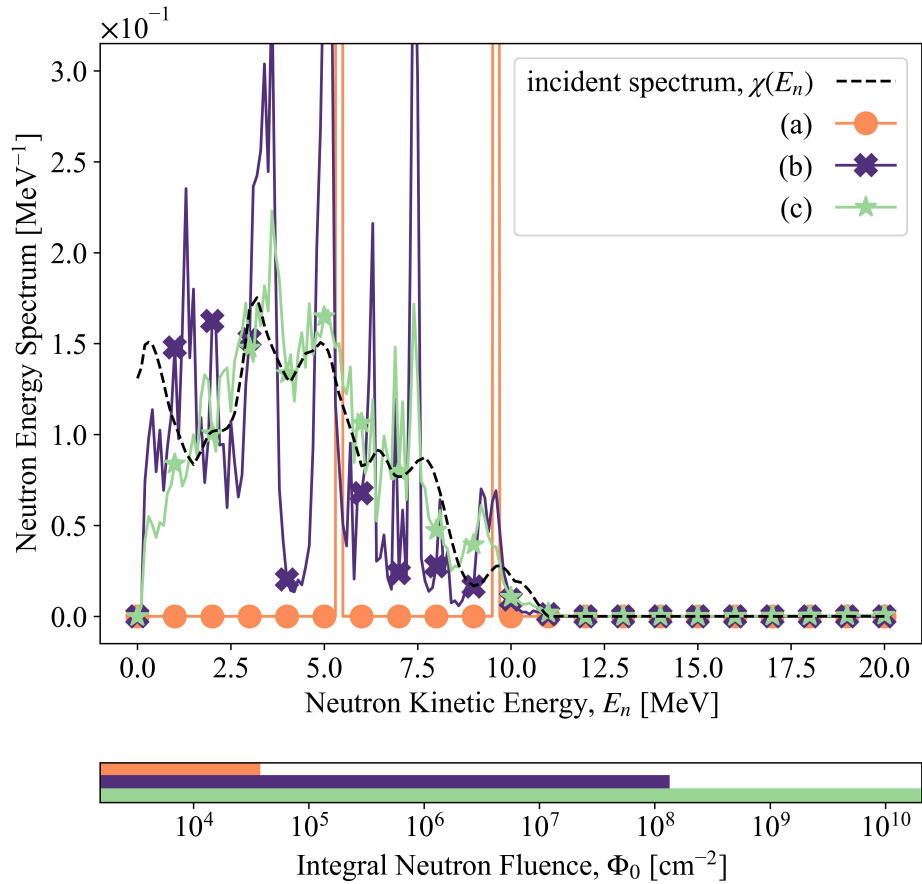


Figure 3.18: Illustration of unfolded AmBe spectra converging toward the incident neutron energy spectrum as the integral neutron fluence increases; unfolded spectrum (a) is obtained at a fluence of $3.6 \times 10^4 \text{ cm}^{-2}$ with radiometric spectrometer effectiveness $\varepsilon_1 = 5.24 \times 10^{-3}$ (b) at $3.8 \times 10^8 \text{ cm}^{-2}$ with radiometric spectrometer effectiveness $\varepsilon_1 = 0.478$, and (c) at $2.1 \times 10^{10} \text{ cm}^{-2}$ with radiometric spectrometer effectiveness $\varepsilon_1 = 0.795$.²¹

3.2.2 Dosimetric Spectrometer Effectiveness

The dosimetric spectrometer effectiveness for each tested spectrum as a function of integral neutron fluence is shown in Figure 3.19. Figure 3.19 shows that the dosimetric spectrometer effectiveness of all three spectra converge to unity as the integral neutron fluence increases. This indicates that the unfolded neutron energy spectrum is suited to estimate the absorbed dose in each unit cell detector by “refolding” response functions with the unfolded neutron energy spectrum via Equation 2.32. Figure 3.19 also shows that ε_2 is more susceptible to noise than ε_1 , owing to the fact that an additional integration is required to compute D_i^r , compounding the error that exists in $F(E_n)$.

Figures 3.20-3.22 depict the refolded absorbed dose values D_i^r of each spectrum approaching the expected absorbed dose values D_i computed via Equation 2.30 as the integral neutron fluence increases. D_i^r values appear to approach expected dose values D_i at a slower rate than simulated dose values D_i^s . This is likely because simulated dose values are only subject to the statistical uncertainties associated with PHITS simulations, and not the compounding of uncertainty that occurs during SPUNIT algorithm iteration and subsequent integration. Interested readers are encouraged to refer to the online version of *Planar Miniaturized Fast Neutron Spectroscopy Evaluation* by Stegeman *et al.* to view animated evolutions of refolded dose values gradually converging to the expected dose values as integral neutron fluence increases.²¹

3.2.3 Biohazard Spectrometer Effectiveness

Figure 3.23 shows the biometric spectrometer effectiveness for each incident neutron energy spectrum as a function of integral neutron fluence. The biometric spectrometer effectiveness converges toward unity as the integral neutron fluence increases, indicating that the PMFND is capable of accurately estimating the ambient dose equivalent $H^*(10\text{ mm})$ using the unfolded neutron energy spectrum given a large enough integral neutron fluence.

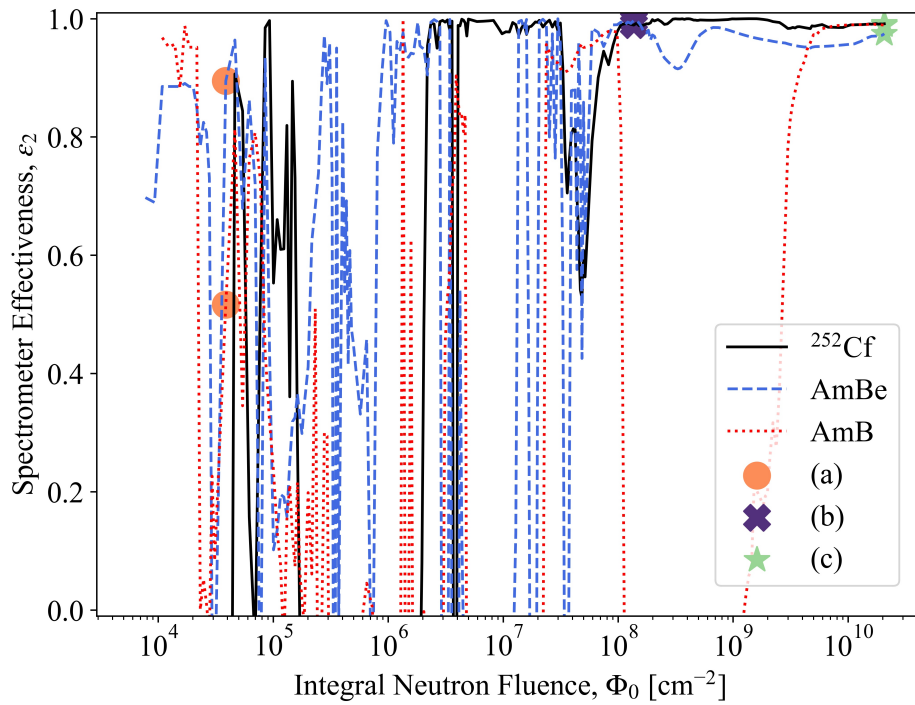


Figure 3.19: *Dosimetric spectrometer effectiveness as a function of integral neutron fluence for all tested incident neutron energy spectra; marked locations (a), (b), and (c) on the effectiveness curve for each spectrum correspond to the refolded dose values labeled (a), (b), and (c) in Figures 3.20-3.22.²¹*

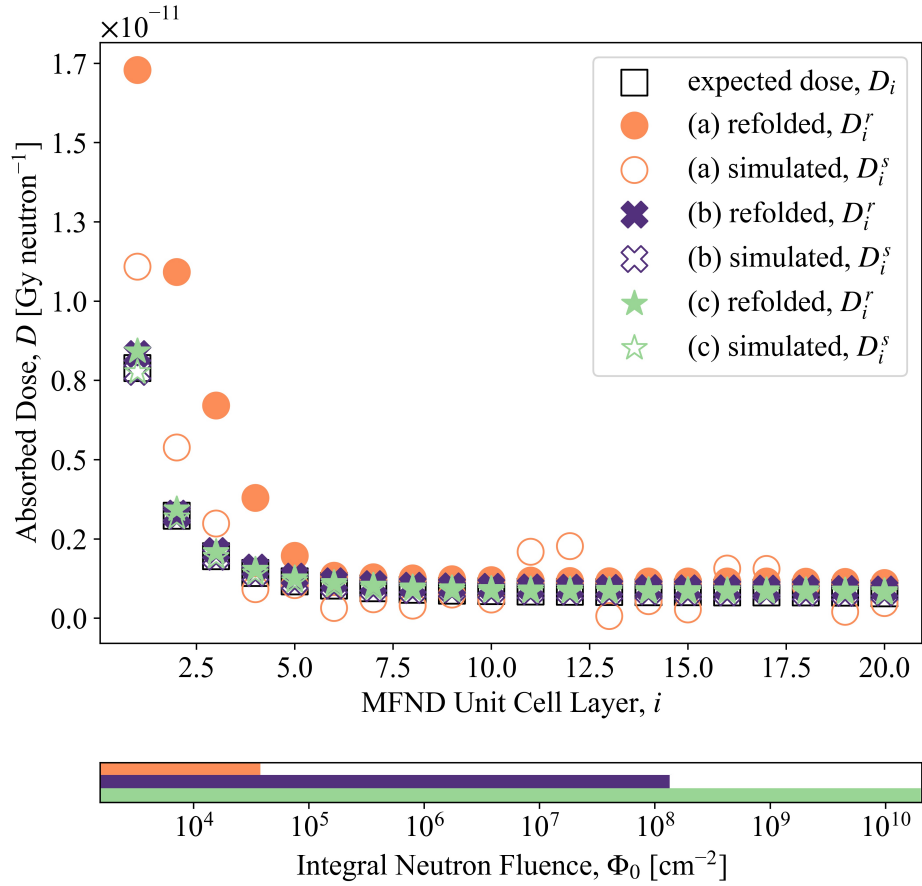


Figure 3.20: Illustration of refolded absorbed dose values (per source neutron) due to incident ^{252}Cf spectrum converging toward the expected absorbed dose values as the integral neutron fluence increases; refolded dose values (a) are obtained at a fluence of $3.6 \times 10^4 \text{ cm}^{-2}$ with dosimetric spectrometer effectiveness $\varepsilon_2 = -2.54$ (b) at $3.8 \times 10^8 \text{ cm}^{-2}$ with dosimetric spectrometer effectiveness $\varepsilon_2 = 0.989$, and (c) at $2.1 \times 10^{10} \text{ cm}^{-2}$ with dosimetric spectrometer effectiveness $\varepsilon_2 = 0.991$.²¹

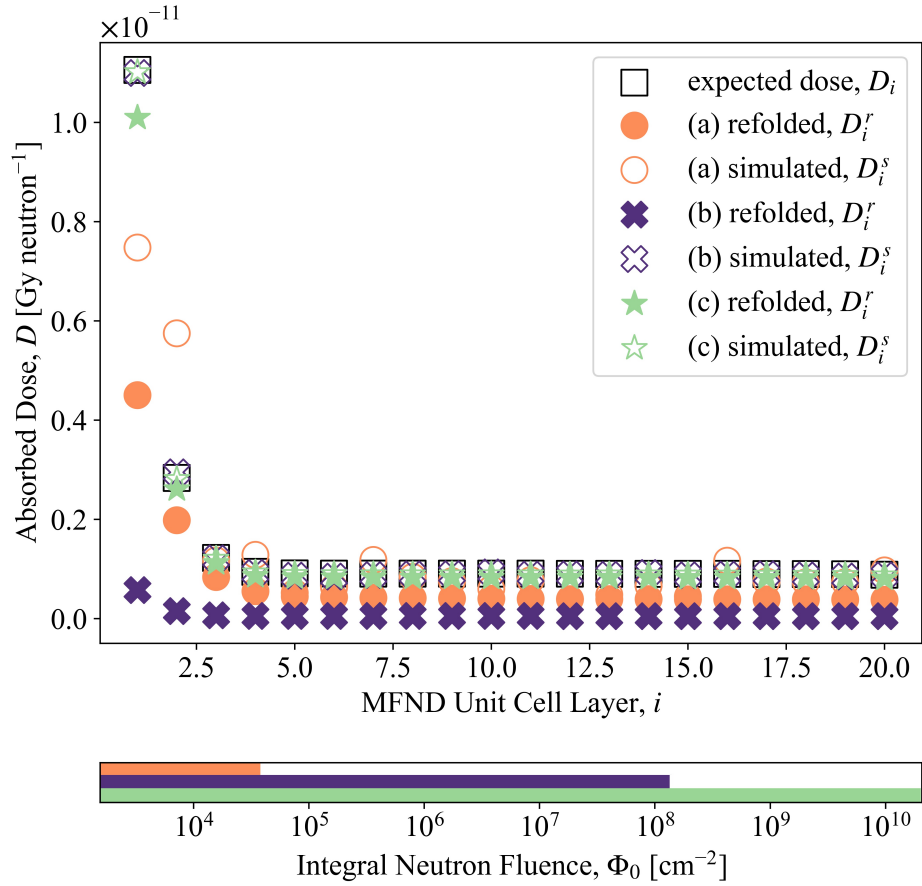


Figure 3.21: Illustration of refolded absorbed dose values (per source neutron) due to incident AmB spectrum converging toward the expected absorbed dose values as the integral neutron fluence increases; refolded dose values (a) are obtained at a fluence of $3.6 \times 10^4 \text{ cm}^{-2}$ with dosimetric spectrometer effectiveness $\varepsilon_2 = 0.516$ (b) at $3.8 \times 10^8 \text{ cm}^{-2}$ with dosimetric spectrometer effectiveness $\varepsilon_2 = -0.317$, and (c) at $2.1 \times 10^{10} \text{ cm}^{-2}$ with dosimetric spectrometer effectiveness $\varepsilon_2 = 0.989$.²¹

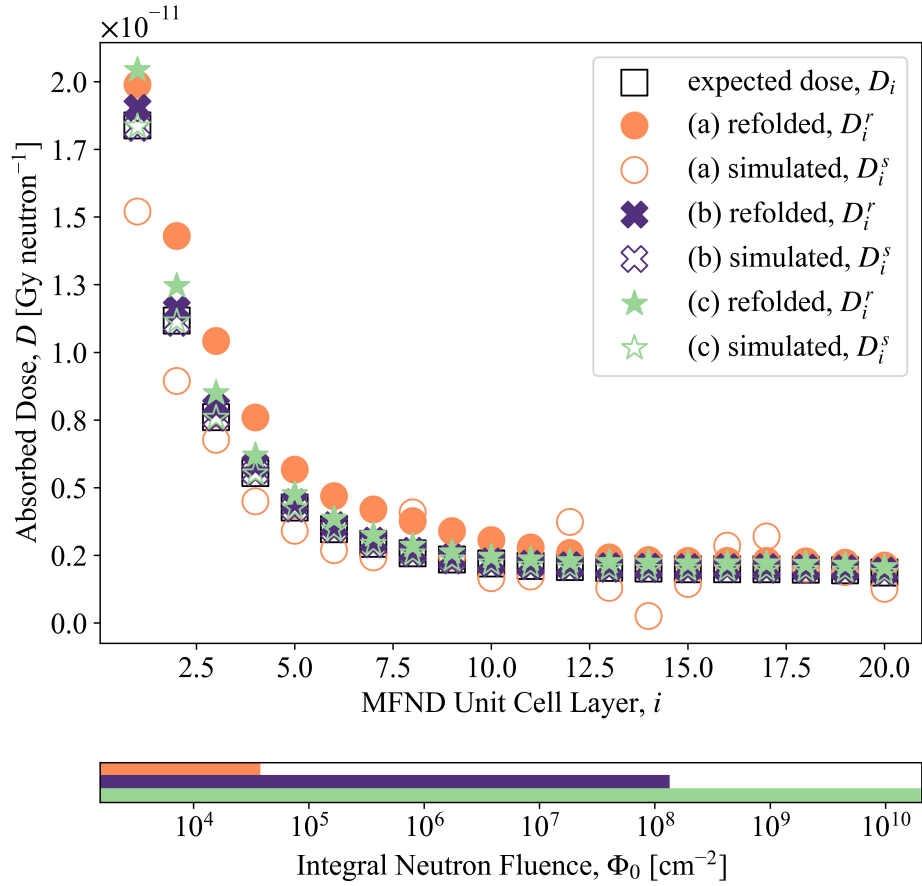


Figure 3.22: Illustration of refolded absorbed dose values (per source neutron) due to incident AmBe spectrum converging toward the expected absorbed dose values as the integral neutron fluence increases; refolded dose values (a) are obtained at a fluence of $3.6 \times 10^4 \text{ cm}^{-2}$ with dosimetric spectrometer effectiveness $\varepsilon_2 = 0.895$ (b) at $3.8 \times 10^8 \text{ cm}^{-2}$ with dosimetric spectrometer effectiveness $\varepsilon_2 = 0.997$, and (c) at $2.1 \times 10^{10} \text{ cm}^{-2}$ with dosimetric spectrometer effectiveness $\varepsilon_2 = 0.974$.²¹

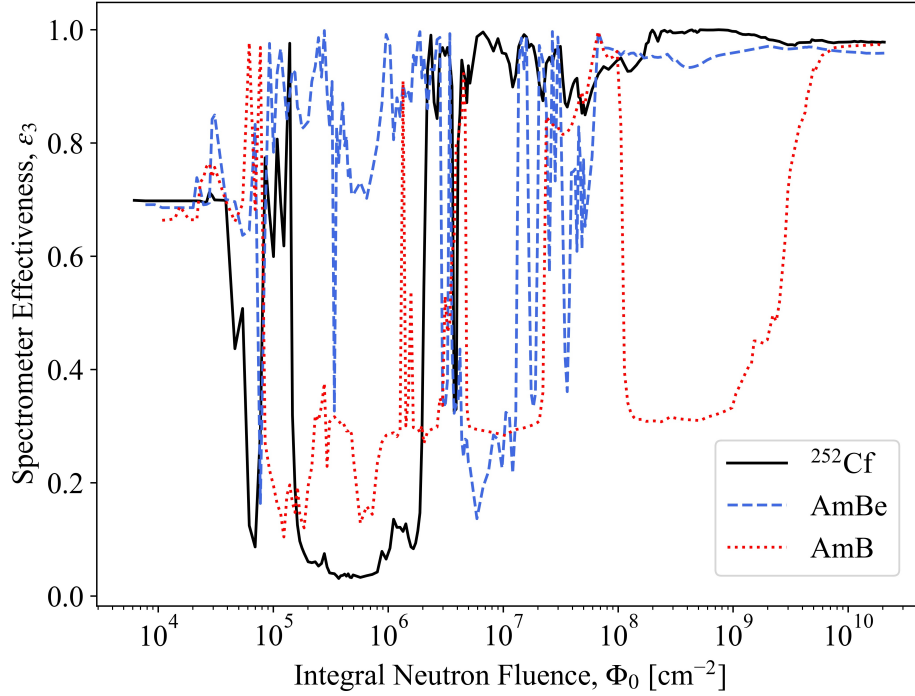


Figure 3.23: Biohazard spectrometer effectiveness as a function of integral neutron fluence for all tested incident neutron energy spectra.²¹

3.2.4 Acceptable Effectiveness Metrics and Minimum Required Neutron Fluence

The integral neutron fluence required to obtain an acceptable spectrometer effectiveness is dependent on the quantity of interest (radiometric, dosimetric, or biometric), the use-case, and the overall complexity of the incident neutron energy spectrum. For this reason, effectiveness acceptability thresholds must be defined for each spectrometer effectiveness metric to determine the smallest neutron fluence necessary to achieve acceptable results. The radiometric spectrometer effectiveness ε_1 is modeled after the square Pearson correlation coefficient, r^2 . Although arbitrary, a correlation coefficient value r at or above 0.8 is generally accepted as a “strong” relationship between two data vectors.⁴⁹ This implies that a squared-correlation coefficient of $0.8^2 = 0.64$ would also indicate a strong relationship. The same interpretation is adopted for ε_1 and $\varepsilon_1 = 0.64$ defines the radiometric spectrometer effectiveness acceptability threshold. Thus, the minimum integral neutron fluence at which $\varepsilon_1 \geq 0.64$ on the ^{252}Cf

Effectiveness	Acceptability Threshold	Φ_0 [cm ⁻²]		
		²⁵² Cf	AmBe	AmB
Radiometric, ε_1	≥ 0.64	2.7×10^8	8.3×10^9	4.4×10^9
Dosimetric, ε_2	≥ 0.64	5.9×10^7	5.9×10^7	2.8×10^9
Biohazard, ε_3	≥ 0.9	6.7×10^7	6.7×10^7	4.7×10^9

Table 3.1: Acceptability thresholds for each spectrometer effectiveness type and integral neutron fluence values at which each spectrum achieves the stated threshold for $N = 2 \times 10^5$ SPUNIT iterations.²¹

radiometric spectrometer effectiveness curve is approximately 2.7×10^8 cm⁻².

The dosimetric spectrometer effectiveness ε_2 is modeled after the coefficient of determination R^2 . R^2 is typically used to assess how well a model fits a data set—in this case, the *model* is the set of refolded dose values D_i^r and the *dataset* is the set of expected dose values D_i . In linear regression analysis, the coefficient of determination R^2 is equal to the squared correlation coefficient r^2 . This is not a case of linear regression analysis, but in lieu of another reasonable threshold, the acceptability threshold for the dosimetric spectrometer effectiveness is also set to $\varepsilon_2 = 0.64$. The biometric spectrometer effectiveness is modeled as a function of the relative error between two quantities. The ε_3 acceptability threshold is taken to be 0.9, as this indicates that the refolded ambient dose equivalent $H_r^*(10\text{ mm})$ is within 10% of the true ambient dose equivalent $H^*(10\text{ mm})$, at which point the result is generally considered “reliable” in Monte Carlo particle transport simulations.⁵⁰ It should also be noted that ε_2 and ε_3 are by no means smooth functions of Φ_0 , evidenced by Figure 3.19 and 3.23. Low-fluence noise results in several instances where ε_2 or ε_3 cross the acceptability threshold. The greatest value of Φ_0 at which ε_2 or ε_3 surpass their respective effectiveness acceptability thresholds are taken to be the minimum required neutron fluence so as to ignore the abundance of low-fluence noise. Table 3.1 shows the various integral neutron fluence thresholds required to achieve minimally acceptable radiometric, dosimetric, and biometric spectrometer effectivenesses (and results) at $N_{\text{it}} = 2 \times 10^5$ SPUNIT iterations.

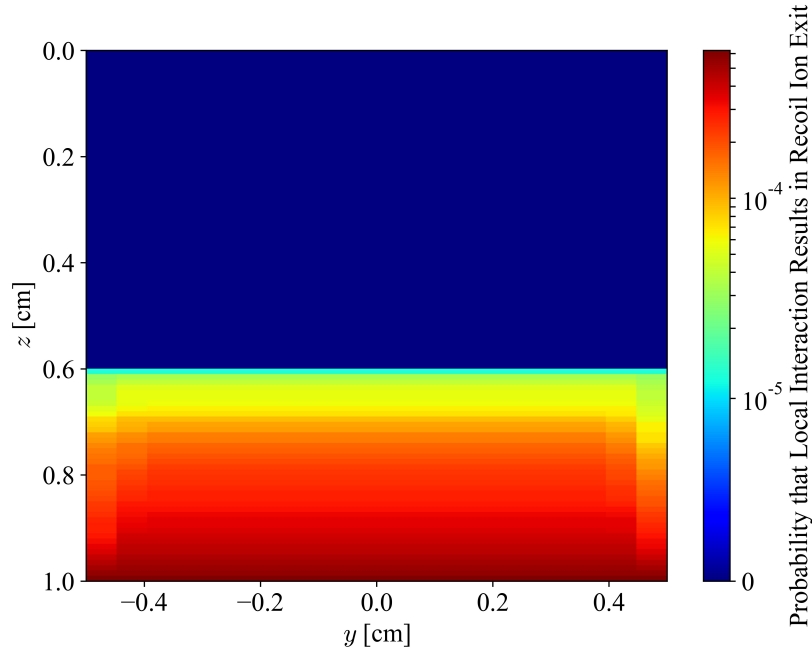


Figure 3.24: *Two-dimensional map of the mean probability that a local elastic neutron scattering interaction results in a recoil ion exiting the back wall of the HDPE block and has a nonzero chance of contributing to the signal charge in one or more unit cell detectors; in this case, $E_n = 20$ MeV.*

3.3 Optimizing the PMFND for Future Studies

3.3.1 HDPE Block Optimization Results

Figure 3.24 shows the probability that a local elastic neutron scattering event with $E_n = 20$ MeV results in a recoil ion exiting the back face of the HDPE block mapped over the entirety of the HDPE block. It is immediately obvious that the first 0.6 cm of the HDPE block are of no use and simply decrease the efficiency of the spectrometer, assuming the user wants the spectrometer to operate for a range of $E_n \in (0, 20)$ MeV. In fact, for any desired energy range $E_n \in (E_{n,\min}, E_{n,\max})$, the maximum HDPE block depth necessary is equal to the range of a recoil proton with $T = E_{n,\max}$.

Figure 3.25 shows the probability that a local elastic neutron scattering event results in a recoil ion exiting the back face of the HDPE block as a function of z_0 for $E_n \in (0, 20)$ MeV. Let \hat{z} be the HDPE depth at which the probability that a local neutron interaction results

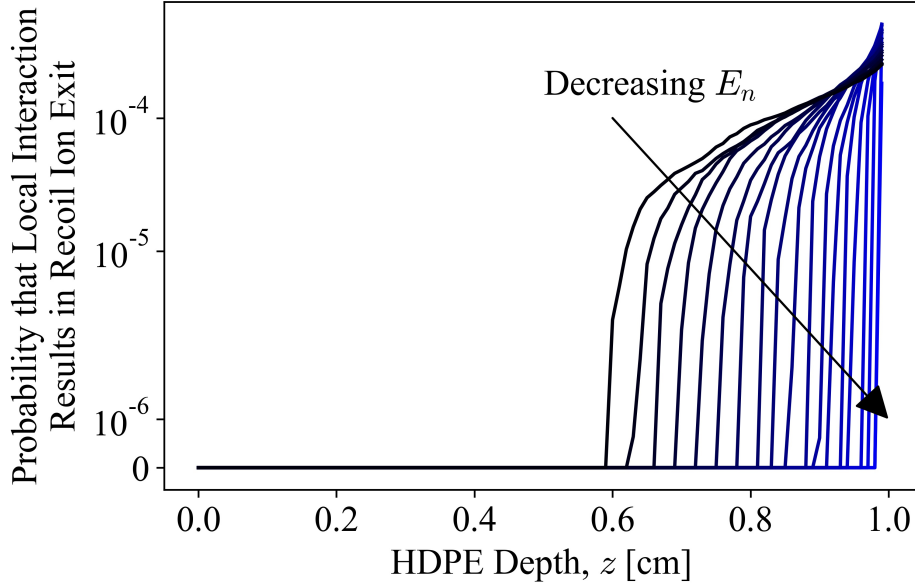


Figure 3.25: Probability that a local interaction at $z = z_0$ results in the production of a recoil ion that exits the HDPE back face for $E_n \in (0, 20)$ MeV.

in a recoil ion exiting the back face of the HDPE block first becomes non-zero. Note that, by definition, the distance from this point to the back face of the HDPE, $\Delta z - \hat{z}$, is exactly equal to $\Lambda_{p,\text{HDPE}}(T)$: the range of a recoil proton in HDPE with kinetic energy $T = E_n$. This implies that the HDPE block operates at maximum neutron-recoil ion conversion efficiency when $\Delta z = \Lambda_{p,\text{HDPE}}(E_{n,\text{max}})$. Figure 3.26 shows the proton range in HDPE overlaid on the $\Delta z - \hat{z}$ values for $E_n \in (0, 20)$ MeV. SRIM and the National Institute of Standards and Technology’s (NIST) Stopping Power and Range Tables for Protons (PSTAR)⁵¹ tool were used to obtain proton range functions in polyethylene. The proton range functions in HDPE and the $\Delta z - \hat{z}$ values align nearly perfectly, firmly establishing a functional relationship between the maximum practical HDPE depth Δz and the maximum incident neutron energy $E_{n,\text{max}}$.

3.3.2 Optimizing Unit Cell Detector Stack

Figures 3.27 and 3.28 both show the proton stopping power as a function of PMFND depth (excluding HDPE), overlaid on top of the PMFND geometry, for initial recoil proton energies

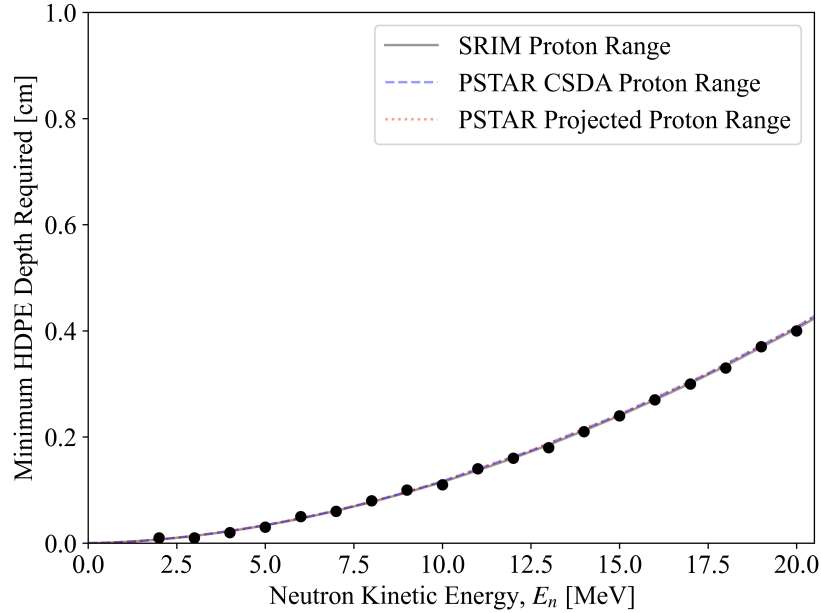


Figure 3.26: *Black points represent the depth at which the probability of a local neutron interaction resulting in a recoil ion exiting the back face of the HDPE block becomes non-zero as a function of incident neutron kinetic energy overlaid on proton ranges in HDPE.*

from $T \in (0, 20)$ MeV. Note that in Figure 3.27, there are many “spikes” in the stopping power curves that coincide with locations where separate unit cell detectors meet (the metallization and insulation segments). Figure 3.28 removes these spikes for improved readability using a simple rolling average procedure. This rolling average procedure involves numerically approximating the first derivative of each stopping power function, $d/dz(-dT/dz)$. Within spatial regions in which $d/dz(-dT/dz) > 0.001 \text{ MeV } \mu\text{m}^{-2}$, the stopping power function values $(-dT/dz)_\ell$ are redefined as

$$\left(-\frac{dT}{dz}\right)_\ell := \frac{1}{2} \left[\left(-\frac{dT}{dz}\right)_{\ell-5} + \left(-\frac{dT}{dz}\right)_{\ell+5} \right], \quad (3.4)$$

where ℓ is the stopping power data vector index. This process is repeated ten times to remove the large spikes in energy deposition that occur in the metallization and insulation layers.

The most important observation from Figures 3.27 and 3.28 is that the 20-unit cell detector PMFND does not contain enough unit cell detectors to capture the full stopping

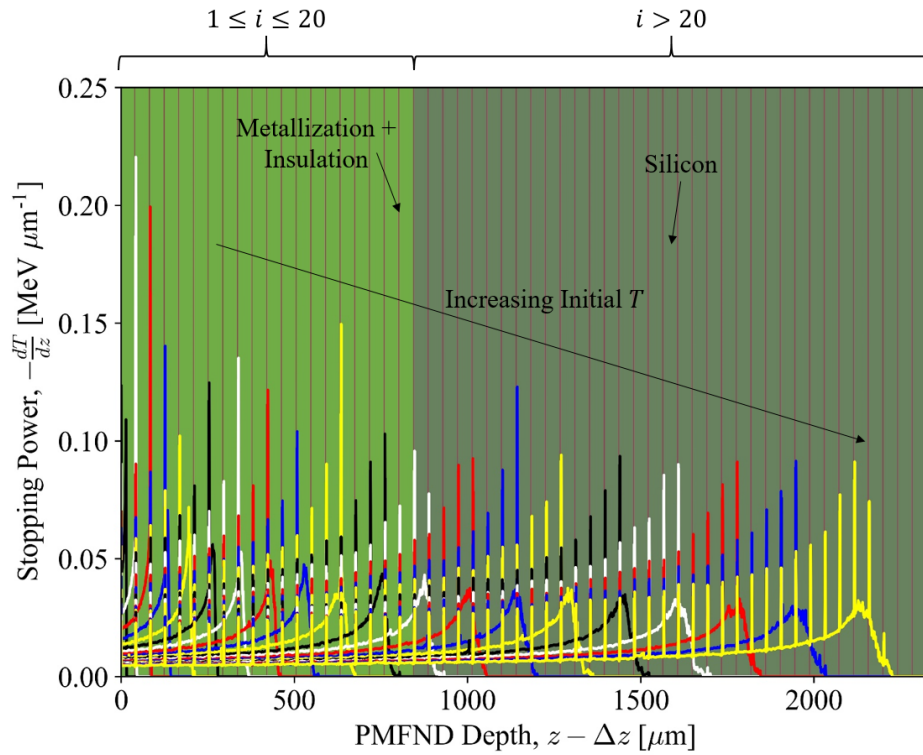


Figure 3.27: Proton stopping power as a function of PMFND depth (excluding HDPE) overlaid on PMFND schematic; green background indicates silicon detection region, magenta line indicates metallization/insulation layers, darkened background indicates unit cell layers beyond unit cell $i = 20$.

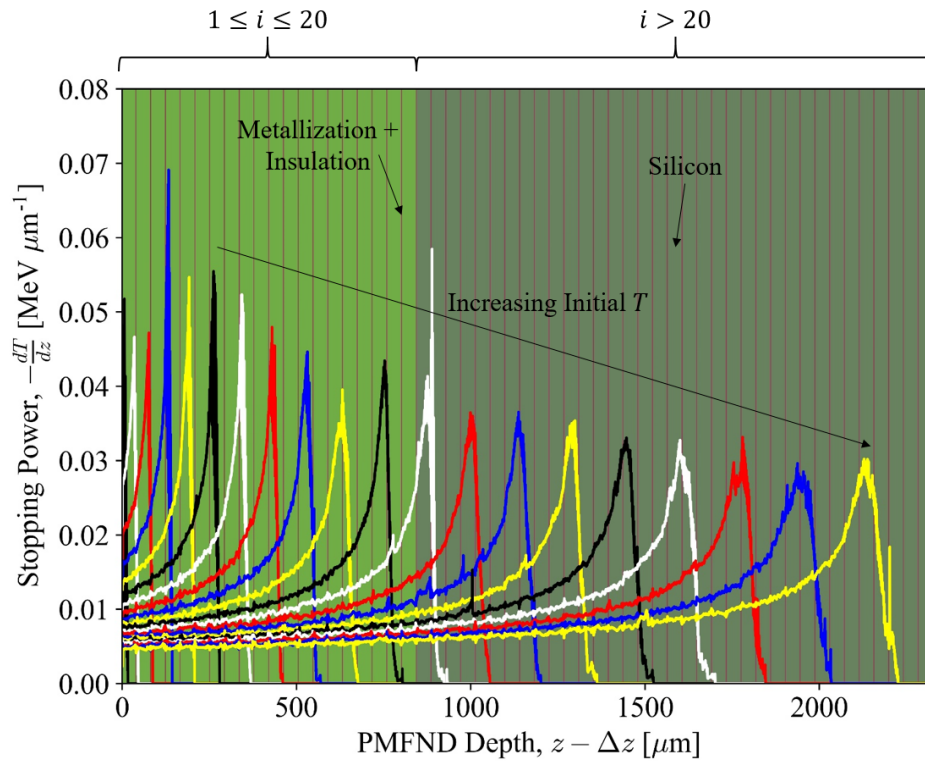


Figure 3.28: Proton stopping power as a function of PMFND depth (excluding HDPE) overlaid on PMFND schematic; green background indicates silicon detection region, magenta line indicates metallization/insulation layer, darkened background indicates unit cell layers beyond unit cell $i = 20$; spikes in stopping power at each metallization/insulation layer are suppressed to improve readability.

power profiles of all $T \in (0, 20)$ MeV; a large amount of spectroscopic information is lost according to this model. 53 unit cell detectors are required to fully slow down a forward-directed proton with initial energy $T = 20$ MeV. Currently, the 20-unit cell PMFND will only fully stop recoil protons $T \in (0, 11.5)$ MeV. This does not necessarily mean that an incident neutron energy spectrum that spans $E_n \in (0, 20)$ MeV *cannot* be reconstructed by a 20-unit cell detector PMFND, but it is likely that spectrum details in the $E_n \in (11.5, 20)$ MeV range would not be well-reflected in the unfolded spectrum. In this work, the ^{252}Cf , AmB, and AmBe spectra were used to test the PMFND's ability to unfold incident neutron energy spectra. The ^{252}Cf and AmB spectrum reconstructions shown in Figures 3.9 and 3.10 appear unaffected by the “missing” spectroscopic information for $E_n \gtrsim 11.5$ MeV because those incident spectra are either close to zero or zero for $E_n \gtrsim 11.5$ MeV. In the case of AmBe, the incident spectrum goes to zero at $E_n = 11.0$ MeV. This may explain why the rightmost peak of the unfolded AmBe spectrum in Figure 3.11 is shifted to the left relative to the position of the same peak in the incident spectrum.

Figure 3.28 makes it clear that the width of the each Bragg peak increases as the initial recoil proton energy increases. This means that higher energy recoil protons deposit most of their energy across several unit cell detectors whereas lower energy recoil protons deposit their energy in a single unit cell detector. These data can be used to systematically increase the thickness of deeper unit cell detectors. The full-width at half maximum (FWHM) for each smoothed stopping power curve shown in Figure 3.28 were numerically estimated. Figure 3.29 shows the estimated FWHM for each Bragg peak as a function of incident recoil proton energy and a linear line of best fit. The line of best fit, including the point $(0, 0)$, is given by

$$\text{FWHM}(T) \approx (8.558 \mu\text{m MeV}^{-1})T. \quad (3.5)$$

Equation 3.5 can be used to generate a stack of unit cell detectors of variable thickness Δz_i , assuming the user wants each unit cell detector to collect *most* of the spectroscopic information within the energy range $E_i \pm 0.5$ MeV in a single unit cell detector where E_i is

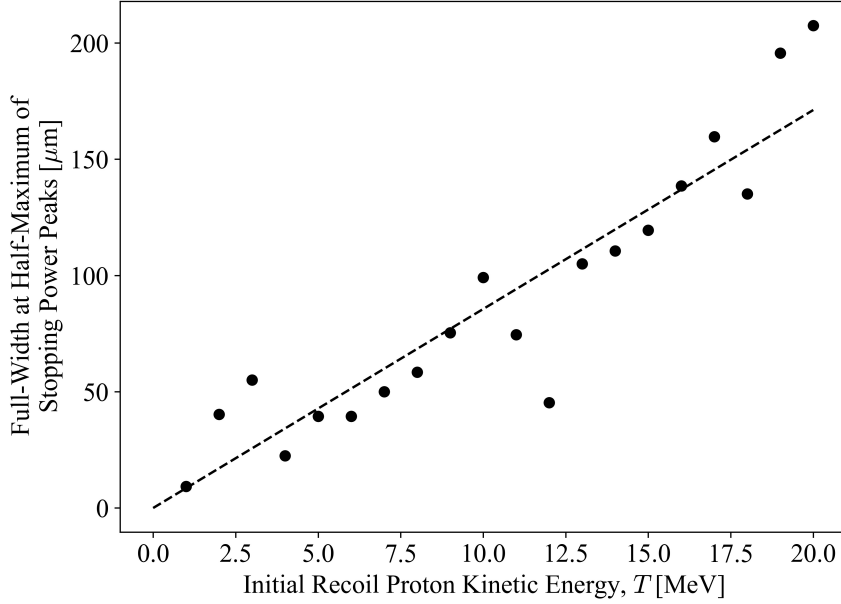


Figure 3.29: *FWHM of each smoothed Bragg peak of Figure 3.28 and best fit line as a function of initial recoil proton kinetic energy.*

the desired “central energy” about which a specific unit cell detector is centered.

The range of the recoil protons in the PMFND unit cell detectors also appears to increase non-linearly with initial energy. These data can be used to develop a “rule of thumb” to estimate the number of uniform thickness unit cell detectors that may be necessary to capture all spectroscopic information from an incident spectrum with $E_n \in (0, E_{n,\max})$. Figure 3.30 shows the proton range in the PMFND unit cell detector stack as a function of initial proton recoil energy, compares this range with that of natural silicon, and fits a curve to the proton range data. The curve fit to the range data is the same as that used for most proton range parameterizations,

$$\Lambda_{p,\text{PMFND}}(T) \approx \frac{1}{\rho} 10^{\tilde{a} + \tilde{b} \log_{10}(T) + \tilde{c} (\log_{10}(T))^2}, \quad (3.6)$$

where \tilde{a} , \tilde{b} , and \tilde{c} are all unitless fitting parameters, ρ is in g cm^{-3} , and T is in MeV.⁴⁸ The fitting parameters are given explicitly in Table 3.2 for $\rho = 2.33 \text{ g cm}^{-3}$. This function fits the data shown in Figure 3.30 exceedingly well. The difference between the pure silicon proton range functions and $\Lambda_{p,\text{PMFND}}(T)$ is due to the presence of the thin metallization and

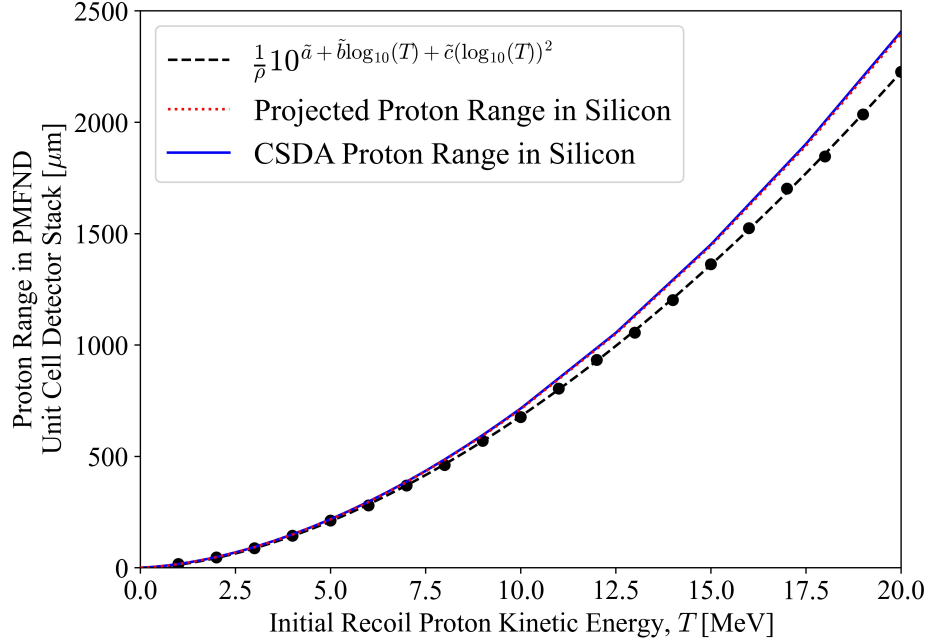


Figure 3.30: Recoil proton range in PMFND unit cell detector stack as a function of initial recoil proton kinetic energy compared with proton range in silicon.

Parameter	\tilde{a}	\tilde{b}	\tilde{c}
Value	1.4982	1.6946	0.0069

Table 3.2: Fitting parameters for Equation 3.6 assuming silicon density $\rho = 2.33 \text{ g cm}^{-3}$.

insulation layers in each unit cell.

Assuming Equation 3.6 predicts the range of protons in the PMFND unit cell detector stack adequately well beyond $T = 20 \text{ MeV}$, the number of uniformly sized unit cell detectors necessary to capture all spectroscopic information for an incident neutron energy spectrum with an energy domain of $E_n \in (0, E_{n,\text{max}})$ is

$$I = \text{ceiling} \left(\frac{\Lambda_{p,\text{PMFND}}(E_{n,\text{max}})}{\Delta z_i + 2\Delta z_{\text{dead},i} + 2\Delta z_{\text{met},i} + \Delta z_{\text{ins},i}} \right). \quad (3.7)$$

3.3.3 Non-Proton Recoil Ion Elimination

From the unfolded neutron energy spectra shown throughout this work (most prominently in Figures 3.9, 3.10, and 3.11), there is some concern that peaks that neutron energy spectra structures in the low-energy region ($E_n \in (0, 1) \text{ MeV}$) are not readily reproduced. This may

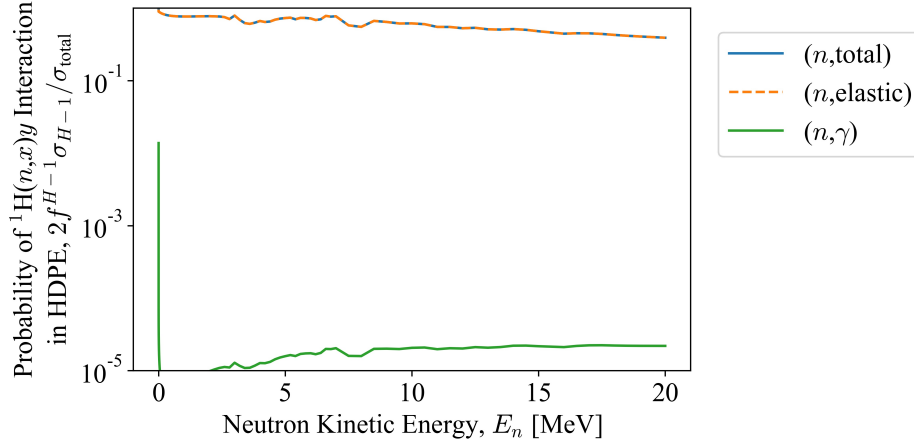


Figure 3.31: Probability of producing a ${}^1_1\text{H}$ recoil ion via interaction in HDPE as a function of incident neutron kinetic energy E_n ; cross section data from ENDF-VIII.0⁵² via JANIS.⁵³

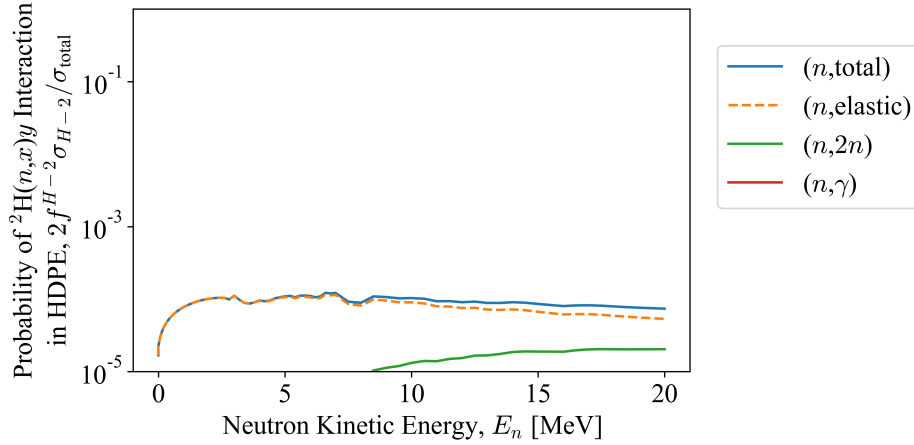


Figure 3.32: Probability of producing a ${}^2_1\text{H}$ recoil ion via interaction in HDPE as a function of incident neutron kinetic energy E_n ; cross section data from ENDF-VIII.0⁵² via JANIS.⁵³

be due to either the build-up of ${}^{12}_6\text{C}$ and ${}^2_1\text{H}$ ions in the first unit cell detector, or that the probability of generating a low-energy recoil proton in the HDPE block, at the right location (near the back face), and that proton ultimately contributes to the collected charge in the first unit cell, is too small.

Figures 3.31, 3.32, and 3.33 show the probability of a neutron of incident energy E_n interacting in the HDPE block, separated by interaction type, and producing ${}^1_1\text{H}$, ${}^2_1\text{H}$, and ${}^{12}_6\text{C}$ recoil ions, respectively.

Figure 3.32 shows that the probability of producing a recoil ${}^2_1\text{H}$ due to a neutron inter-

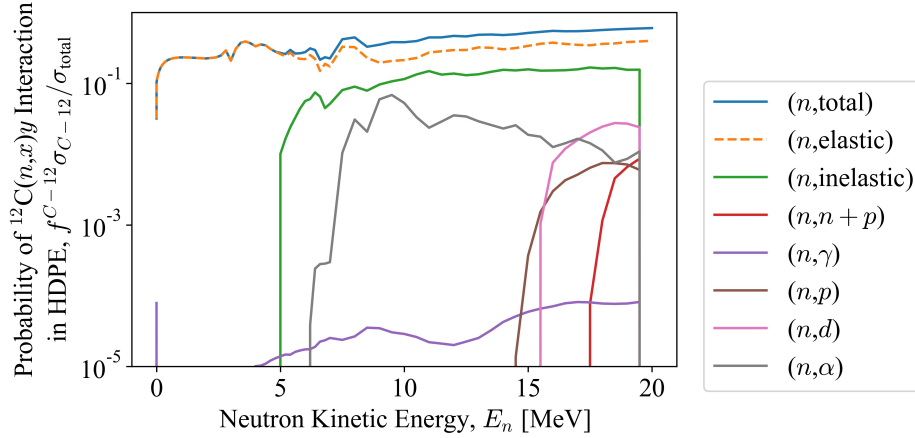


Figure 3.33: Probability of producing a $^{12}_6\text{C}$ recoil ion via interaction in HDPE as a function of incident neutron kinetic energy E_n ; cross section data from ENDF-VIII.0⁵² via JANIS.⁵³

action in HDPE is extremely low for any E_n . The concern that ^2_1H recoil ions distort the energy deposition distribution in the first unit cell detector can be dismissed immediately. Figures 3.31 and 3.33 show that the probabilities of generating recoil protons and generating recoil $^{12}_6\text{C}$ ions are of similar magnitude over the entire energy range. The contribution of $^{12}_6\text{C}$ recoil ion energy deposition in the first unit cell detector cannot yet be dismissed.

Figure 3.34 shows a series of $^{12}_6\text{C}$ recoil ion stopping power profiles produced from SRIM simulations overlaid on a fraction of the first unit cell detector in the PMFND detector stack. SRIM simulations were conducted via the method described in Section 2.4.2.2. Figure 3.34 shows that carbon recoil ions produced at the interface between the HDPE block and the first unit cell detector do not deposit any energy in the active detection region for $T < 3.41$ MeV, which corresponds to the maximum kinetic energy a $^{12}_6\text{C}$ recoil ion can inherit from an elastic collision with an incident neutron of $E_n = 12$ MeV. Carbon ions produced from neutrons with $E_n \geq 12$ MeV can potentially deposit energy in the first unit cell detector, but this is still unlikely due to the minuscule range of $^{12}_6\text{C}$ in HDPE and the metallization layer constituents.

Since neither the ^2_1H nor $^{12}_6\text{C}$ recoil ions appear to significantly affect energy deposition in the first unit cell detector of the PMFND, the inability of the PMFND to reconstruct spectral features in the low-energy range is likely due to some other cause. It is possible that

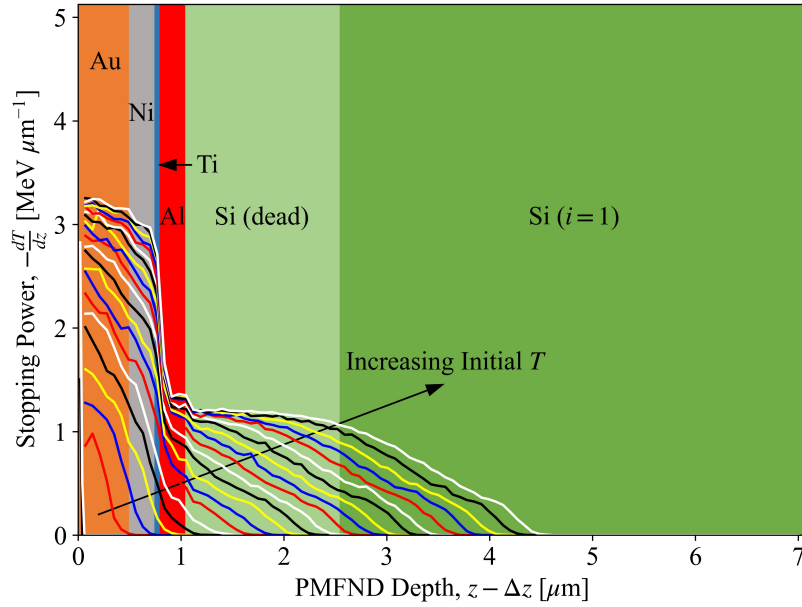


Figure 3.34: Series of $^{12}_6\text{C}$ recoil ion stopping power profiles with initial kinetic energies $T \in [0.284, 5.680]$ MeV overlaid on first unit cell detector of PMFND.

the probability that a low-energy incident neutron produces a similar-energy recoil proton that deposits most or all of its energy in the first unit cell detector of the PMFND is just too small to facilitate spectral reconstruction at low-energies. This is reflected in the absorbed dose response functions shown in Figure 3.1, as the absorbed dose response in all unit cell detectors is minimal for $E_n \in (0, 1)$ MeV.

Chapter 4

Conclusions

Accurate cancer risk estimation due to neutron exposure requires accurate knowledge of the incident neutron energy spectrum to a high position-resolution. Existing neutron spectrometers, intended to measure the incident neutron energy spectrum, are too large and unwieldy to maintain a high spatial resolution and be used for personal dosimetry purposes. The MFND was conceived to be a high position-resolution area monitoring tool for personal dosimetry purposes. In this work, three substantial studies were carried out to develop an understanding and build up the utility of the PMFND. The first study sought to determine

- If the PMFND could unfold an incident neutron energy spectrum without *a priori* information,
- How the number of unit cell detectors (I) in the PMFND affect the PMFND's ability to unfold incident neutron energy spectra, and
- If either the NNLS unfolding method or the SPUNIT method provide better reconstructions of the incident neutron energy spectrum.

In the first study, PHITS was used to generate absorbed dose response functions and absorbed dose values due to incident ^{252}Cf , AmB, and AmBe spectra. The NNLS unfolding method and the SPUNIT method were used to attempt to unfold neutron energy spectra incident

upon PMFNDs with $I = 5$ and $I = 20$ -unit cell detectors. The results of the first study show that

- The PMFND is capable of reconstructing a number of incident neutron energy spectra assuming no *a priori* information,
- PMFNDs with more unit cell detectors (greater I) generally result in unfolded neutron energy spectra that more closely match incident neutron energy spectra,
- The SPUNIT unfolding method is generally superior to the NNLS unfolding method because it preserves maximum energy resolution and reconstructs fine details in the incident neutron energy spectrum.

The second study sought to determine

- How to quantitatively evaluate the effectiveness of the PMFND as a neutron spectrometer, and
- The integral neutron fluence necessary to achieve acceptable unfolding results.

In the second study, PHITS was used to generate absorbed dose values due to incident ^{252}Cf , AmB, and AmBe spectra as a function of integral neutron fluence. The SPUNIT method was used to unfold neutron energy spectra incident upon the PMFND with $I = 20$ -unit cell detectors. Three quantities—the radiometric, dosimetric, and biometric spectrometer effectiveness—were defined based on existing statistical quantities that quantify the relationship between two related variables. The results of the second study show that

- The spectrometer effectiveness can be defined in three different ways: the radiometric spectrometer effectiveness ε_1 defined in Equation 2.24, the dosimetric spectrometer effectiveness ε_2 defined in Equation 2.29, and the biometric spectrometer effectiveness ε_3 defined in Equation 2.33, and
- The integral neutron fluence required to achieve acceptable unfolding results varies depending on the spectrometer effectiveness metric used for evaluation; integral neutron

fluence values for which spectrometer effectiveness metrics pass acceptance thresholds for each incident neutron energy spectrum are given in Table 3.1.

The third study sought to determine

- How the HDPE block of the PMFND can be optimized to improve PMFND performance,
- How the unit cell detectors of the PMFND can be optimized to improve PMFND performance, and
- If the concept of the PMFND can be generalized to work for a wider range of neutron environments.

In the third study, the HDPE neutron-proton converter block and the unit cell detector stack of the PMFND were characterized in an attempt to optimize them to be suitable for an arbitrary neutron energy range $E_n \in (0, E_{n,\max})$. A custom Monte Carlo procedure was constructed to evaluate the probability that a normally incident neutron of energy E_n interacts at (x_0, y_0, z_0) in the HDPE block of dimensions $(\Delta x, \Delta y, \Delta z)$, produces a recoil ion via elastic scattering, and that ion exits the back face of the HDPE block, giving it a chance to deposit energy in one or more unit cell detectors. SRIM and `pysrim` were used to generate range and stopping power profiles for recoil protons as a function of initial recoil ion energy T to determine the number (or thickness as a function of z) of unit cell detectors necessary to capture all spectroscopic information available from an arbitrary incident neutron energy spectrum with an energy range $E_n \in (0, E_{n,\max})$. The results of the study show that

- The optimal HDPE block thickness, for any neutron energy range, is simply the range of a proton with $T = E_{n,\max}$, that is, $\Delta z = \Lambda_{p,\text{HDPE}}(E_{n,\max})$, and
- The minimum required number of uniform thickness unit cell detectors to capture all spectroscopic information for the general energy range $E_n \in (0, E_{n,\max})$ is given by Equation 3.7, and thus

- The PMFND concept *is* extensible in the sense that wider neutron energy ranges can be accounted for by the PMFND by increasing/reducing thicknesses or increasing/decreasing the number unit cell detectors.

4.1 Future Work

The iteration of the PMFND design shown in this work is an early-stage concept. Some fabrication and testing of a PMFND prototype has already taken place.⁵⁴ Ultimately, a spherical version of the MFND (SMFND), like the one shown in Figure 4.1, is desired due to its isotropic response. A series of PHITS simulations, similar to those described in this work, could be conducted on the SMFND to develop absorbed dose response functions, absorbed dose values due to incident neutron energy spectra, and spectrometer effectiveness curves as a function of integral neutron fluence. Anisotropy in the SMFND geometry necessary for wiring purposes could also be accounted for with solid angle-dependent response functions.

The optimization methods described in this work can be improved. The relative error introduced by SRIM simulations when computing stopping power profiles is likely fairly high due to too few histories per simulation—however, this is impossible to confirm without modifying SRIM, which is closed-source. If one were to generate enough proton stopping power profiles in the PMFND detector stack, the calculation used to compute the probability of a neutron interacting in HDPE and resulting in a recoil ion entering the PMFND detector stack could be combined with the data provided by stopping power profiles to predict energy deposition distributions in the PMFND detector stack. A litany of full-scale Monte Carlo simulations could be conducted to verify that optimization methods are effective.

The PMFND and SMFND are envisioned as high position-resolution neutron spectrometers and/or personal dosimeters for use in a variety of neutron environments. Environments of particular interest include radiation therapy centers and aboard spacecraft due to the relative unpredictability of the local secondary neutron energy spectra. Neutron energy spectra in radiation therapy centers develop from charged particles—like protons emitted from a proton therapy machine during a treatment session—interacting with patients and

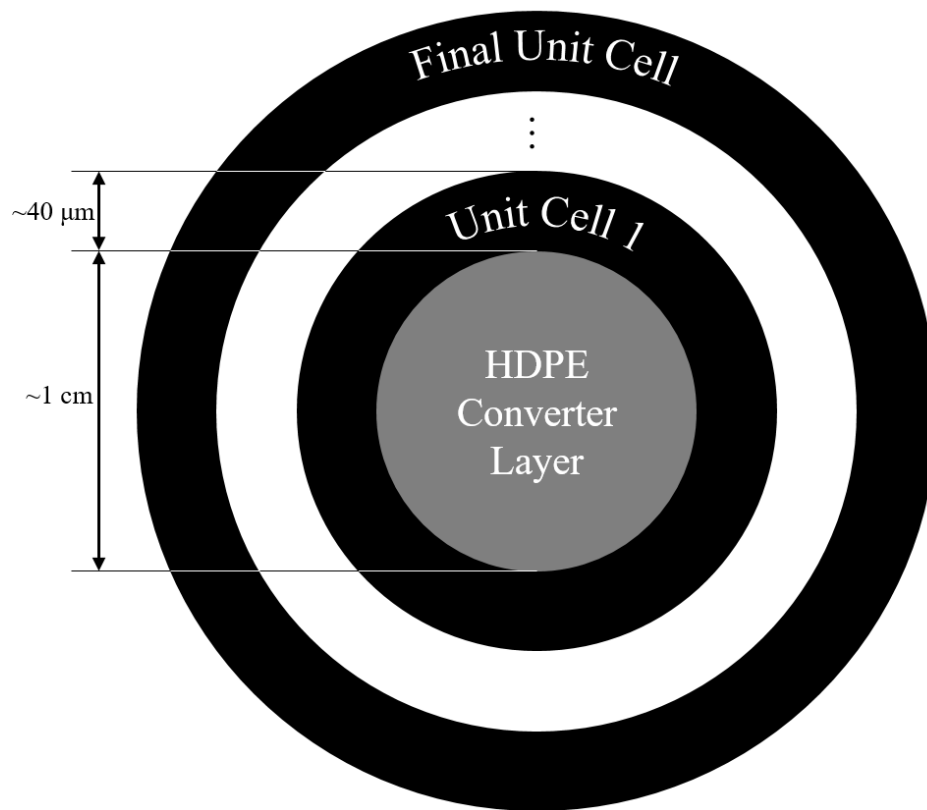


Figure 4.1: *Spherical MFND concept.*

other adjacent equipment. Neutron energy spectra aboard spacecraft develop as high-energy, heavy, charged particles from galactic cosmic rays and solar particle events interact with the hull of the spacecraft and adjacent equipment. It is envisioned that astronauts and medical radiation technicians could don a PMFND or SMFND on their chest, much like a thermoluminescent dosimeter badge, to more accurately estimate occupational cancer risk due to neutron exposure.

Bibliography

- [1] David B Richardson, Elisabeth Cardis, Robert D Daniels, Michael Gillies, Jacqueline A O'Hagan, Ghassan B Hamra, Richard Haylock, Dominique Laurier, Klervi Leuraud, Monika Moissonnier, et al. Risk of cancer from occupational exposure to ionising radiation: retrospective cohort study of workers in France, the United Kingdom, and the United States (INWORKS). *BMJ*, 351, 2015.
- [2] P K Sarkar. Neutron dosimetry in the particle accelerator environment. *Radiation Measurements*, 45(10):1476–1483, 2010.
- [3] Christina Zacharatou Jarlskog and Harald Paganetti. Risk of developing second cancer from neutron dose in proton therapy as function of field characteristics, organ, and patient age. *International Journal of Radiation Oncology* Biology* Physics*, 72(1): 228–235, 2008.
- [4] R J M Fry. The radiation protection problems of high altitude and space flight. Technical report, Oak Ridge National Laboratory, 1993.
- [5] Francis A Cucinotta. *Space radiation cancer risk projections for exploration missions: uncertainty reduction and mitigation*. DIANE Publishing, 2002.
- [6] Ravinder Nath. *Neutron measurements around high energy x-ray radiotherapy machines: a report of Task Group 27, Radiation Therapy Committee, American Association of Physicists in Medicine*. American Inst. of Physics, 1987.
- [7] T W Armstrong and B L Colborn. Predictions of secondary neutrons and their importance to radiation effects inside the International Space Station. *Radiation measurements*, 33(3):229–234, 2001.

- [8] ICRP. 1990 recommendations of the International Commission on Radiological Protection. *Annals of the ICRP*, 21(1-3), 1991.
- [9] ICRP. The 2007 recommendations of the International Commission on Radiological Protection. *Annals of the ICRP*, 37(2-4), 2007.
- [10] L J Chappel, C M Milder, and S R Elgart. NASA space cancer risk model: 2020 operational implementation. Technical report, NASA, 2021. URL <https://ntrs.nasa.gov/citations/20210013314>.
- [11] F D Brooks and H Klein. Neutron spectrometry—historical review and present status. *Nuclear Instruments and Methods in Physics Research Section A: Accelerators, Spectrometers, Detectors and Associated Equipment*, 476(1-2):1–11, 2002.
- [12] A Pietropaolo, M Angelone, R Bedogni, N Colonna, A J Hurd, A Khaplanov, F Murtas, M Pillon, F Piscitelli, E M Schooneveld, and K Zeitelhack. Neutron detection techniques from μeV to GeV. *Physics Reports*, 875:1–65, 2020. ISSN 0370-1573. doi: <https://doi.org/10.1016/j.physrep.2020.06.003>. URL <https://www.sciencedirect.com/science/article/pii/S0370157320302490>. Neutron detection techniques from μeV to GeV.
- [13] D J Thomas and A V Alevra. Bonner sphere spectrometers—a critical review. *Nuclear Instruments and Methods in Physics Research Section A: Accelerators, Spectrometers, Detectors and Associated Equipment*, 476(1):12–20, 2002. ISSN 0168-9002. doi: [https://doi.org/10.1016/S0168-9002\(01\)01379-1](https://doi.org/10.1016/S0168-9002(01)01379-1). URL <https://www.sciencedirect.com/science/article/pii/S0168900201013791>. Int. Workshop on Neutron Field Spectrometry in Science, Technology and Radiation Protection.
- [14] C B Hoshor, T M Oakes, E R Myers, B J Rogers, J E Currie, S M Young, J A Crow, P R Scott, W H Miller, S L Bellinger, T J Sobering, R G Fronk, J K Shultis, D S McGregor, and A N Caruso. A portable and wide energy range semiconductor-based neutron spectrometer. *Nuclear Instruments and Methods in Physics Research Section A: Accelerators, Spectrometers, Detectors and Associated Equipment*, 803:68–

- 81, 2015. ISSN 0168-9002. doi: <https://doi.org/10.1016/j.nima.2015.08.077>. URL <https://www.sciencedirect.com/science/article/pii/S0168900215010499>.
- [15] J K Shultis and D S McGregor. Design and performance considerations for perforated semiconductor thermal-neutron detectors. *Nuclear Instruments and Methods in Physics Research Section A: Accelerators, Spectrometers, Detectors and Associated Equipment*, 606(3):608–636, 2009. ISSN 0168-9002. doi: <https://doi.org/10.1016/j.nima.2009.02.033>. URL <https://www.sciencedirect.com/science/article/pii/S016890020900391X>.
- [16] J Bart Czirr, David B Merrill, David Buehler, Thomas K McKnight, James L Carroll, Thomas Abbott, and Eva Wilcox. Capture-gated neutron spectrometry. *Nuclear Instruments and Methods in Physics Research Section A: Accelerators, Spectrometers, Detectors and Associated Equipment*, 476(1):309–312, 2002. ISSN 0168-9002. doi: [https://doi.org/10.1016/S0168-9002\(01\)01445-0](https://doi.org/10.1016/S0168-9002(01)01445-0). URL <https://www.sciencedirect.com/science/article/pii/S0168900201014450>. Int. Workshop on Neutron Field Spectrometry in Science, Technology and Radiation Protection.
- [17] Philip Holm, Kari Peräjärvi, Samu Ristkari, T. Siiskonen, and Harri Toivonen. A capture-gated neutron spectrometer for characterization of neutron sources and their shields. *Nuclear Instruments and Methods in Physics Research Section A Accelerators Spectrometers Detectors and Associated Equipment*, 751:48–54, 07 2014. doi: 10.1016/j.nima.2014.03.021.
- [18] National Council on Radiation Protection and Measurements NCRP. *Protection Against Neutron Radiation*. NCRP report. National Council on Radiation Protection and Measurements, 1971. URL <https://books.google.com/books?id=sThjzQEACAAJ>.
- [19] Richard H Olsher, David T Graves, Shawna L Eisele, Christopher W Bjork, William A Martinez, Leonard L Romero, Michael W Mallett, Michael A Duran, and Charles R Hurlbut. PRESCILA: a new, lightweight neutron rem meter. *Health Physics*, 86(6): 603–612, June 2004. doi: 10.1097/00004032-200406000-00005.

- [20] Amir Bahadori and Zayd Leseman. Miniaturized fast neutron spectrometer, August 2021. URL <https://www.freepatentsonline.com/y2021/0239865.html>.
- [21] Luke Stegeman, Tyler Hieber, Dipta Sarkar, Samuel W Oxandale, Steven L Bellinger, Zayd C Leseman, and Amir A Bahadori. Planar Miniaturized Fast Neutron Detector spectroscopy evaluation. *Nuclear Instruments and Methods in Physics Research Section A: Accelerators, Spectrometers, Detectors and Associated Equipment*, 1020: 165865, 2021. ISSN 0168-9002. doi: <https://doi.org/10.1016/j.nima.2021.165865>. URL <https://www.sciencedirect.com/science/article/pii/S0168900221008500>.
- [22] Takashi Nakamura. Cosmic-ray neutron spectrometry and dosimetry. *Journal of Nuclear Science and Technology*, 45(sup5):1–7, 2008. doi: 10.1080/00223131.2008.10875772. URL <https://doi.org/10.1080/00223131.2008.10875772>.
- [23] Timothy D Malouff, Anita Mahajan, Sunil Krishnan, Chris Beltran, Danushka S Seneviratne, and Daniel Michael Trifiletti. Carbon ion therapy: A modern review of an emerging technology. *Frontiers in Oncology*, 10, 2020. ISSN 2234-943X. doi: 10.3389/fonc.2020.00082. URL <https://www.frontiersin.org/article/10.3389/fonc.2020.00082>.
- [24] Tatsuhiko Sato, Yosuke Iwamoto, Shintaro Hashimoto, Tatsuhiko Ogawa, Takuya Furuta, Shin ichiro Abe, Takeshi Kai, Pi-En Tsai, Norihiro Matsuda, Hiroshi Iwase, Nobuhiro Shigyo, Lembit Sihver, and Koji Niita. Features of Particle and Heavy Ion Transport code System (PHITS) version 3.02. *Journal of Nuclear Science and Technology*, 55(6):684–690, 2018. doi: 10.1080/00223131.2017.1419890. URL <https://doi.org/10.1080/00223131.2017.1419890>.
- [25] H. Hirayama, Y. Namito, A. F. Bielajew, S. J. Wilderman, and W. R. Nelson. The EGS5 code system, 2005.
- [26] K. Iida, A. Kohama, and K. Oyamatsu. Formula for proton-nucleus reaction cross section at intermediate energies and its application. *Journal of the Physical Society of*

- Japan*, 76(4), 2007. doi: 10.1143/JPSJ.76.044201. URL <https://doi.org/10.1143/JPSJ.76.044201>.
- [27] Luke A Stegeman, Quentin Pease, Tyler J Hieber, Dipta Sarkar, Samuel W Oxandale, Steven L Bellinger, Zayd C Leseman, and Amir A Bahadori. Neutron spectrum unfolding with a planar Miniaturized Fast-Neutron Detector. *Transactions of the American Nuclear Society*, 120:740–743, 2019.
- [28] James F Ziegler, M D Ziegler, and J P Biersack. SRIM – the stopping and range of ions in matter (2010). *Nuclear Instruments and Methods in Physics Research Section B: Beam Interactions with Materials and Atoms*, 268(11):1818–1823, 2010. ISSN 0168-583X. doi: <https://doi.org/10.1016/j.nimb.2010.02.091>. URL <https://www.sciencedirect.com/science/article/pii/S0168583X10001862>. 19th International Conference on Ion Beam Analysis.
- [29] T Sato, Y Iwamoto, S Hashimoto, T Ogawa, T Furuta, S Abe, T Kai, Y Matsuya, N Matsuda, Y Hirata, L Yao, P-E Tsai, H Ratliff, H Iwase, Y Sakaki, N Shigyo, L Sihver, and K Niita. Particle and Heavy Ion Transport code System—general introduction, 2022. URL <https://phits.jaea.go.jp/lec/phits-introduction-en.pdf>.
- [30] Keiichi Shibata, Osamu Iwamoto, Tsuneo Nakagawa, Nobuyuki Iwamoto, Akira Ichihara, Satoshi Kunieda, Satoshi Chiba, Kazuyoshi Furutaka, Naohiko Otuka, Takaaki Ohsawa, Toru Murata, Hiroyuki Matsunobu, Atsushi Zukeran, So Kamada, and Jun ichi Katakura. Jendl-4.0: A new library for nuclear science and engineering. *Journal of Nuclear Science and Technology*, 48(1):1–30, 2011. doi: 10.1080/18811248.2011.9711675. URL <https://doi.org/10.1080/18811248.2011.9711675>.
- [31] Koji Niita, Tatsuhiko Sato, Yosuke Iwamoto, Shintaro Hashimoto, Tatsuhiko Ogawa, Takuya Furuta, Shinichiro Abe, Takeshi Kai, Pi-En Tsai, NORihiro Matsuda, Yosuke Matsuya, Hunter Ratliff, Hiroshi Iwase, Nobuhiro Shigyo, and Lembit Sihver. PHITS ver. 3.17 user’s manual. Technical report, JAEA, 2019. URL phits.jaea.go.jp/manualE-phits317.pdf.

- [32] T Ogawa, T Sato, S Hashimoto, and K Niita. Development of a reaction ejectile sampling algorithm to recover kinematic correlations from inclusive cross-section data in Monte-Carlo particle transport simulations. *Nuclear Instruments and Methods in Physics Research Section A: Accelerators, Spectrometers, Detectors and Associated Equipment*, 763:575 – 590, 2014. ISSN 0168-9002. doi: <https://doi.org/10.1016/j.nima.2014.06.088>. URL <http://www.sciencedirect.com/science/article/pii/S0168900214008420>.
- [33] Hans Geissel, Christoph Scheidenberger, Peter Malzacher, Jörg Malzacher, Helmut Weick, and Andrej Prochazka. ATIMA. URL <https://web-docs.gsi.de/~weick/atima/>.
- [34] A. Boudard, J. Cugnon, J.-C. David, S. Leray, and D. Mancusi. New potentialities of the Liège intranuclear cascade model for reactions induced by nucleons and light charged particles. *Phys. Rev. C*, 87:014606, Jan 2013. doi: 10.1103/PhysRevC.87.014606. URL <https://link.aps.org/doi/10.1103/PhysRevC.87.014606>.
- [35] S. Furihata. The GEM code - the Generalized Evaporation Model and the fission model. In Andreas Kling, Fernando J. C. Barão, Masayuki Nakagawa, Luis Távora, and Pedro Vaz, editors, *Advanced Monte Carlo for Radiation Physics, Particle Transport Simulation and Applications*, pages 1045–1050, Berlin, Heidelberg, 2001. Springer Berlin Heidelberg. ISBN 978-3-642-18211-2.
- [36] Hideo Hirayama, Yoshihito Namito, Alex Bielajew, Scott Wilderman, and Walter Nelson. The EGS5 code system. Technical report, SLAC National Accelerator Laboratory, 01 2006.
- [37] Koji Niita, Satoshi Chiba, Toshiki Maruyama, Tomoyuki Maruyama, Hiroshi Takada, Tokio Fukahori, Yasuaki Nakahara, and Akira Iwamoto. Analysis of the (n, xn') reactions by quantum molecular dynamics plus statistical decay model. *Phys. Rev. C*, 52:2620–2635, Nov 1995. doi: 10.1103/PhysRevC.52.2620. URL <https://link.aps.org/doi/10.1103/PhysRevC.52.2620>.
- [38] T Sato, R Kataoka, H Yasuda, S Yashiro, T Kuwabara, D Shiota, and Y Kubo. Air

- shower simulation for WASAVIES: warning system for aviation exposure to solar energetic particles. *Radiation Protection Dosimetry*, 161(1-4):274–278, 12 2013. ISSN 0144-8420. doi: 10.1093/rpd/nct332. URL <https://doi.org/10.1093/rpd/nct332>.
- [39] Gerald R Lynch and Orin I Dahl. Approximations to multiple Coulomb scattering. *Nuclear Instruments and Methods in Physics Research Section B: Beam Interactions with Materials and Atoms*, 58(1):6–10, 1991. ISSN 0168-583X. doi: [https://doi.org/10.1016/0168-583X\(91\)95671-Y](https://doi.org/10.1016/0168-583X(91)95671-Y). URL <https://www.sciencedirect.com/science/article/pii/0168583X9195671Y>.
- [40] L Landau. On the energy loss of fast particles by ionisation. *Journal of Physics*, 8(201), 1944.
- [41] Karl Whittle. Radiation damage. In *Nuclear Materials Science*, 2053-2563, pages 2–1 to 2–22. IOP Publishing, 2016. ISBN 978-0-7503-1104-5. doi: 10.1088/978-0-7503-1104-5ch2. URL <https://dx.doi.org/10.1088/978-0-7503-1104-5ch2>.
- [42] pySRIM documentation. <https://pypi.org/project/pysrim/>, 2022. Accessed: 2022-03-13.
- [43] International Organization for Standardization. Reference neutron radiations — part 1: Characteristics and methods of production. Technical Report 8529-1:2001, International Organization for Standardization, 2001. URL <https://www.iso.org/standard/25666.html>.
- [44] scipy.optimize.npls. URL <https://docs.scipy.org/doc/scipy/reference/generated/scipy.optimize.npls.html>.
- [45] Charles L. Lawson and Richard J. Hanson. Solving least squares problems. In *Classics in applied mathematics*, 1995.
- [46] J. J. Doroshenko, S. N. Kraitor, T. V. Kuznetsova, K. K. Kushnereva, and E. S. Leonov. New methods for measuring neutron spectra with energy from 0.4 eV to 10 MeV by

- track and activation detectors. *Nuclear Technology*, 33(3):296–304, 1977. doi: 10.13182/NT77-A31791. URL <https://doi.org/10.13182/NT77-A31791>.
- [47] ICRP. Conversion coefficients for use in radiological protection against external radiation. *Annals of the ICRP*, 26(3-4), 1996.
- [48] J Kenneth Shultis and Richard E Faw. *Radiation Shielding*. American Nuclear Society, La Grange Park, IL, March 2000.
- [49] Haldun Akoglu. User’s guide to correlation coefficients. *Turkish Journal of Emergency Medicine*, 18(3):91–93, 2018. ISSN 2452-2473. doi: 10.1016/j.tjem.2018.08.001.
- [50] J K Shultis and R E Faw. An MCNP primer. Technical report, Kansas State University, 2004-2006.
- [51] M J Berger, J S Coursey, M A Zucker, and J Chang. Estar, pstar, and astar: Computer programs for calculating stopping-power and range tables for electrons, protons, and helium ions (version 1.2.3), 2005. URL <http://physics.nist.gov/Star>.
- [52] D A Brown, M B Chadwick, R Capote, A C Kahler, A Trkov, M W Herman, A A Sonzogni, Y Danon, A D Carlson, M Dunn, D L Smith, G M Hale, G Arbanas, R Arcilla, C R Bates, B Beck, B Becker, F Brown, R J Casperson, J Conlin, D E Cullen, M-A Descalle, R. Firestone, T Gaines, K H Guber, A I Hawari, J Holmes, T D Johnson, T Kawano, B C Kiedrowski, A J Koning, S Kopecky, L Leal, J P Leestone, C Lubitz, J I Márquez Damián, C M Mattoon, E A McCutchan, S Mughabghab, P Navratil, D Neudecker, G P A Nobre, G Noguere, M Paris, M T Pigni, A J Plompen, B Pritychenko, V G Pronyaev, D Roubtsov, D Rochman, P Romano, P Schillebeeckx, S Simakov, M Sin, I Sirakov, B Sleaford, V Sobes, E S Soukhovitskii, I Stetcu, P Talou, I Thompson, S van der Marck, L Welsch-Sherrill, D Wiarda, M White, J L Wormald, R Q Wright, M Zerkle, G Žerovnik, and Y Zhu. ENDF/B-VIII.0: The 8th major release of the nuclear reaction data library with CIELO-project cross sections, new standards and thermal scattering data. *Nuclear Data Sheets*, 148:1–

- 142, 2018. ISSN 0090-3752. doi: <https://doi.org/10.1016/j.nds.2018.02.001>. URL <https://www.sciencedirect.com/science/article/pii/S0090375218300206>. Special Issue on Nuclear Reaction Data.
- [53] N. Soppera, M. Bossant, and E. Dupont. JANIS 4: An improved version of the NEA Java-based nuclear data information system. *Nuclear Data Sheets*, 120:294–296, 2014. ISSN 0090-3752. doi: <https://doi.org/10.1016/j.nds.2014.07.071>. URL <https://www.sciencedirect.com/science/article/pii/S0090375214005237>.
- [54] Samuel W Oxandale, Luke A Stegeman, Tyler J Hieber, Dipta Sarkar, Steven L Bellinger, Amir A Bahadori, and Zayd C Leseman. Fabrication, modeling, and testing of a Miniaturized Fast Neutron Detector. volume Volume 10: Micro- and Nano-Systems Engineering and Packaging of *ASME International Mechanical Engineering Congress and Exposition*, 11 2019. doi: 10.1115/IMECE2019-11534. URL <https://doi.org/10.1115/IMECE2019-11534>. V010T12A002.

Appendix A

PHITS Response Simulation Input File

[T i t l e]
Planar Miniaturized Fast Neutron Detector

[P a r a m e t e r s]
icntl = 0
rseed = -1
maxcas = 5.00E+05
maxbch = 1550
emin(1) = 1.000000000E-03
emin(2) = 1.000000000E-10
dmax(2) = 2.000000000E+01
emin(12) = 1.000000000E-01
emin(13) = 1.000000000E-01
emin(14) = 1.000000000E-03
dmax(12) = 1.000000000E+03
dmax(13) = 1.000000000E+03
dmax(14) = 1.000000000E+03
emin(15) = 1.000000000E-03
emin(16) = 1.000000000E-03
emin(17) = 1.000000000E-03
emin(18) = 1.000000000E-03
emin(19) = 1.000000000E-03
esmin = 1.000000000E-06
emcnf = 1.000000000E+02
e-mode = 2
itall = 1
negs = 1
irqmd = 1
icxsni = 2
nspred = 2

```

istdev      =  -1
nedisp      =   1
file(1)     = /homes/lukesteg/phits317B_ExportControlled/phits
file(6)     =  phits.out
file(7)     =
             /homes/lukesteg/phits317B_ExportControlled/phits/data/xsdir.jnd
file(20)    = /homes/lukesteg/phits317B_ExportControlled/phits/XS/egs

```

[S o u r c e]

```

s-type = 2
proj = neutron
x0 = -5.0000E-01
x1 = 5.0000E-01
y0 = -5.0000E-01
y1 = 5.0000E-01
z0 = -1.0000E-03
z1 = -1.0000E-03
dir = 1.0000
e0 = <E_n>

```

[M a t e r i a l]

```

M1 $ Silicon -- 2.33 g cm-3
   28Si  92.2300
   29Si  4.6800
   30Si  3.0900

```

```

M2 $ Silicon Oxide -- 2.2 g cm-3
   28Si  92.2300
   29Si  4.6800
   30Si  3.0900
   16O  200.0000

```

```

M3 $ High Density Polyethylene -- 0.97 g cm-3
   1H  199.9600
   2H  0.0400
   12C 100.0000

```

```

M4 $ Gold -- 19.32 g cm-3
   Au  1.0000

```

```

M5 $ Nickel -- 8.912 g cm-3
   Ni  1.0000

```

```

M6 $ Titanium -- 4.506 g cm-3
   Ti  1.0000

```

```

M7 $ Aluminum -- 2.7 g cm-3
   Al  1.0000

```

[C e l l]

```

1000  3  -0.970  10000  -10001  -20000  20001  -30000  30001  $ HDPE
1001  4  -19.320 10001  -10002  -20000  20001  -30000  30001  $ Gold

```

1002	5	-8.912	10002	-10003	-20000	20001	-30000	30001	\$	
			Nickel							
1003	6	-4.506	10003	-10004	-20000	20001	-30000	30001	\$	
			Titanium							
1004	7	-2.700	10004	-10005	-20000	20001	-30000	30001	\$	
			Aluminum							
1005	1	-2.330	10005	-10006	-20000	20001	-30000	30001	\$	
			Silicon Dead Layer							
1006	1	-2.330	10006	-10007	-20000	20001	-30000	30001	\$	
			Silicon							
1007	1	-2.330	10007	-10008	-20000	20001	-30000	30001	\$	
			Silicon Dead Layer							
1008	7	-2.700	10008	-10009	-20000	20001	-30000	30001	\$	
			Aluminum							
1009	6	-4.506	10009	-10010	-20000	20001	-30000	30001	\$	
			Titanium							
1010	5	-8.912	10010	-10011	-20000	20001	-30000	30001	\$	
			Nickel							
1011	4	-19.320	10011	-10012	-20000	20001	-30000	30001	\$	Gold
1012	2	-2.200	10012	-10013	-20000	20001	-30000	30001	\$	
			Silicon Oxide							
1013	4	-19.320	10013	-10014	-20000	20001	-30000	30001	\$	Gold
1014	5	-8.912	10014	-10015	-20000	20001	-30000	30001	\$	
			Nickel							
1015	6	-4.506	10015	-10016	-20000	20001	-30000	30001	\$	
			Titanium							
1016	7	-2.700	10016	-10017	-20000	20001	-30000	30001	\$	
			Aluminum							
1017	1	-2.330	10017	-10018	-20000	20001	-30000	30001	\$	
			Silicon Dead Layer							
1018	1	-2.330	10018	-10019	-20000	20001	-30000	30001	\$	
			Silicon							
1019	1	-2.330	10019	-10020	-20000	20001	-30000	30001	\$	
			Silicon Dead Layer							
1020	7	-2.700	10020	-10021	-20000	20001	-30000	30001	\$	
			Aluminum							
1021	6	-4.506	10021	-10022	-20000	20001	-30000	30001	\$	
			Titanium							
1022	5	-8.912	10022	-10023	-20000	20001	-30000	30001	\$	
			Nickel							
1023	4	-19.320	10023	-10024	-20000	20001	-30000	30001	\$	Gold
1024	2	-2.200	10024	-10025	-20000	20001	-30000	30001	\$	
			Silicon Oxide							
1025	4	-19.320	10025	-10026	-20000	20001	-30000	30001	\$	Gold
1026	5	-8.912	10026	-10027	-20000	20001	-30000	30001	\$	
			Nickel							
1027	6	-4.506	10027	-10028	-20000	20001	-30000	30001	\$	
			Titanium							
1028	7	-2.700	10028	-10029	-20000	20001	-30000	30001	\$	
			Aluminum							
1029	1	-2.330	10029	-10030	-20000	20001	-30000	30001	\$	
			Silicon Dead Layer							
1030	1	-2.330	10030	-10031	-20000	20001	-30000	30001	\$	
			Silicon							

1031	1	-2.330	10031	-10032	-20000	20001	-30000	30001	\$
			Silicon Dead Layer						
1032	7	-2.700	10032	-10033	-20000	20001	-30000	30001	\$
			Aluminum						
1033	6	-4.506	10033	-10034	-20000	20001	-30000	30001	\$
			Titanium						
1034	5	-8.912	10034	-10035	-20000	20001	-30000	30001	\$
			Nickel						
1035	4	-19.320	10035	-10036	-20000	20001	-30000	30001	\$ Gold
1036	2	-2.200	10036	-10037	-20000	20001	-30000	30001	\$
			Silicon Oxide						
1037	4	-19.320	10037	-10038	-20000	20001	-30000	30001	\$ Gold
1038	5	-8.912	10038	-10039	-20000	20001	-30000	30001	\$
			Nickel						
1039	6	-4.506	10039	-10040	-20000	20001	-30000	30001	\$
			Titanium						
1040	7	-2.700	10040	-10041	-20000	20001	-30000	30001	\$
			Aluminum						
1041	1	-2.330	10041	-10042	-20000	20001	-30000	30001	\$
			Silicon Dead Layer						
1042	1	-2.330	10042	-10043	-20000	20001	-30000	30001	\$
			Silicon						
1043	1	-2.330	10043	-10044	-20000	20001	-30000	30001	\$
			Silicon Dead Layer						
1044	7	-2.700	10044	-10045	-20000	20001	-30000	30001	\$
			Aluminum						
1045	6	-4.506	10045	-10046	-20000	20001	-30000	30001	\$
			Titanium						
1046	5	-8.912	10046	-10047	-20000	20001	-30000	30001	\$
			Nickel						
1047	4	-19.320	10047	-10048	-20000	20001	-30000	30001	\$ Gold
1048	2	-2.200	10048	-10049	-20000	20001	-30000	30001	\$
			Silicon Oxide						
1049	4	-19.320	10049	-10050	-20000	20001	-30000	30001	\$ Gold
1050	5	-8.912	10050	-10051	-20000	20001	-30000	30001	\$
			Nickel						
1051	6	-4.506	10051	-10052	-20000	20001	-30000	30001	\$
			Titanium						
1052	7	-2.700	10052	-10053	-20000	20001	-30000	30001	\$
			Aluminum						
1053	1	-2.330	10053	-10054	-20000	20001	-30000	30001	\$
			Silicon Dead Layer						
1054	1	-2.330	10054	-10055	-20000	20001	-30000	30001	\$
			Silicon						
1055	1	-2.330	10055	-10056	-20000	20001	-30000	30001	\$
			Silicon Dead Layer						
1056	7	-2.700	10056	-10057	-20000	20001	-30000	30001	\$
			Aluminum						
1057	6	-4.506	10057	-10058	-20000	20001	-30000	30001	\$
			Titanium						
1058	5	-8.912	10058	-10059	-20000	20001	-30000	30001	\$
			Nickel						
1059	4	-19.320	10059	-10060	-20000	20001	-30000	30001	\$ Gold

1060	2	-2.200	10060	-10061	-20000	20001	-30000	30001	\$	
		Silicon Oxide								
1061	4	-19.320	10061	-10062	-20000	20001	-30000	30001	\$	Gold
1062	5	-8.912	10062	-10063	-20000	20001	-30000	30001	\$	
		Nickel								
1063	6	-4.506	10063	-10064	-20000	20001	-30000	30001	\$	
		Titanium								
1064	7	-2.700	10064	-10065	-20000	20001	-30000	30001	\$	
		Aluminum								
1065	1	-2.330	10065	-10066	-20000	20001	-30000	30001	\$	
		Silicon Dead Layer								
1066	1	-2.330	10066	-10067	-20000	20001	-30000	30001	\$	
		Silicon								
1067	1	-2.330	10067	-10068	-20000	20001	-30000	30001	\$	
		Silicon Dead Layer								
1068	7	-2.700	10068	-10069	-20000	20001	-30000	30001	\$	
		Aluminum								
1069	6	-4.506	10069	-10070	-20000	20001	-30000	30001	\$	
		Titanium								
1070	5	-8.912	10070	-10071	-20000	20001	-30000	30001	\$	
		Nickel								
1071	4	-19.320	10071	-10072	-20000	20001	-30000	30001	\$	Gold
1072	2	-2.200	10072	-10073	-20000	20001	-30000	30001	\$	
		Silicon Oxide								
1073	4	-19.320	10073	-10074	-20000	20001	-30000	30001	\$	Gold
1074	5	-8.912	10074	-10075	-20000	20001	-30000	30001	\$	
		Nickel								
1075	6	-4.506	10075	-10076	-20000	20001	-30000	30001	\$	
		Titanium								
1076	7	-2.700	10076	-10077	-20000	20001	-30000	30001	\$	
		Aluminum								
1077	1	-2.330	10077	-10078	-20000	20001	-30000	30001	\$	
		Silicon Dead Layer								
1078	1	-2.330	10078	-10079	-20000	20001	-30000	30001	\$	
		Silicon								
1079	1	-2.330	10079	-10080	-20000	20001	-30000	30001	\$	
		Silicon Dead Layer								
1080	7	-2.700	10080	-10081	-20000	20001	-30000	30001	\$	
		Aluminum								
1081	6	-4.506	10081	-10082	-20000	20001	-30000	30001	\$	
		Titanium								
1082	5	-8.912	10082	-10083	-20000	20001	-30000	30001	\$	
		Nickel								
1083	4	-19.320	10083	-10084	-20000	20001	-30000	30001	\$	Gold
1084	2	-2.200	10084	-10085	-20000	20001	-30000	30001	\$	
		Silicon Oxide								
1085	4	-19.320	10085	-10086	-20000	20001	-30000	30001	\$	Gold
1086	5	-8.912	10086	-10087	-20000	20001	-30000	30001	\$	
		Nickel								
1087	6	-4.506	10087	-10088	-20000	20001	-30000	30001	\$	
		Titanium								
1088	7	-2.700	10088	-10089	-20000	20001	-30000	30001	\$	
		Aluminum								

1089	1	-2.330	10089	-10090	-20000	20001	-30000	30001	\$	
			Silicon Dead Layer							
1090	1	-2.330	10090	-10091	-20000	20001	-30000	30001	\$	
			Silicon							
1091	1	-2.330	10091	-10092	-20000	20001	-30000	30001	\$	
			Silicon Dead Layer							
1092	7	-2.700	10092	-10093	-20000	20001	-30000	30001	\$	
			Aluminum							
1093	6	-4.506	10093	-10094	-20000	20001	-30000	30001	\$	
			Titanium							
1094	5	-8.912	10094	-10095	-20000	20001	-30000	30001	\$	
			Nickel							
1095	4	-19.320	10095	-10096	-20000	20001	-30000	30001	\$	Gold
1096	2	-2.200	10096	-10097	-20000	20001	-30000	30001	\$	
			Silicon Oxide							
1097	4	-19.320	10097	-10098	-20000	20001	-30000	30001	\$	Gold
1098	5	-8.912	10098	-10099	-20000	20001	-30000	30001	\$	
			Nickel							
1099	6	-4.506	10099	-10100	-20000	20001	-30000	30001	\$	
			Titanium							
1100	7	-2.700	10100	-10101	-20000	20001	-30000	30001	\$	
			Aluminum							
1101	1	-2.330	10101	-10102	-20000	20001	-30000	30001	\$	
			Silicon Dead Layer							
1102	1	-2.330	10102	-10103	-20000	20001	-30000	30001	\$	
			Silicon							
1103	1	-2.330	10103	-10104	-20000	20001	-30000	30001	\$	
			Silicon Dead Layer							
1104	7	-2.700	10104	-10105	-20000	20001	-30000	30001	\$	
			Aluminum							
1105	6	-4.506	10105	-10106	-20000	20001	-30000	30001	\$	
			Titanium							
1106	5	-8.912	10106	-10107	-20000	20001	-30000	30001	\$	
			Nickel							
1107	4	-19.320	10107	-10108	-20000	20001	-30000	30001	\$	Gold
1108	2	-2.200	10108	-10109	-20000	20001	-30000	30001	\$	
			Silicon Oxide							
1109	4	-19.320	10109	-10110	-20000	20001	-30000	30001	\$	Gold
1110	5	-8.912	10110	-10111	-20000	20001	-30000	30001	\$	
			Nickel							
1111	6	-4.506	10111	-10112	-20000	20001	-30000	30001	\$	
			Titanium							
1112	7	-2.700	10112	-10113	-20000	20001	-30000	30001	\$	
			Aluminum							
1113	1	-2.330	10113	-10114	-20000	20001	-30000	30001	\$	
			Silicon Dead Layer							
1114	1	-2.330	10114	-10115	-20000	20001	-30000	30001	\$	
			Silicon							
1115	1	-2.330	10115	-10116	-20000	20001	-30000	30001	\$	
			Silicon Dead Layer							
1116	7	-2.700	10116	-10117	-20000	20001	-30000	30001	\$	
			Aluminum							
1117	6	-4.506	10117	-10118	-20000	20001	-30000	30001	\$	
			Titanium							

1118	5	-8.912	10118	-10119	-20000	20001	-30000	30001	\$
	Nickel								
1119	4	-19.320	10119	-10120	-20000	20001	-30000	30001	\$ Gold
1120	2	-2.200	10120	-10121	-20000	20001	-30000	30001	\$
	Silicon Oxide								
1121	4	-19.320	10121	-10122	-20000	20001	-30000	30001	\$ Gold
1122	5	-8.912	10122	-10123	-20000	20001	-30000	30001	\$
	Nickel								
1123	6	-4.506	10123	-10124	-20000	20001	-30000	30001	\$
	Titanium								
1124	7	-2.700	10124	-10125	-20000	20001	-30000	30001	\$
	Aluminum								
1125	1	-2.330	10125	-10126	-20000	20001	-30000	30001	\$
	Silicon Dead Layer								
1126	1	-2.330	10126	-10127	-20000	20001	-30000	30001	\$
	Silicon								
1127	1	-2.330	10127	-10128	-20000	20001	-30000	30001	\$
	Silicon Dead Layer								
1128	7	-2.700	10128	-10129	-20000	20001	-30000	30001	\$
	Aluminum								
1129	6	-4.506	10129	-10130	-20000	20001	-30000	30001	\$
	Titanium								
1130	5	-8.912	10130	-10131	-20000	20001	-30000	30001	\$
	Nickel								
1131	4	-19.320	10131	-10132	-20000	20001	-30000	30001	\$ Gold
1132	2	-2.200	10132	-10133	-20000	20001	-30000	30001	\$
	Silicon Oxide								
1133	4	-19.320	10133	-10134	-20000	20001	-30000	30001	\$ Gold
1134	5	-8.912	10134	-10135	-20000	20001	-30000	30001	\$
	Nickel								
1135	6	-4.506	10135	-10136	-20000	20001	-30000	30001	\$
	Titanium								
1136	7	-2.700	10136	-10137	-20000	20001	-30000	30001	\$
	Aluminum								
1137	1	-2.330	10137	-10138	-20000	20001	-30000	30001	\$
	Silicon Dead Layer								
1138	1	-2.330	10138	-10139	-20000	20001	-30000	30001	\$
	Silicon								
1139	1	-2.330	10139	-10140	-20000	20001	-30000	30001	\$
	Silicon Dead Layer								
1140	7	-2.700	10140	-10141	-20000	20001	-30000	30001	\$
	Aluminum								
1141	6	-4.506	10141	-10142	-20000	20001	-30000	30001	\$
	Titanium								
1142	5	-8.912	10142	-10143	-20000	20001	-30000	30001	\$
	Nickel								
1143	4	-19.320	10143	-10144	-20000	20001	-30000	30001	\$ Gold
1144	2	-2.200	10144	-10145	-20000	20001	-30000	30001	\$
	Silicon Oxide								
1145	4	-19.320	10145	-10146	-20000	20001	-30000	30001	\$ Gold
1146	5	-8.912	10146	-10147	-20000	20001	-30000	30001	\$
	Nickel								
1147	6	-4.506	10147	-10148	-20000	20001	-30000	30001	\$
	Titanium								

1148	7	-2.700	10148	-10149	-20000	20001	-30000	30001	\$
			Aluminum						
1149	1	-2.330	10149	-10150	-20000	20001	-30000	30001	\$
			Silicon Dead Layer						
1150	1	-2.330	10150	-10151	-20000	20001	-30000	30001	\$
			Silicon						
1151	1	-2.330	10151	-10152	-20000	20001	-30000	30001	\$
			Silicon Dead Layer						
1152	7	-2.700	10152	-10153	-20000	20001	-30000	30001	\$
			Aluminum						
1153	6	-4.506	10153	-10154	-20000	20001	-30000	30001	\$
			Titanium						
1154	5	-8.912	10154	-10155	-20000	20001	-30000	30001	\$
			Nickel						
1155	4	-19.320	10155	-10156	-20000	20001	-30000	30001	\$ Gold
1156	2	-2.200	10156	-10157	-20000	20001	-30000	30001	\$
			Silicon Oxide						
1157	4	-19.320	10157	-10158	-20000	20001	-30000	30001	\$ Gold
1158	5	-8.912	10158	-10159	-20000	20001	-30000	30001	\$
			Nickel						
1159	6	-4.506	10159	-10160	-20000	20001	-30000	30001	\$
			Titanium						
1160	7	-2.700	10160	-10161	-20000	20001	-30000	30001	\$
			Aluminum						
1161	1	-2.330	10161	-10162	-20000	20001	-30000	30001	\$
			Silicon Dead Layer						
1162	1	-2.330	10162	-10163	-20000	20001	-30000	30001	\$
			Silicon						
1163	1	-2.330	10163	-10164	-20000	20001	-30000	30001	\$
			Silicon Dead Layer						
1164	7	-2.700	10164	-10165	-20000	20001	-30000	30001	\$
			Aluminum						
1165	6	-4.506	10165	-10166	-20000	20001	-30000	30001	\$
			Titanium						
1166	5	-8.912	10166	-10167	-20000	20001	-30000	30001	\$
			Nickel						
1167	4	-19.320	10167	-10168	-20000	20001	-30000	30001	\$ Gold
1168	2	-2.200	10168	-10169	-20000	20001	-30000	30001	\$
			Silicon Oxide						
1169	4	-19.320	10169	-10170	-20000	20001	-30000	30001	\$ Gold
1170	5	-8.912	10170	-10171	-20000	20001	-30000	30001	\$
			Nickel						
1171	6	-4.506	10171	-10172	-20000	20001	-30000	30001	\$
			Titanium						
1172	7	-2.700	10172	-10173	-20000	20001	-30000	30001	\$
			Aluminum						
1173	1	-2.330	10173	-10174	-20000	20001	-30000	30001	\$
			Silicon Dead Layer						
1174	1	-2.330	10174	-10175	-20000	20001	-30000	30001	\$
			Silicon						
1175	1	-2.330	10175	-10176	-20000	20001	-30000	30001	\$
			Silicon Dead Layer						
1176	7	-2.700	10176	-10177	-20000	20001	-30000	30001	\$
			Aluminum						

1177	6	-4.506	10177	-10178	-20000	20001	-30000	30001	\$	
	Titanium									
1178	5	-8.912	10178	-10179	-20000	20001	-30000	30001	\$	
	Nickel									
1179	4	-19.320	10179	-10180	-20000	20001	-30000	30001	\$ Gold	
1180	2	-2.200	10180	-10181	-20000	20001	-30000	30001	\$	
	Silicon Oxide									
1181	4	-19.320	10181	-10182	-20000	20001	-30000	30001	\$ Gold	
1182	5	-8.912	10182	-10183	-20000	20001	-30000	30001	\$	
	Nickel									
1183	6	-4.506	10183	-10184	-20000	20001	-30000	30001	\$	
	Titanium									
1184	7	-2.700	10184	-10185	-20000	20001	-30000	30001	\$	
	Aluminum									
1185	1	-2.330	10185	-10186	-20000	20001	-30000	30001	\$	
	Silicon Dead Layer									
1186	1	-2.330	10186	-10187	-20000	20001	-30000	30001	\$	
	Silicon									
1187	1	-2.330	10187	-10188	-20000	20001	-30000	30001	\$	
	Silicon Dead Layer									
1188	7	-2.700	10188	-10189	-20000	20001	-30000	30001	\$	
	Aluminum									
1189	6	-4.506	10189	-10190	-20000	20001	-30000	30001	\$	
	Titanium									
1190	5	-8.912	10190	-10191	-20000	20001	-30000	30001	\$	
	Nickel									
1191	4	-19.320	10191	-10192	-20000	20001	-30000	30001	\$ Gold	
1192	2	-2.200	10192	-10193	-20000	20001	-30000	30001	\$	
	Silicon Oxide									
1193	4	-19.320	10193	-10194	-20000	20001	-30000	30001	\$ Gold	
1194	5	-8.912	10194	-10195	-20000	20001	-30000	30001	\$	
	Nickel									
1195	6	-4.506	10195	-10196	-20000	20001	-30000	30001	\$	
	Titanium									
1196	7	-2.700	10196	-10197	-20000	20001	-30000	30001	\$	
	Aluminum									
1197	1	-2.330	10197	-10198	-20000	20001	-30000	30001	\$	
	Silicon Dead Layer									
1198	1	-2.330	10198	-10199	-20000	20001	-30000	30001	\$	
	Silicon									
1199	1	-2.330	10199	-10200	-20000	20001	-30000	30001	\$	
	Silicon Dead Layer									
1200	7	-2.700	10200	-10201	-20000	20001	-30000	30001	\$	
	Aluminum									
1201	6	-4.506	10201	-10202	-20000	20001	-30000	30001	\$	
	Titanium									
1202	5	-8.912	10202	-10203	-20000	20001	-30000	30001	\$	
	Nickel									
1203	4	-19.320	10203	-10204	-20000	20001	-30000	30001	\$ Gold	
1204	2	-2.200	10204	-10205	-20000	20001	-30000	30001	\$	
	Silicon Oxide									
1205	4	-19.320	10205	-10206	-20000	20001	-30000	30001	\$ Gold	
1206	5	-8.912	10206	-10207	-20000	20001	-30000	30001	\$	
	Nickel									

1207	6	-4.506	10207	-10208	-20000	20001	-30000	30001	\$	
			Titanium							
1208	7	-2.700	10208	-10209	-20000	20001	-30000	30001	\$	
			Aluminum							
1209	1	-2.330	10209	-10210	-20000	20001	-30000	30001	\$	
			Silicon Dead Layer							
1210	1	-2.330	10210	-10211	-20000	20001	-30000	30001	\$	
			Silicon							
1211	1	-2.330	10211	-10212	-20000	20001	-30000	30001	\$	
			Silicon Dead Layer							
1212	7	-2.700	10212	-10213	-20000	20001	-30000	30001	\$	
			Aluminum							
1213	6	-4.506	10213	-10214	-20000	20001	-30000	30001	\$	
			Titanium							
1214	5	-8.912	10214	-10215	-20000	20001	-30000	30001	\$	
			Nickel							
1215	4	-19.320	10215	-10216	-20000	20001	-30000	30001	\$	Gold
1216	2	-2.200	10216	-10217	-20000	20001	-30000	30001	\$	
			Silicon Oxide							
1217	4	-19.320	10217	-10218	-20000	20001	-30000	30001	\$	Gold
1218	5	-8.912	10218	-10219	-20000	20001	-30000	30001	\$	
			Nickel							
1219	6	-4.506	10219	-10220	-20000	20001	-30000	30001	\$	
			Titanium							
1220	7	-2.700	10220	-10221	-20000	20001	-30000	30001	\$	
			Aluminum							
1221	1	-2.330	10221	-10222	-20000	20001	-30000	30001	\$	
			Silicon Dead Layer							
1222	1	-2.330	10222	-10223	-20000	20001	-30000	30001	\$	
			Silicon							
1223	1	-2.330	10223	-10224	-20000	20001	-30000	30001	\$	
			Silicon Dead Layer							
1224	7	-2.700	10224	-10225	-20000	20001	-30000	30001	\$	
			Aluminum							
1225	6	-4.506	10225	-10226	-20000	20001	-30000	30001	\$	
			Titanium							
1226	5	-8.912	10226	-10227	-20000	20001	-30000	30001	\$	
			Nickel							
1227	4	-19.320	10227	-10228	-20000	20001	-30000	30001	\$	Gold
1228	2	-2.200	10228	-10229	-20000	20001	-30000	30001	\$	
			Silicon Oxide							
1229	4	-19.320	10229	-10230	-20000	20001	-30000	30001	\$	Gold
1230	5	-8.912	10230	-10231	-20000	20001	-30000	30001	\$	
			Nickel							
1231	6	-4.506	10231	-10232	-20000	20001	-30000	30001	\$	
			Titanium							
1232	7	-2.700	10232	-10233	-20000	20001	-30000	30001	\$	
			Aluminum							
1233	1	-2.330	10233	-10234	-20000	20001	-30000	30001	\$	
			Silicon Dead Layer							
1234	1	-2.330	10234	-10235	-20000	20001	-30000	30001	\$	
			Silicon							
1235	1	-2.330	10235	-10236	-20000	20001	-30000	30001	\$	
			Silicon Dead Layer							

1236	7	-2.700	10236	-10237	-20000	20001	-30000	30001	\$	
Aluminum										
1237	6	-4.506	10237	-10238	-20000	20001	-30000	30001	\$	
Titanium										
1238	5	-8.912	10238	-10239	-20000	20001	-30000	30001	\$	
Nickel										
1239	4	-19.320	10239	-10240	-20000	20001	-30000	30001	\$ Gold	
1240	2	-2.200	10240	-10241	-20000	20001	-30000	30001	\$	
Silicon Oxide										
8888	0	-99999	#1000	#1001	#1002	#1003	#1004	#1005	#1006	#1007
			#1008	#1009	#1010	#1011	#1012	#1013	#1014	#1015
			#1016	#1017	#1018	#1019	#1020	#1021	#1022	#1023
			#1024	#1025	#1026	#1027	#1028	#1029	#1030	#1031
			#1032	#1033	#1034	#1035	#1036	#1037	#1038	#1039
			#1040	#1041	#1042	#1043	#1044	#1045	#1046	#1047
			#1048	#1049	#1050	#1051	#1052	#1053	#1054	#1055
			#1056	#1057	#1058	#1059	#1060	#1061	#1062	#1063
			#1064	#1065	#1066	#1067	#1068	#1069	#1070	#1071
			#1072	#1073	#1074	#1075	#1076	#1077	#1078	#1079
			#1080	#1081	#1082	#1083	#1084	#1085	#1086	#1087
			#1088	#1089	#1090	#1091	#1092	#1093	#1094	#1095
			#1096	#1097	#1098	#1099	#1100	#1101	#1102	#1103
			#1104	#1105	#1106	#1107	#1108	#1109	#1110	#1111
			#1112	#1113	#1114	#1115	#1116	#1117	#1118	#1119
			#1120	#1121	#1122	#1123	#1124	#1125	#1126	#1127
			#1128	#1129	#1130	#1131	#1132	#1133	#1134	#1135
			#1136	#1137	#1138	#1139	#1140	#1141	#1142	#1143
			#1144	#1145	#1146	#1147	#1148	#1149	#1150	#1151
			#1152	#1153	#1154	#1155	#1156	#1157	#1158	#1159
			#1160	#1161	#1162	#1163	#1164	#1165	#1166	#1167
			#1168	#1169	#1170	#1171	#1172	#1173	#1174	#1175
			#1176	#1177	#1178	#1179	#1180	#1181	#1182	#1183
			#1184	#1185	#1186	#1187	#1188	#1189	#1190	#1191
			#1192	#1193	#1194	#1195	#1196	#1197	#1198	#1199
			#1200	#1201	#1202	#1203	#1204	#1205	#1206	#1207
			#1208	#1209	#1210	#1211	#1212	#1213	#1214	#1215
			#1216	#1217	#1218	#1219	#1220	#1221	#1222	#1223
			#1224	#1225	#1226	#1227	#1228	#1229	#1230	#1231
			#1232	#1233	#1234	#1235	#1236	#1237	#1238	#1239
			#1240							\$
Vacuum										
9999	-1	99999								\$ Void

[S u r f a c e]

10000	pz	0.0000000000E+00	\$	Front	HDPE
10001	pz	1.0000000000E+00	\$	Front	Au
10002	pz	1.0000500000E+00	\$	Front	Ni
10003	pz	1.0000750000E+00	\$	Front	Ti
10004	pz	1.0000800000E+00	\$	Front	Al
10005	pz	1.0001050000E+00	\$	Front	Si (dead)
10006	pz	1.0002550000E+00	\$	Front	Si (active)
10007	pz	1.0039550000E+00	\$	Front	Si (dead)
10008	pz	1.0041050000E+00	\$	Front	Al
10009	pz	1.0041300000E+00	\$	Front	T

10010	pz	1.0041350000E+00	\$	Front	Ni
10011	pz	1.0041600000E+00	\$	Front	Au
10012	pz	1.0042100000E+00	\$	Front	SiO2
10013	pz	1.0042350000E+00	\$	Front	Au
10014	pz	1.0042850000E+00	\$	Front	Ni
10015	pz	1.0043100000E+00	\$	Front	Ti
10016	pz	1.0043150000E+00	\$	Front	Al
10017	pz	1.0043400000E+00	\$	Front	Si (dead)
10018	pz	1.0044900000E+00	\$	Front	Si (active)
10019	pz	1.0081900000E+00	\$	Front	Si (dead)
10020	pz	1.0083400000E+00	\$	Front	Al
10021	pz	1.0083650000E+00	\$	Front	Ti
10022	pz	1.0083700000E+00	\$	Front	Ni
10023	pz	1.0083950000E+00	\$	Front	Au
10024	pz	1.0084450000E+00	\$	Front	SiO2
10025	pz	1.0084700000E+00	\$	Front	Au
10026	pz	1.0085200000E+00	\$	Front	Ni
10027	pz	1.0085450000E+00	\$	Front	Ti
10028	pz	1.0085500000E+00	\$	Front	Al
10029	pz	1.0085750000E+00	\$	Front	Si (dead)
10030	pz	1.0087250000E+00	\$	Front	Si (active)
10031	pz	1.0124250000E+00	\$	Front	Si (dead)
10032	pz	1.0125750000E+00	\$	Front	Al
10033	pz	1.0126000000E+00	\$	Front	Ti
10034	pz	1.0126050000E+00	\$	Front	Ni
10035	pz	1.0126300000E+00	\$	Front	Au
10036	pz	1.0126800000E+00	\$	Front	SiO2
10037	pz	1.0127050000E+00	\$	Front	Au
10038	pz	1.0127550000E+00	\$	Front	Ni
10039	pz	1.0127800000E+00	\$	Front	Ti
10040	pz	1.0127850000E+00	\$	Front	Al
10041	pz	1.0128100000E+00	\$	Front	Si (dead)
10042	pz	1.0129600000E+00	\$	Front	Si (active)
10043	pz	1.0166600000E+00	\$	Front	Si (dead)
10044	pz	1.0168100000E+00	\$	Front	Al
10045	pz	1.0168350000E+00	\$	Front	Ti
10046	pz	1.0168400000E+00	\$	Front	Ni
10047	pz	1.0168650000E+00	\$	Front	Au
10048	pz	1.0169150000E+00	\$	Front	SiO2
10049	pz	1.0169400000E+00	\$	Front	Au
10050	pz	1.0169900000E+00	\$	Front	Ni
10051	pz	1.0170150000E+00	\$	Front	Ti
10052	pz	1.0170200000E+00	\$	Front	Al
10053	pz	1.0170450000E+00	\$	Front	Si (dead)
10054	pz	1.0171950000E+00	\$	Front	Si (active)
10055	pz	1.0208950000E+00	\$	Front	Si (dead)
10056	pz	1.0210450000E+00	\$	Front	Al
10057	pz	1.0210700000E+00	\$	Front	Ti
10058	pz	1.0210750000E+00	\$	Front	Ni
10059	pz	1.0211000000E+00	\$	Front	Au
10060	pz	1.0211500000E+00	\$	Front	SiO2
10061	pz	1.0211750000E+00	\$	Front	Au
10062	pz	1.0212250000E+00	\$	Front	Ni
10063	pz	1.0212500000E+00	\$	Front	Ti

10064	pz	1.0212550000E+00	\$	Front	Al
10065	pz	1.0212800000E+00	\$	Front	Si (dead)
10066	pz	1.0214300000E+00	\$	Front	Si (active)
10067	pz	1.0251300000E+00	\$	Front	Si (dead)
10068	pz	1.0252800000E+00	\$	Front	Al
10069	pz	1.0253050000E+00	\$	Front	Ti
10070	pz	1.0253100000E+00	\$	Front	Ni
10071	pz	1.0253350000E+00	\$	Front	Au
10072	pz	1.0253850000E+00	\$	Front	SiO2
10073	pz	1.0254100000E+00	\$	Front	Au
10074	pz	1.0254600000E+00	\$	Front	Ni
10075	pz	1.0254850000E+00	\$	Front	Ti
10076	pz	1.0254900000E+00	\$	Front	Al
10077	pz	1.0255150000E+00	\$	Front	Si (dead)
10078	pz	1.0256650000E+00	\$	Front	Si (active)
10079	pz	1.0293650000E+00	\$	Front	Si (dead)
10080	pz	1.0295150000E+00	\$	Front	Al
10081	pz	1.0295400000E+00	\$	Front	Ti
10082	pz	1.0295450000E+00	\$	Front	Ni
10083	pz	1.0295700000E+00	\$	Front	Au
10084	pz	1.0296200000E+00	\$	Front	SiO2
10085	pz	1.0296450000E+00	\$	Front	Au
10086	pz	1.0296950000E+00	\$	Front	Ni
10087	pz	1.0297200000E+00	\$	Front	Ti
10088	pz	1.0297250000E+00	\$	Front	Al
10089	pz	1.0297500000E+00	\$	Front	Si (dead)
10090	pz	1.0299000000E+00	\$	Front	Si (active)
10091	pz	1.0336000000E+00	\$	Front	Si (dead)
10092	pz	1.0337500000E+00	\$	Front	Al
10093	pz	1.0337750000E+00	\$	Front	Ti
10094	pz	1.0337800000E+00	\$	Front	Ni
10095	pz	1.0338050000E+00	\$	Front	Au
10096	pz	1.0338550000E+00	\$	Front	SiO2
10097	pz	1.0338800000E+00	\$	Front	Au
10098	pz	1.0339300000E+00	\$	Front	Ni
10099	pz	1.0339550000E+00	\$	Front	Ti
10100	pz	1.0339600000E+00	\$	Front	Al
10101	pz	1.0339850000E+00	\$	Front	Si (dead)
10102	pz	1.0341350000E+00	\$	Front	Si (active)
10103	pz	1.0378350000E+00	\$	Front	Si (dead)
10104	pz	1.0379850000E+00	\$	Front	Al
10105	pz	1.0380100000E+00	\$	Front	Ti
10106	pz	1.0380150000E+00	\$	Front	Ni
10107	pz	1.0380400000E+00	\$	Front	Au
10108	pz	1.0380900000E+00	\$	Front	SiO2
10109	pz	1.0381150000E+00	\$	Front	Au
10110	pz	1.0381650000E+00	\$	Front	Ni
10111	pz	1.0381900000E+00	\$	Front	Ti
10112	pz	1.0381950000E+00	\$	Front	Al
10113	pz	1.0382200000E+00	\$	Front	Si (dead)
10114	pz	1.0383700000E+00	\$	Front	Si (active)
10115	pz	1.0420700000E+00	\$	Front	Si (dead)
10116	pz	1.0422200000E+00	\$	Front	Al
10117	pz	1.0422450000E+00	\$	Front	Ti

10118	pz	1.0422500000E+00	\$	Front	Ni
10119	pz	1.0422750000E+00	\$	Front	Au
10120	pz	1.0423250000E+00	\$	Front	SiO2
10121	pz	1.0423500000E+00	\$	Front	Au
10122	pz	1.0424000000E+00	\$	Front	Ni
10123	pz	1.0424250000E+00	\$	Front	Ti
10124	pz	1.0424300000E+00	\$	Front	Al
10125	pz	1.0424550000E+00	\$	Front	Si (dead)
10126	pz	1.0426050000E+00	\$	Front	Si (active)
10127	pz	1.0463050000E+00	\$	Front	Si (dead)
10128	pz	1.0464550000E+00	\$	Front	Al
10129	pz	1.0464800000E+00	\$	Front	Ti
10130	pz	1.0464850000E+00	\$	Front	Ni
10131	pz	1.0465100000E+00	\$	Front	Au
10132	pz	1.0465600000E+00	\$	Front	SiO2
10133	pz	1.0465850000E+00	\$	Front	Au
10134	pz	1.0466350000E+00	\$	Front	Ni
10135	pz	1.0466600000E+00	\$	Front	Ti
10136	pz	1.0466650000E+00	\$	Front	Al
10137	pz	1.0466900000E+00	\$	Front	Si (dead)
10138	pz	1.0468400000E+00	\$	Front	Si (active)
10139	pz	1.0505400000E+00	\$	Front	Si (dead)
10140	pz	1.0506900000E+00	\$	Front	Al
10141	pz	1.0507150000E+00	\$	Front	Ti
10142	pz	1.0507200000E+00	\$	Front	Ni
10143	pz	1.0507450000E+00	\$	Front	Au
10144	pz	1.0507950000E+00	\$	Front	SiO2
10145	pz	1.0508200000E+00	\$	Front	Au
10146	pz	1.0508700000E+00	\$	Front	Ni
10147	pz	1.0508950000E+00	\$	Front	Ti
10148	pz	1.0509000000E+00	\$	Front	Al
10149	pz	1.0509250000E+00	\$	Front	Si (dead)
10150	pz	1.0510750000E+00	\$	Front	Si (active)
10151	pz	1.0547750000E+00	\$	Front	Si (dead)
10152	pz	1.0549250000E+00	\$	Front	Al
10153	pz	1.0549500000E+00	\$	Front	Ti
10154	pz	1.0549550000E+00	\$	Front	Ni
10155	pz	1.0549800000E+00	\$	Front	Au
10156	pz	1.0550300000E+00	\$	Front	SiO2
10157	pz	1.0550550000E+00	\$	Front	Au
10158	pz	1.0551050000E+00	\$	Front	Ni
10159	pz	1.0551300000E+00	\$	Front	Ti
10160	pz	1.0551350000E+00	\$	Front	Al
10161	pz	1.0551600000E+00	\$	Front	Si (dead)
10162	pz	1.0553100000E+00	\$	Front	Si (active)
10163	pz	1.0590100000E+00	\$	Front	Si (dead)
10164	pz	1.0591600000E+00	\$	Front	Al
10165	pz	1.0591850000E+00	\$	Front	Ti
10166	pz	1.0591900000E+00	\$	Front	Ni
10167	pz	1.0592150000E+00	\$	Front	Au
10168	pz	1.0592650000E+00	\$	Front	SiO2
10169	pz	1.0592900000E+00	\$	Front	Au
10170	pz	1.0593400000E+00	\$	Front	Ni
10171	pz	1.0593650000E+00	\$	Front	Ti

10172	pz	1.0593700000E+00	\$	Front	Al
10173	pz	1.0593950000E+00	\$	Front	Si (dead)
10174	pz	1.0595450000E+00	\$	Front	Si (active)
10175	pz	1.0632450000E+00	\$	Front	Si (dead)
10176	pz	1.0633950000E+00	\$	Front	Al
10177	pz	1.0634200000E+00	\$	Front	Ti
10178	pz	1.0634250000E+00	\$	Front	Ni
10179	pz	1.0634500000E+00	\$	Front	Au
10180	pz	1.0635000000E+00	\$	Front	SiO2
10181	pz	1.0635250000E+00	\$	Front	Au
10182	pz	1.0635750000E+00	\$	Front	Ni
10183	pz	1.0636000000E+00	\$	Front	Ti
10184	pz	1.0636050000E+00	\$	Front	Al
10185	pz	1.0636300000E+00	\$	Front	Si (dead)
10186	pz	1.0637800000E+00	\$	Front	Si (active)
10187	pz	1.0674800000E+00	\$	Front	Si (dead)
10188	pz	1.0676300000E+00	\$	Front	Al
10189	pz	1.0676550000E+00	\$	Front	Ti
10190	pz	1.0676600000E+00	\$	Front	Ni
10191	pz	1.0676850000E+00	\$	Front	Au
10192	pz	1.0677350000E+00	\$	Front	SiO2
10193	pz	1.0677600000E+00	\$	Front	Au
10194	pz	1.0678100000E+00	\$	Front	Ni
10195	pz	1.0678350000E+00	\$	Front	Ti
10196	pz	1.0678400000E+00	\$	Front	Al
10197	pz	1.0678650000E+00	\$	Front	Si (dead)
10198	pz	1.0680150000E+00	\$	Front	Si (active)
10199	pz	1.0717150000E+00	\$	Front	Si (dead)
10200	pz	1.0718650000E+00	\$	Front	Al
10201	pz	1.0718900000E+00	\$	Front	Ti
10202	pz	1.0718950000E+00	\$	Front	Ni
10203	pz	1.0719200000E+00	\$	Front	Au
10204	pz	1.0719700000E+00	\$	Front	SiO2
10205	pz	1.0719950000E+00	\$	Front	Au
10206	pz	1.0720450000E+00	\$	Front	Ni
10207	pz	1.0720700000E+00	\$	Front	Ti
10208	pz	1.0720750000E+00	\$	Front	Al
10209	pz	1.0721000000E+00	\$	Front	Si (dead)
10210	pz	1.0722500000E+00	\$	Front	Si (active)
10211	pz	1.0759500000E+00	\$	Front	Si (dead)
10212	pz	1.0761000000E+00	\$	Front	Al
10213	pz	1.0761250000E+00	\$	Front	Ti
10214	pz	1.0761300000E+00	\$	Front	Ni
10215	pz	1.0761550000E+00	\$	Front	Au
10216	pz	1.0762050000E+00	\$	Front	SiO2
10217	pz	1.0762300000E+00	\$	Front	Au
10218	pz	1.0762800000E+00	\$	Front	Ni
10219	pz	1.0763050000E+00	\$	Front	Ti
10220	pz	1.0763100000E+00	\$	Front	Al
10221	pz	1.0763350000E+00	\$	Front	Si (dead)
10222	pz	1.0764850000E+00	\$	Front	Si (active)
10223	pz	1.0801850000E+00	\$	Front	Si (dead)
10224	pz	1.0803350000E+00	\$	Front	Al
10225	pz	1.0803600000E+00	\$	Front	Ti

10226	pz	1.0803650000E+00	\$ Front Ni
10227	pz	1.0803900000E+00	\$ Front Au
10228	pz	1.0804400000E+00	\$ Front SiO2
10229	pz	1.0804650000E+00	\$ Front Au
10230	pz	1.0805150000E+00	\$ Front Ni
10231	pz	1.0805400000E+00	\$ Front Ti
10232	pz	1.0805450000E+00	\$ Front Al
10233	pz	1.0805700000E+00	\$ Front Si (dead)
10234	pz	1.0807200000E+00	\$ Front Si (active)
10235	pz	1.0844200000E+00	\$ Front Si (dead)
10236	pz	1.0845700000E+00	\$ Front Al
10237	pz	1.0845950000E+00	\$ Front Ti
10238	pz	1.0846000000E+00	\$ Front Ni
10239	pz	1.0846250000E+00	\$ Front Au
10240	pz	1.0846750000E+00	\$ Front SiO2
10241	pz	1.0847000000E+00	\$ Back SiO2
20000	px	5.0000000000E-01	
20001	px	-5.0000000000E-01	
30000	py	5.0000000000E-01	
30001	py	-5.0000000000E-01	
99999	so	2.0000000000E+02	

[V o l u m e]

reg	vol
1005	1.5000E-04
1006	3.7000E-03
1007	1.5000E-04
1017	1.5000E-04
1018	3.7000E-03
1019	1.5000E-04
1029	1.5000E-04
1030	3.7000E-03
1031	1.5000E-04
1041	1.5000E-04
1042	3.7000E-03
1043	1.5000E-04
1053	1.5000E-04
1054	3.7000E-03
1055	1.5000E-04
1065	1.5000E-04
1066	3.7000E-03
1067	1.5000E-04
1077	1.5000E-04
1078	3.7000E-03
1079	1.5000E-04
1089	1.5000E-04
1090	3.7000E-03
1091	1.5000E-04
1101	1.5000E-04
1102	3.7000E-03
1103	1.5000E-04
1113	1.5000E-04
1114	3.7000E-03
1115	1.5000E-04

```

1125  1.5000E-04
1126  3.7000E-03
1127  1.5000E-04
1137  1.5000E-04
1138  3.7000E-03
1139  1.5000E-04
1149  1.5000E-04
1150  3.7000E-03
1151  1.5000E-04
1161  1.5000E-04
1162  3.7000E-03
1163  1.5000E-04
1173  1.5000E-04
1174  3.7000E-03
1175  1.5000E-04
1185  1.5000E-04
1186  3.7000E-03
1187  1.5000E-04
1197  1.5000E-04
1198  3.7000E-03
1199  1.5000E-04
1209  1.5000E-04
1210  3.7000E-03
1211  1.5000E-04
1221  1.5000E-04
1222  3.7000E-03
1223  1.5000E-04
1233  1.5000E-04
1234  3.7000E-03
1235  1.5000E-04

```

[T - D e p o s i t]

```

title = Number Deposition in Active Si
mesh  = reg
reg   = 1006 1018 1030 1042 1054 1066 1078 1090 1102 1114 1126 1138
      1150 1162 1174 1186
      1198 1210 1222 1234
unit  = 3
part  = all
output = deposit
deposit = 0
axis  = eng
resfile = NumberDepositionSiActive.dat
file   = NumberDepositionSiActive.dat
e-type = 2
ne     = 2000
emin   = 0.0
emax   = 20.0

```

[T - D e p o s i t]

```

title = Number Deposition in Dead Si (Front)
mesh  = reg
reg   = 1005 1017 1029 1041 1053 1065 1077 1089 1101 1113 1125 1137
      1149 1161 1173 1185

```

```
      1197 1209 1221 1233
unit   =   3
part   =   all
output =   deposit
deposit =   0
axis   =   eng
resfile = NumberDepositionSiDeadFront.dat
file    =   NumberDepositionSiDeadFront.dat
e-type =   2
ne     =  2000
emin   =   0.0
emax   =  20.0
```

[T - D e p o s i t]

```
title  =   Number Deposition in Dead Si (Back)
mesh   =   reg
reg     =   1007 1019 1031 1043 1055 1067 1079 1091 1103 1115 1127 1139
        1151 1163 1175 1187
        1199 1211 1223 1235
unit   =   3
part   =   all
output =   deposit
deposit =   0
axis   =   eng
resfile = NumberDepositionSiDeadBack.dat
file    =   NumberDepositionSiDeadBack.dat
e-type =   2
ne     =  2000
emin   =   0.0
emax   =  20.0
```

[E n d]

Appendix B

pysrim Script for PMFND Proton Stopping Power Simulations

```
### CONSTRUCTING A SRIM SIMULATION WITH PYSRIM

import srим
import shutil
import os
import numpy as np

### CONSTANTS
cmToAngstrom = 1e+8
umToAngstrom = 1e+4

def MigrateData(source, destination):
    fileList =
        ['E2RECOIL.txt', 'IONIZ.txt', 'LATERAL.txt', 'NOVAC.txt', 'PHONON.txt', 'RANGE.txt',
        'TRIMAUTO']
    for filename in fileList:
        shutil.move(source + filename, destination + filename)

def MakeDirectory(location, newDirectory):
    if os.path.exists(location):
        if not os.path.exists(location + newDirectory):
            os.mkdir(location + newDirectory)
    else:
        raise Exception('Anchor location at ' + location + ' does not
            exist.')

def MFNDLayers(hdpeThickness, nLayers=1):
    hdpe = srим.Layer({
        'C' : {
            'stoich' : 2.0,
```

```

        'E_d' : 28.0,
        'lattice' : 3.0,
        'surface' : 7.41
    },
    'H' : {
        'stoich' : 4.0,
        'E_d' : 10.0,
        'lattice' : 3.0,
        'surface' : 2.0
    }
},
density=0.97,
width=hdpeThickness*cmToAngstrom,
phase=0,
name='HDPE'
)

gold = srim.Layer({
    'Au' : {
        'stoich' : 1.0,
        'E_d' : 25.0,
        'lattice' : 3.0,
        'surface' : 3.8
    }
},
density=19.311,
width=0.5*umToAngstrom,
phase=0,
name='Gold'
)

nickel = srim.Layer({
    'Ni' : {
        'stoich' : 1.0,
        'E_d' : 25.0,
        'lattice' : 3.0,
        'surface' : 4.46
    }
},
density=8.8955,
width=0.25*umToAngstrom,
phase=0,
name='Nickel'
)

titanium = srim.Layer({
    'Ti' : {
        'stoich' : 1.0,
        'E_d' : 25.0,
        'lattice' : 3.0,
        'surface' : 4.89
    }
},
density=4.5189,

```

```

        width=0.05*umToAngstrom,
        phase=0,
        name='Titanium'
    )

aluminum = srim.Layer({
    'Al' : {
        'stoich' : 1.0,
        'E_d' : 25.0,
        'lattice' : 3.0,
        'surface' : 3.36
    }
},
density=2.702,
width=0.25*umToAngstrom,
phase=0,
name='Aluminum'
)

diode = srim.Layer({
    'Si' : {
        'stoich' : 1.0,
        'E_d' : 15.0,
        'lattice' : 2.0,
        'surface' : 4.7
    }
},
density=2.3212,
width=40.0*umToAngstrom,
phase=0,
name='Diode'
)

siliconDioxide = srim.Layer({
    'Si' : {
        'stoich' : 1.0,
        'E_d' : 15.0,
        'lattice' : 2.0,
        'surface' : 4.7
    },
    'O' : {
        'stoich' : 2.0,
        'E_d' : 28.0,
        'lattice' : 3.0,
        'surface' : 2.0
    }
},
density=2.2,
width=0.25*umToAngstrom,
phase=0,
name='Silicon Dioxide'
)

unitCell = [gold, nickel, titanium, aluminum, diode, aluminum,
titanium, nickel, gold, siliconDioxide]

```

```

layerList = []
if hdpeThickness == 0.0:
    None
else:
    layerList.append(hdpe)

for i in range(0, nLayers):
    layerList += unitCell

return layerList

def mainMFND(projectileIon, energy, hdpeThickness, nIons, nLayers=50,
plotFocus='all'):

    energy *= 1e+6 # CONVERTS eV TO MeV

    ### SPECIFY SRIM DIRECTORY
    srimExecutableDirectory = 'C://SRIM-2013/'

    ### SPECIFY PLACE YOU WANT TO SAVE THINGS
    storageLocation = 'E://Work/DetectorGithub/PYTHON/Analysis/SRIM/'

    ### FILE STRINGS
    energyString = str(int(energy // 1e+6)) + '-MeV'
    hdpeThicknessString = str(int(hdpeThickness * 10000)) + '-um'

    thisDirectory = 'run-' + energyString + '-' + hdpeThicknessString +
        '-' + plotFocus + '/'

    ### PICK YOUR ION
    ion = srim.Ion(projectileIon, energy=energy)

    ### CONSTRUCT YOUR LAYERS
    layerList = MFNDLayers(hdpeThickness, nLayers)

    ### SET PLOTTING BOUNDARIES
    unitCellWidth = 42.35*umToAngstrom
    if plotFocus == 'all':
        xMin = 0
        xMax = hdpeThickness + unitCellWidth*nLayers
    elif 'layer-' in plotFocus[:-1]:
        layerIndex = abs(int(plotFocus[-2:])) ### LAYER INDEX STARTS AT 0
        xMin = hdpeThickness + unitCellWidth*layerIndex
        xMax = xMin + unitCellWidth

    ### CONSTRUCT YOUR TARGET
    target = srim.Target(layerList)

    ### START TRIM CALCULATION
    trim = srim.TRIM(target, ion, number_ions=nIons, calculation=1,
        plot_xmin=xMin, plot_xmax=xMax)
    trim.run(srimExecutableDirectory)

    ### MIGRATE RESULTS TO DESIRED DIRECTORY

```

```
MakeDirectory(storageLocation, thisDirectory)
MigrateData(srimExecutableDirectory, storageLocation + thisDirectory)

if __name__ == '__main__':

    energy = np.arange(1, 20 + 1)
    hdpeThickness = 0.0
    ion = 'H'
    nParticles = 100
    nLayers = np.arange(0, 55)

    for i in range(0, len(energy)):
        for j in range(0, len(nLayers)):
            mainMFND(ion, energy[i], hdpeThickness, nParticles,
                    nLayers[-1] + 1, plotFocus='layer-' + str(nLayers[j]))
```

Appendix C

Custom Monte Carlo Code for Determining Entry Probability

```
### SCATTERING ANALYSIS
import numpy as np
import matplotlib.pyplot as plt
import scipy as sc
import scipy.interpolate
from mpl_toolkits.mplot3d import Axes3D
import matplotlib
import pickle
font = {'family' : 'Times New Roman',
        'weight' : 'normal',
        'size'   : 16}
matplotlib.rc('font', **font)
plt.rcParams.update({'mathtext.fontset' : 'cm'})
precision = np.float64

def GetIonA(ion):
    A = int(ion.split('-')[1])
    return A

def GetEjectileNeutronEnergy(En, ws, A, Q):
    sqrtEnplus = 1 / (A + 1) * (ws * np.sqrt(En) + np.sqrt(En * (ws ** 2
        + A ** 2 - 1) + A * (A + 1) * Q))
    sqrtEnminus = 1 / (A + 1) * (ws * np.sqrt(En) - np.sqrt(En * (ws **
        2 + A ** 2 - 1) + A * (A + 1) * Q))
    valid = (sqrtEnminus >= 0) * (Q < 0)
    Enplus = sqrtEnplus ** 2
    Enminus = sqrtEnminus ** 2 * valid
    return Enplus, Enminus

# def GetEjectileIonEnergy(En, Enp, ws, ):
```

```

def ConvertUnitsEnergy(unit):
    ### CONVERT FROM unit TO MeV
    if unit == 'eV':
        multiplier = 1e-6
    elif unit == 'keV':
        multiplier = 1e-3
    elif unit == 'MeV':
        multiplier = 1.0
    return multiplier

def ConvertUnitsDistance(unit):
    ### CONVERT FROM unit TO cm
    if unit == 'A':
        multiplier = 1e-8
    elif unit == 'um':
        multiplier = 1e-4
    elif unit == 'mm':
        multiplier = 1e-1
    elif unit == 'cm':
        multiplier = 1.0
    return multiplier

def GetRange(filename):
    a = open(filename, 'r')
    read = a.readlines()
    a.close()

    startLine = '-----'
    stopLine =
    '-----'

    for i in range(0, len(read)):
        line = read[i].split()
        if len(line) > 0:
            if line[0] == startLine:
                startIndex = i + 1
            if line[0] == stopLine:
                endIndex = i - 1
    read = read[startIndex : endIndex + 1]

    ### LOOP THROUGH TABLE
    # ENERGIES IN MeV
    # DISTANCES IN cm
    energy = np.array([])
    projectedRange = np.array([])
    for i in range(0, len(read)):
        line = read[i].split()
        energyUnit = line[1]
        thisEnergy = float(line[0]) * ConvertUnitsEnergy(energyUnit)
        energy = np.append(energy, thisEnergy)
        distanceUnit = line[5]
        thisProjectedRange = float(line[4]) *
            ConvertUnitsDistance(distanceUnit)
        projectedRange = np.append(projectedRange, thisProjectedRange)

```

```

    return energy, projectedRange

def GetRangePSTAR(filename, density):
    data = np.genfromtxt(filename, skip_header=7, delimiter=' ')
    energy = data[:, 0]
    csdaRange = data[:, 1] / density
    projectedRange = data[:, 2] / density
    return energy, csdaRange, projectedRange

fH2 = 0.00015
fH1 = 1 - fH2
fC12 = 1

def ReadJANIS(filename, labels):
    a = open(filename, 'r')
    read = a.readlines()
    a.close()

    thisTarget = {}

    energy = np.array([])

    for i in range(3, len(read)):
        line = read[i].split(' ; ')
        energy = np.append(energy, float(line[0]))
        if i == 3:
            for j in range(1, len(line)):
                thisTarget[labels[j - 1]] = np.array([])

            for j in range(1, len(line)):
                if line[j] == '' or line[j] == '\n':
                    line[j] = '0.0'
                thisTarget[labels[j - 1]] = np.append(thisTarget[labels[j - 1]], float(line[j]))

    return energy, thisTarget

def PlotTarget(energy, thisTarget, labels):
    for j in range(0, len(labels)):
        plt.plot(energy, thisTarget[labels[j]], label=labels[j])
    plt.legend()
    plt.xscale('log')
    plt.yscale('log')
    plt.xlabel('Neutron Kinetic Energy [MeV]')
    plt.ylabel('Cross Section [barns]')

def MakeInterpolationFunction(x, y):
    logx = np.log10(x)
    logy = np.log10(y)
    linInterp = sc.interpolate.interp1d(logx, logy, bounds_error=False,
        fill_value=(-np.inf, np.max(logy)), kind='linear')
    logInterp = lambda z: np.power(10.0, linInterp(np.log10(z)))
    return logInterp

```

```

filename = '1-1-H.csv'
labelsH1 = ['(n,total)', '(n,elastic)', '(n,g)']
energyH1, H1 = ReadJANIS(filename, labelsH1)

filename = '2-1-H.csv'
labelsH2 = ['(n,2n)', '(n,elastic)', '(n,total)', '(n,g)']
energyH2, H2 = ReadJANIS(filename, labelsH2)

filename = '12-6-C.csv'
labelsC12 =
    ['(n,total)', '(n,elastic)', '(n,inelastic)', '(n,other)', '(n,n+p)', '(n,g)', '(n,p)', '(n,p)']
energyC12, C12 = ReadJANIS(filename, labelsC12)

### INTERPOLATE CROSS SECTION DATA

def GetCrossSection(interaction, energy):
    if interaction in labelsH1:
        H1i = MakeInterpolationFunction(energyH1, H1[interaction])
    else:
        H1i = lambda x : 0
    if interaction in labelsH2:
        H2i = MakeInterpolationFunction(energyH2, H2[interaction])
    else:
        H2i = lambda x : 0
    if interaction in labelsC12:
        C12i = MakeInterpolationFunction(energyC12, C12[interaction])
    else:
        C12i = lambda x : 0

    xc = 1 * (fC12 * C12i(energy) + 2 * (fH1 * H1i(energy) + fH2 *
        H2i(energy)))
    return xc

def GetCrossSectionSingle(interaction, energy, target):
    if target == 'H1':
        return 2 * fH1 * MakeInterpolationFunction(energyH1,
            H1[interaction])(energy)
    elif target == 'H2':
        return 2 * fH2 * MakeInterpolationFunction(energyH2,
            H2[interaction])(energy)
    elif target == 'C12':
        return 1 * fC12 * MakeInterpolationFunction(energyC12,
            C12[interaction])(energy)

if __name__ == '__main__':

    ### KNOWN
    En = 20

    ### SELECTABLE
    Q = 0
    # assert(Q <= 0), 'Q-value must be endothermic'
    ion = 'H-1'

```

```

# ion = 'H-2'
# ion = 'C-12'

energyList = energyH1

### GET HDPE NUMBER DENSITY
barnConversion = 1e-24
avogadrosNumber = 6.0221408e+23 # mol-1
rho = 0.97 # g cm-3
h1AtomicMass = 1.0078250321
h2AtomicMass = 2.0141017780
c12AtomicMass = 12.00000000
c13AtomicMass = 13.0033548378
atomicMass = 2 * fH1 * h1AtomicMass + 2 * fH2 * h2AtomicMass + fC12 *
    c12AtomicMass

### PROBABILITY THAT NEUTRON MAKES IT TO x PRIOR TO INTERACTION
muHDPEtotal = GetCrossSection('(n,total)', energyList) * hdpeN
muHDPEscatterH1 = GetCrossSectionSingle('(n,elastic)', energyList,
    'H1') * hdpeN # + GetCrossSectionSingle('(n,inelastic)',
    energyList, 'H1')
muHDPEscatterH2 = GetCrossSectionSingle('(n,elastic)', energyList,
    'H2') * hdpeN # + GetCrossSectionSingle('(n,inelastic)',
    energyList, 'H2')
muHDPEscatterC12 = (GetCrossSectionSingle('(n,elastic)', energyList,
    'C12') + GetCrossSectionSingle('(n,inelastic)', energyList,
    'C12')) * hdpeN
muHDPEscatter = muHDPEscatterH1 + muHDPEscatterH2 + muHDPEscatterC12
# energyList = energyList / 1e+6

muHDPEtotal = MakeInterpolationFunction(energyList / 1e+6,
    muHDPEtotal)
muHDPEscatter = MakeInterpolationFunction(energyList / 1e+6,
    muHDPEscatter)
muHDPEscatterH1 = MakeInterpolationFunction(energyList / 1e+6,
    muHDPEscatterH1)
muHDPEscatterH2 = MakeInterpolationFunction(energyList / 1e+6,
    muHDPEscatterH2)
muHDPEscatterC12 = MakeInterpolationFunction(energyList / 1e+6,
    muHDPEscatterC12)
# ionList = ['H-1', 'H-2', 'C-12']
ionList = ['C-12', 'H-2', 'H-1']

### DERIVED
dx = 1
dy = 1
dz = 1

### PROCEDURE -- WANT TO DETERMINE DISTRIBUTION OF T AND cos(thetar)

### RANDOMLY SELECT wc
N = 20000

```

```

iChoice = 10
points = 10
dividingFactor = 5
xMesh = np.linspace(-dx / 2, dx / 2, points // dividingFactor,
    dtype=precision)
yMesh = np.linspace(-dy / 2, dy / 2, points // dividingFactor,
    dtype=precision)
zMesh = np.linspace(0.0 * dz, dz, points + 1, dtype=precision)
zMesh = zMesh[:-1]
xdiff = np.diff(xMesh)[0]
ydiff = np.diff(yMesh)[0]
zdiff = np.diff(zMesh)[0]

### ARRAY METHOD
X0, Y0, Z0 = np.meshgrid(xMesh, yMesh, zMesh)
# hitProbabilityArray = np.zeros(np.shape(X0))
startPoint = np.array([X0, Y0, (2 * Z0 + zdiff) / 2], dtype=precision)

P1 = np.exp(-muHDPEtotal(En) * Z0) - np.exp(-muHDPEtotal(En) * (Z0 +
    zdiff))

P = 0
for ion in ionList:
    if ion == 'H-1':
        rangeFilename = 'h-1-in-hdpe-range.txt'
        muIon = muHDPEscatterH1(En)
    elif ion == 'H-2':
        rangeFilename = 'h-2-in-hdpe-range.txt'
        muIon = muHDPEscatterH2(En)
    elif ion == 'C-12':
        rangeFilename = 'c-12-in-hdpe-range.txt'
        muIon = muHDPEscatterC12(En)
    elif ion == 'C-13':
        rangeFilename = 'c-13-in-hdpe-range.txt'
        muIon = muHDPEscatterC13(En)

P2 = muIon / muHDPEtotal(En)

A = GetIonA(ion)
gamma = (A ** 2 + A * (A + 1) * Q / En) ** (-1/2)
alpha = (A - 1) ** 2 / ((A + 1) ** 2)
Delta = Q * (1 + A) / A / En

wc = (2 * np.random.rand(N) - 1).astype(precision)
T = 0.5 * En * (1 - alpha) * (1 - wc * np.sqrt(1 + Delta)) + Q *
    A / (A + 1)

Enp = En - T + Q
wr = np.sqrt(1 - 1 / A * Enp / T * (1 - wc ** 2) / ((gamma + wc)
    ** 2 + (1 - wc ** 2)))
wr[T == 0] = 0
wr[T == En] = 1

### WE HAVE T AND wr

```

```

thetar = np.arccos(wr)

### CHOOSE AN AZIMUTHAL ANGLE RANDOMLY
psir = (np.random.rand(N) * 2 * np.pi).astype(precision)

### DETERMINE TRAJECTORY
xdir = np.cos(psir) * np.sin(thetar)
ydir = np.sin(psir) * np.sin(thetar)
zdir = np.cos(thetar)

### DETERMINE RANGE
energyRange, ionRange = GetRange(rangeFilename)
ionRange = MakeInterpolationFunction(energyRange, ionRange)
R = ionRange(T).astype(precision)

### DETERMINE POINT AT WHICH PARTICLE RANGES OUT (IN HDPE)
# endPoint = np.array([R * xdir + startPoint[0], R * ydir +
#     startPoint[1], R * zdir + startPoint[2]])
xEndPoint = np.tensordot(R * xdir,
    np.ones(np.shape(startPoint[0]), dtype=precision), axes=0) +
    startPoint[0]
yEndPoint = np.tensordot(R * ydir,
    np.ones(np.shape(startPoint[1]), dtype=precision), axes=0) +
    startPoint[1]
zEndPoint = np.tensordot(R * zdir,
    np.ones(np.shape(startPoint[2]), dtype=precision), axes=0) +
    startPoint[2]
endPoint = np.array([xEndPoint, yEndPoint, zEndPoint])

txPlus = (dx / 2 - startPoint[0]) / (endPoint[0] - startPoint[0])
txMinus = (- dx / 2 - startPoint[0]) / (endPoint[0] -
    startPoint[0])
tyPlus = (dy / 2 - startPoint[1]) / (endPoint[1] - startPoint[1])
tyMinus = (- dy / 2 - startPoint[1]) / (endPoint[1] -
    startPoint[1])
txMask = txPlus > txMinus
tx = txMask * txPlus + ~txMask * txMinus
tyMask = tyPlus > tyMinus
ty = tyMask * tyPlus + ~tyMask * tyMinus
tz = (dz - startPoint[2]) / (zEndPoint - startPoint[2])

### FIND INTERSECTION POINTS
intersectionx1 = startPoint[0] + (endPoint[0] - startPoint[0]) *
    tz
intersectiony1 = startPoint[1] + (endPoint[1] - startPoint[1]) *
    tz
intersectionz1 = startPoint[2] + (endPoint[2] - startPoint[2]) *
    tz
condition = (tx >= tz) * (ty >= tz) * (tz <= 1) * (tz >= 0)
# intersectionx = np.where(condition, intersectionx1, np.nan)
# intersectiony = np.where(condition, intersectiony1, np.nan)
# intersectionz = np.where(condition, intersectionz1, np.nan)
intersectionx = np.where(condition, intersectionx1, np.nan)
intersectiony = np.where(condition, intersectiony1, np.nan)

```

```
intersectionz = np.where(condition, intersectionz1, np.nan)
xEnd = endPoint[0]
yEnd = endPoint[1]
zEnd = endPoint[2]

hits = np.sum(condition, axis=0)
P3 = hits / N
P += P1 * P2 * P3
```
